



Sept 94

UPPER CRUSTAL VELOCITY STRUCTURE OF THE
SOUTHWESTERN CANADIAN CORDILLERA FROM EXPLOSION
RECORDINGS ON THE WCTN EARTHQUAKE SEISMIC NET

by

Stephen John Fallows
B.Sc., University of York, England, 1991

A Thesis Submitted in Partial Fulfilment of the
requirements for the Degree of

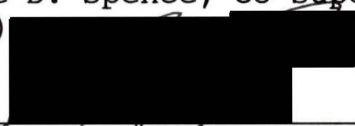
MASTER OF SCIENCE

in the School of Earth and Ocean Sciences

We accept this thesis as conforming
to the required standard



Dr George D. Spence, Co-Supervisor (School of Earth and Ocean
Sciences)



Dr Gary C. Rogers, Co-Supervisor (Pacific Geoscience Centre)



Dr Roy D. Hyndman, Department Member (Pacific Geoscience
Centre)



Dr C. Peter Keller, Outside Member (Department of Geography)



Dr Harry W. Dosso, External Examiner (Department of Physics)

© **STEPHEN FALLOWS, 1994. UNIVERSITY OF VICTORIA.**

All rights reserved. Thesis may not be reproduced in whole or
part, by photocopy or other means, with the permission of the
author.

Co-Supervisors: George D. Spence and Gary C. Rogers

ABSTRACT

The Western Canadian Telemetered Network (WCTN) in southwestern B.C recorded explosion shots from Lithoprobe's Southern Cordillera Refraction Experiment (SCoRE) in 1989 and 1990 and from the USGS Pacific Northwest refraction survey in 1991. Of the 24 shots which produced detectable arrivals at the 18 WCTN stations 14 shots and 14 stations were selected as the utilizable data set. The geographical distribution of the shots and receiver stations enables a large three dimensional area to be sampled. Most receivers show good P wave arrivals and S waves are recorded at many sites. Only ray paths considered to be in the top 10 km of the crust were used, and so all velocity estimates made were for the upper crust.

The data sets were modelled using two methods: an in-line refraction least squares method and a tomographic inversion procedure. Seismograms from combinations of shots and receivers were separated from the main data set to leave only those which sample along a two dimensional profile. Along five profiles estimates of P wave velocity, S wave velocity and Poisson's ratio were made. P wave velocities were found to be highest over southern Vancouver Island (6.55 km/s), while S waves were highest over the southernmost Coast Belt and Georgia Strait (3.75 km/s). Poisson's ratio along the five profiles is homogenous except for an increase in the profile

on the south of Vancouver Island.

The travel time data were also modelled using a tomographic inversion procedure. The real earth was represented as a near surface velocity layer of uniform thickness over a refracting velocity grid. The results obtained were in overall agreement with the two dimensional profiles, and previous refraction surveys conducted in the region.

High values of Poisson's ratio over Vancouver Island (0.27-0.28) may be related to (a) high mafic content represented by the volcanics of Wrangellia, or (b) fluids moving up through the continental crust released by the subducting Juan de Fuca Plate. Both the Georgia Strait and mainland have lower Poisson's ratios than Vancouver Island. The northern region of the Coast Belt has especially low values (0.20-0.24) which may be related to high quartz content in the crust.

Examiners:



Dr George D. Spence, Co-Supervisor (School of Earth and Ocean Sciences)



Dr Gary C. Rogers, Co-Supervisor (Pacific Geoscience Centre)



Dr Roy D. Hyndman, Department Member (Pacific Geoscience Centre)



Dr C. Peter Keller, Outside Member (Department of Geography)



Dr Harry W. Dosso, External Examiner (Department of Physics)

TABLE OF CONTENTS

Abstract.....	ii
Table of Contents.....	v
List of Tables.....	vii
List of Figures.....	viii
Acknowledgements.....	xii
Chapter One	TECTONIC AND GEOPHYSICAL FRAMEWORK
1.1 Introduction.....	1
1.2 Tectonic setting.....	2
1.3 Geological setting.....	3
1.4 Geophysical setting	
1.4.1 Regional seismic surveys.....	6
1.4.2 Southern Cordillera refraction experiment.....	7
Chapter Two	DATA ACQUISITION AND PROCESSING
2.1 Introduction.....	11
2.2 Filtering.....	13
2.3 Initial data characteristics.....	16
Chapter Three	DATA ANALYSIS AND INTERPRETATION PROCEDURES
3.1 Introduction.....	19
3.2 Travel time picking.....	23
3.3 Constructing the inversion data sets.....	23

3.4	Inversion method.....	30
3.5	Inversion method testing.....	36
Chapter Four RESULTS		
4.1	Initial in-line refraction interpretation.....	49
4.2	P wave inversion	62
4.3	Additional inversions on the P wave data set	
4.3.1	Rotation of the grid.....	65
4.3.2	Deletion of high offsets.....	67
4.4	S wave inversion	69
4.5	Poisson's ratio results.....	72
4.6	Near surface layer results.....	73
4.7	Uncertainties in velocities and Poisson's ratio.....	79
Chapter Five DISCUSSION		
5.1	Comparison of results with previous refraction work..	82
5.2	Implications of results.....	86
Bibliography.....		92
Appendix 1	P and S wave seismograms.....	97
Appendix 2	P Wave inversion data set.....	115
Appendix 3	S Wave inversion data set.....	118
Appendix 4	Time term method.....	120

LIST OF TABLES

Table 1. Location of the WCTN stations.....	11
Table 2. Location and charge size of explosion shots.....	13
Table 3. P wave travel time picks for shot/station..... combinations.	30
Table 4. S wave travel time picks for shot/station..... combinations.	31
Table 5. Distance travelled within each grid element..... by ray paths on a 10x10 grid.	39
Table 6. Distance travelled within each grid element..... by ray paths on a 20x20 grid.	43
Table 7. Comparison of test velocities and their..... modelled values in the near surface layer.	47
Table 8. P wave velocity, S wave velocity and Poisson's..... ratio estimates for the upper crust from in-line data sets.	61
Table 9. Distance travelled by the P wave ray paths..... within each grid element of a 8x7 along strike grid.	64
Table 10. Distance travelled by the S wave ray paths..... within each grid element of a 8x7 along strike grid.	72
Table 11. Velocities estimates in the near surface..... layer from several inversions.	76
Table 12. Error estimates as given by path density.....	81

LIST OF FIGURES

Figure 1. Location map of previous refraction lines.....4 showing major geological features.	4
Figure 2. Location map of shotpoints and receivers.....12	12
Figure 3. Amplitude spectra for P wave arrivals.....14 from shot 8.	14
Figure 4. Amplitude spectra for S wave arrivals.....15 from shot 8.	15
Figure 5. (a) S wave arrivals at Campbell River with.....17 a 3-30 Hz filter. (b) S wave arrivals at Campbell River with a 3-7 Hz filter.	17
Figure 6. (a) Travel paths through the SCoRE Line 2 model...26 (b) Theoretical travel times from shot point 12.	26
Figure 7. Travel paths of the 116 P waves.....28	28
Figure 8. Travel paths of the 86 S waves.....29	29
Figure 9. (a) Ray path through the velocity model.....32 (b) Path of a model ray across the refracting grid.	32
Figure 10. Modelling test P velocities with a single.....38 anomaly using a 10x10 grid.	38
Figure 11. Converging r.m.s. of travel time residuals.....40	40
Figure 12. Modelling test P velocities with a single.....42 anomaly using a 20x20 grid.	42
Figure 13. Modelling test P velocities with near surface....45 anomalies using a 10x10 grid.	45
Figure 14. Modelling P velocity zones test data with.....46 a 10x10 grid.	46
Figure 15. (a) P wave travel paths in the region of.....51 the VISP80 IV refraction profile. (b) P wave arrivals of set80.	51
Figure 16. (a) S wave travel paths in the region of.....52 the VISP80 IV refraction profile. (b) The S wave arrivals of set80.	52

Figure 17. (a) P wave travel paths in the region of.....	53
the SCoRE Line 2 refraction profile.	
(b) The P wave arrivals of set2.	
Figure 18. (a) S wave travel paths in the region of.....	54
the SCoRE Line 2 refraction profile.	
(b) The S wave arrivals of set2.	
Figure 19. (a) P wave travel paths in the region of.....	55
the SCoRE Line 3 refraction profile.	
(b) The P wave arrivals of set3.	
Figure 20. (a) S wave travel paths in the region of.....	56
the SCoRE Line 3 refraction profile.	
(b) The S wave arrivals of set3.	
Figure 21. (a) P wave travel paths in the region of.....	57
the SCoRE Line 10 refraction profile.	
(b) The P wave arrivals of set10.	
Figure 22. (a) P wave travel paths in the region of.....	58
the SCoRE Line 10 refraction profile.	
(b) The S wave arrivals of set10.	
Figure 23. (a) P wave travel paths used to construct.....	59
setnew.	
(b) The P wave arrivals of setnew.	
Figure 24. (a) S wave travel paths used to construct.....	60
setnew.	
(b) The S wave arrivals of setnew.	
Figure 25. The final P wave inversion velocity model.....	63
Figure 26. P velocities on a rotated 7x7 grid.....	66
Figure 27. P velocities on a 8x7 along strike grid.....	68
with a 161 Km offset cutoff.	
Figure 28. P velocities on a 8x7 along strike grid.....	70
with a 147 Km offset cutoff.	
Figure 29. The final S wave inversion velocity model.....	71
Figure 30. The final Poisson's ratio model.....	74
Figure 31. P wave inversion velocity model with a fixed.....	78
near surface layer.	

Figure 32.	(a) Upper crust from SCoRE Line 2.....	83
	(b) 8x7 grid results along Line 2.	
	(c) 6x5 grid results along Line 2.	
	(d) 7x7 rotated grid results along Line 2.	
Figure 33.	(a) Upper crust from SCoRE Line 3.....	85
	(b) 8x7 grid results along Line 3.	
	(c) 6x5 grid results along Line 3.	
	(d) 7x7 rotated grid results along Line 3.	
Figure 34.	(a) Poisson's ratio-Porosity relation for.....	88
	selected pore aspect ratios.	
	(b) P velocity against Poisson's ratio for	
	several rock forming compositions with	
	in-line results shown.	
	(c) P velocity against Poisson's ratio with all	
	tomographic results shown.	
	(d) P velocity against Poisson's ratio with well	
	constrained results shown.	
Figure 35.	Seismograms at Port Alberni Station.....	97
Figure 36.	Seismograms at Bowen Island Station.....	98
Figure 37.	Seismograms at Buttle Lake Station.....	99
Figure 38.	Seismograms at Campbell River Station.....	100
Figure 39.	Seismograms at Eliza Dome Station.....	101
Figure 40.	Seismograms at Estevan Point Station.....	102
Figure 41.	Seismograms at Haney Station.....	103
Figure 42.	Seismograms at Mount Grey Station.....	104
Figure 43.	Seismograms at Nanaimo Station.....	105
Figure 44.	Seismograms at Mount Ozzard Station.....	106
Figure 45.	Seismograms at Port Renfrew Station.....	107
Figure 46.	Seismograms at PGC Station.....	108
Figure 47.	Seismograms at Sechelt Station.....	109
Figure 48.	Seismograms at Saturna Station.....	110
Figure 49.	Seismograms at Mount Vedder Station.....	111
Figure 50.	Seismograms at Gonzales Station.....	112

Figure 51. Seismograms at Whistler Station.....113

Figure 52. Seismograms at Watts Point Station.....114

ACKNOWLEDGEMENTS

I would like to take this opportunity to thank my supervisors; George Spence, for his continual encouragement and guidance, and Gary Rogers, for his many insights and recommendations throughout the work.

I am extremely grateful to Tianson Yuan for answering the hundreds of computer questions I must have asked him. For the research data I am indebted to the Geological Survey of Canada.

For their friendship I must mention: Scott, Owen, Janine, Chandra and Mel; for their correspondence, humour and naan bread: Mark, Andy, Dave, Steve, Rob and the Price household.

I thank Ken, Val, Jo and Tugs for all their love and understanding these past three years.

CHAPTER ONE -TECTONIC AND GEOPHYSICAL FRAMEWORK

1.1 INTRODUCTION

The Lithoprobe southern Cordillera Transect used multidisciplinary means to study the crust and upper mantle structure of the southwestern Canadian Cordillera. A major part of this study were the Southern Cordillera Refraction experiments (SCoRE) conducted in 1989 and 1990. These experiments consisted of several ~300 km in-line refraction profiles.

Many of the shots from SCoRE89, SCoRE90, and several from the Pacific Northwest refraction survey, PACNW1, (a seismic refraction experiment conducted in northwest Washington) were recorded on the earthquake stations of the WCTN network. Seismic ray path coverage between the shots and stations extends beyond that of the in-line experiments of SCoRE and PACNW to cover southern Vancouver Island, the Georgia Strait and southwestern British Columbia. In addition to extended coverage over previous seismic experiments, the WCTN data set also offers S wave data which has not been modelled before over this region.

The objectives of this thesis are: (1) to extract information from the WCTN explosion data set on P velocities, S velocities and Poisson's ratio in the southern Insular and Coast Belts of the Cordillera, and then (2) understand how lateral variations in velocity and Poisson's ratio structure may be related to variations in the rocks physical properties.

1.2 TECTONIC SETTING

Many authors have detailed the evolution of the Canadian Cordillera (Monger and Price 1979; Coney et al. 1980; Monger et al. 1982; Gabrielse and Yorath 1989). The principal tectonic elements of this region are five belts. From east to west these are: the Foreland, Omineca, Intermontane, Coastal and Insular. The Cordillera is also divided into terranes. A terrane is recognized by its unique stratigraphy relative to neighbouring terranes and by the faults that border it. The boundaries between morphological belts are mostly, but not entirely, coincident with the major terrane boundaries (Gabrielse and Yorath 1989).

According to Monger et al. (1982) the Cordillera has been shaped by the accretion of two large composite superterranes during Mesozoic times. The first of these was the Intermontane Superterrane, which presently underlies the Intermontane Belt. It was accreted to North America about 175 Ma by eastward thrusting over the Proterozoic craton. The Omineca and Foreland Belts formed during and after the collision. The second allochthonous terrane was the Insular Superterrane colliding around 100 Ma, at which time the Intermontane terrane was an integral part of the North American continent. Monger et al. (1982) described the Coast Belt as a tectonic welt resulting from the collision.

The accretion of the superterranes took place within an overall tectonic setting in which the North American plate

overrode various oceanic plates, including the Kula and Farallon plates (Riddihough 1984). In the present tectonic regime the oceanic Juan de Fuca plate, which is a remnant of the former Farallon plate, is subducting beneath the west coast margin.

1.3 GEOLOGICAL SETTING

The study region stretches over the Insular and Coastal Belts (Figure 1)¹. In this region most of the Insular Belt is comprised of the Wrangellia terrane, which is characterized by late Paleozoic volcanic rocks (the Sicker Group) overlain by Triassic basaltic pillow lavas, flows, pillow breccias, and minor sediments of the Karmutsen Formation (Muller 1977). On southwestern Vancouver Island, two small terranes have been emplaced beneath Wrangellia as a consequence of Eocene plate motions. The Pacific Rim terrane is an Upper Mesozoic melange, and the Crescent terrane represents Eocene oceanic crust deposited in a marginal basin (Massey 1986).

The Coast Belt is divided into three tectonic elements

¹Location map of the refraction lines in the southwestern Cordillera. From SCORE89 lines 2 and 3 are shown, as is line 10 from SCORE90. The other surveys in the area are lines I and IV of VISP80 and PACNW1. Major geologic and tectonic features are: AF, Ashlu Creek Fault; TLF, Thomas Lake Fault; HF, Harrison Fault; CCBD, Central Coast Belt Detachment; BKFS, Bralorne-Kwoiek Creek Fault System; FRF, Fraser River Fault; FR-SCF, Fraser River-Straight Creek Fault; ROL, Ross Lake Fault; HOF, Hozameen Fault; PF, Pasayten Fault; BR, Bridge River; Ca, Cadwallader; Ch, Chilliwack; CR, Crescent Rim; Ga, Gambier; HL, Harrison Lake; Mt, Methow; PR, Pacific Rim; N, Nanaimo sediments; Sh, Shuksan; T, Tertiary sediments; Wr, Wrangellia.

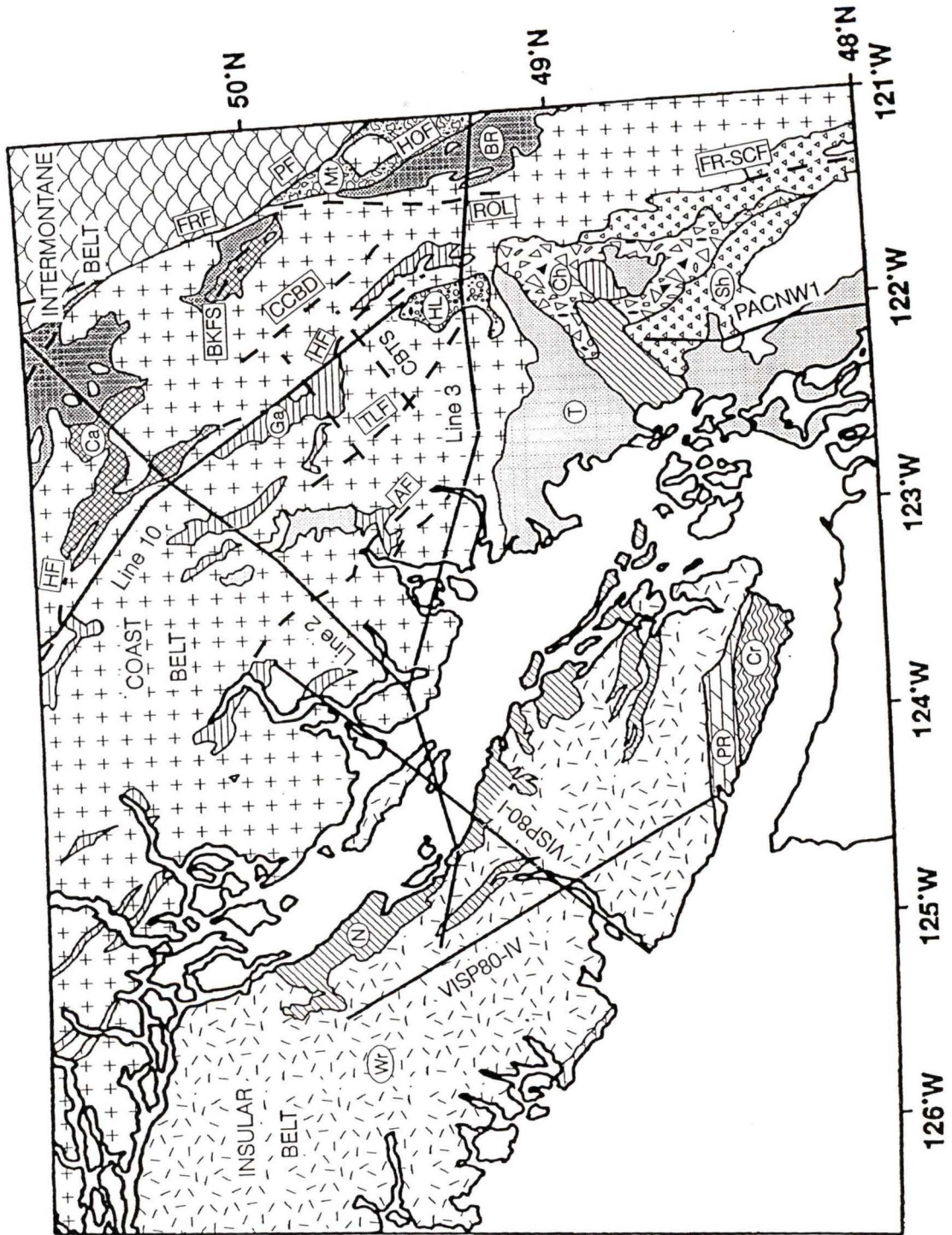


Figure 1

(Journeay and Friedman 1993): the Eastern Coast Belt (ECB), Central Coast Belt (CCB) and Western Coast Belt (WCB). The ECB is separated from the CCB by the Bralorne-Duffy Lake-Kwoiek Fault System. It contains mainly the stratified Methow, Bridge River and Cadwallader Terranes. In the CCB are high grade metamorphosed island arc and oceanic rocks separated by imbricate thrust faults. Associated with the thrust sheets are synorogenic and postorogenic plutonic complexes. The CCB is separated from the WCB by the Central Coast Belt Detachment (CCBD), a thrust fault that places middle to lower crustal rocks of the CCB over the WCB. The Western Coast Belt is primarily composed of Middle Jurassic to Miocene Age plutonic rocks intruding low-grade supracrustal arc sequences ranging in age from Middle Triassic to Late Cretaceous. The Coast Belt Thrust System (CBTS) within the WCB is a west vergent contractional belt formed at the eastern edge of the Insular Superterrane in the Late Cretaceous. It is interpreted as the suture between the Insular and Intermontane Superterranes.

Throughout the Coast Belt Late Cretaceous to Middle Tertiary northwest trending, dextral strike-slip faults can be found. Central Coast Belt rocks correlate with the Cascade Metamorphic core of the North Cascade Mountains but are offset by 80-110 Km of Late Eocene strike-slip (Monger 1986).

1.4 GEOPHYSICAL SETTING

1.4.1 REGIONAL SEISMIC SURVEYS

Refraction data shot prior to 1971 over the Southern Canadian Cordillera were synthesized by Berry and Forsyth (1975). Across strike refraction lines showed a decrease in upper crustal velocity from 6.5 km/s on Vancouver Island to 6.4 km/s in the Coast Belt. P_n arrivals were used to construct a time term surface for the base of the crust. A principal finding of the final model was a Moho depth of 23 km in the westernmost Coast Belt, increasing to 33 km along the eastern edge. However, the large receiver spacings meant that both vertical and lateral velocity variations were poorly resolved. Crustal arrivals were very poorly recorded on the mainland for a shot on Vancouver Island. Berry and Forsyth (1975) interpreted a crustal barrier or scattering zone located beneath eastern Georgia Strait, which prevented the propagation of energy within the crust.

In 1980 the Vancouver Island Seismic Project (VISP80) recorded refraction data along the length of the island and across the subduction zone (McMechan and Spence 1983, Spence et al. 1985). A two dimensional velocity model (McMechan and Spence 1983) along line IV (Figure 1) shows few lateral variations down to depths of ~20 km. The near surface velocities are between 5.5 and 6.0 km/s to a depth of 2 km, with the exception of the low velocities (5.0 km/s) at the southern end of the line. The velocity increases linearly from

6.4 km/s at a depth of 2.0 km to 6.75 km/s at 15.5 km depth. Line I of VISP80 (Figure 1) was interpreted by Spence et al. (1985). The upper crustal velocity beneath Vancouver Island ranges from 6.4 to 6.6 km/s and is 6.3 km/s beneath the mainland. The VISP80 data has been re-interpreted by Drew and Clowes (1990), but the new models they propose vary only with the initial interpretations at depths below 10 km.

1.4.2 SOUTHERN CORDILLERA REFRACTION EXPERIMENT

A major aim of the Lithoprobe Southern Cordillera Transect was to use multidisciplinary means to further understanding of crustal structure and terrane accretion in the Canadian Cordillera. One part of this study was the Southern Cordillera Refraction Experiments of 1989 and 1990, SCoRE89 and SCoRE90.

SCoRE89 covered the Insular, Coast and Intermontane Belts with a triangular arrangement of shots and receivers centred upon the Fraser River Fault System (Figure 1). Line 1 of the survey (which is less than 50 km west of the region shown in Figure 1), ran 330 km north-south along strike exclusively within the Intermontane Belt. Its northernmost shot was also a shot point for Line 2 which runs cross strike through the Coast Belt and on to Vancouver Island. The triangle is completed by Line 3, the southernmost leg, spanning 330 km, mainly within the Coast Belt. Interpretation has been undertaken along the lines using travel time inversion and

amplitude forward modelling (Zelt et al. 1992, McLean 1994, Zelt et al. 1993). The largest shots were at the line ends and midpoints. In addition, three shots were fired at the centre of the triangle. These shots were recorded along all the lines. The resulting data set allows for three dimensional modelling of the crust and upper mantle using tomographic methods (Zelt et al. 1994). SCoRE90 investigated structure mainly in the southeastern Cordillera (Kanasewich et al 1994). In addition, the westernmost line, Line 10, ran 350 km along strike within the Coast Belt (O'Leary et al. 1994).

Line 3 (Figure 1) was interpreted by Zelt et al. (1993). The final model shows a near surface layer, which is on average 1.2 km thick. The Georgia Basin is represented by low velocities in the model. Upper crustal velocities beneath Vancouver Island range from 6.25 to 6.4 km/s. This is in good agreement with previous studies of the area (Spence et al. 1985, Drew and Clowes 1990). From the Insular-Coast Belt boundary to the centre of the Coast Belt, the upper crustal velocities at 6.2-6.4 km/s are slightly lower than those of Wrangellia. The position of this zone correlates well with the Jurassic and Cretaceous plutonic overlap assemblages of the WCB. Farther east velocities in the upper crust decrease again to 6.10-6.20 km/s, remaining low to the end of the line. This transition concurs with the westernmost surface exposure of the Harrison Lake Terrane. The middle crust velocity also decreases across the Harrison Fault from 6.6-6.9 km/s in the

west to 6.35–6.45 km/s east of the fault. The authors conclude that Wrangellia lies to the west of the Harrison Fault in the middle crust and to the west of the Coast Belt in the upper crust. This interpretation leaves the eastern limit of Wrangellia in the lower crust uncertain. However, lower crustal velocities also decrease across the Harrison Lake Fault region. The eastern extent of Wrangellia will be discussed again below in relation to the Line 10 results (O'Leary et al. 1994).

Line 2 (Figure 1) was interpreted by McLean (1994). The upper crust beneath Vancouver Island has a velocity ranging from 6.3 to 6.4 km/s; in the Coast Belt this reduces to 6.3 km/s. To the east of the Harrison Fault the upper crustal velocity decreases again to 6.0 km/s.

Line 10 is a 350 km along strike profile in the Southern Coast Belt (Figure 1). The inversion was performed by O'Leary et al. (1994). The principal structural features of the model are a near surface layer varying in depth between 0.5 and 3.0 km, with an average P velocity of 4.40 km/s, and the upper, middle and lower layers of the crust, each approximately 10 km thick. The upper crust ranges in velocity between 6.05 and 6.35 km/s. The middle and lower crust have average velocities of 6.4 and 6.6 km/s, respectively. The Moho lies at a depth of approximately 35 km. The collision zone between the Insular and Intermontane Superterrane is believed to be situated close to the profile. Two collision zone models have been proposed

based on reflection data: (i) a crustal delamination model in which Wrangellia was displaced over the terranes below (Monger and Journeay 1992) and (ii) a crustal wedging model in which Wrangellia interfingers the Intermontane Superterrane throughout the crust east of the Harrison fault (Varsek et al. 1993). The lack of higher Insular velocities within the crust suggest that the Insular Superterrane does not extend as far east as Line 10 and so favours the crustal delamination model.

CHAPTER TWO - DATA ACQUISITION AND PROCESSING

2.1 Introduction

The Western Canadian Telemetered Network (WCTN) in Southwestern British Columbia recorded explosion shots from Lithoprobe's Southern Cordillera Refraction Experiment (SCoRE) in 1989 and 1990 and from the USGS Pacific Northwest Refraction Survey in 1991. The 18 WCTN stations received detectable arrivals from 24 shots, not including shot locations that were used more than once. WCTN uses a GEOS satellite clock for timing accuracy and is digitized at 60 samples/second. The geographical distribution of these shots and stations is shown in Figure 2. Table 1 lists the receiver locations, and Table 2 gives the shot locations and sizes.

No.	Station	Lat.	Long.	Elev.(km)
1	*Port Alberni (ALB)	49.2718	-124.8277	0.0260
2	*Bowen Island (BIB)	49.4094	-123.3100	0.0370
3	*Buttle Lake (BTB)	49.4683	-125.5214	1.6400
4	*Campbell River (CBB)	50.0320	-125.3638	0.3170
5	Eliza Dome (EDB)	49.8737	-127.1198	0.1890
6	Estevan Point (ETB)	49.3763	-126.5380	0.0010
7	*Haney (HNB)	49.2745	-122.5792	0.1830
8	*Mount Grey (MGB)	49.0000	-124.6975	1.3000
9	*Nanaimo (NAB)	49.2225	-124.0036	0.2560
10	Mount Ozzard (OZB)	48.9603	-125.4928	0.6710
11	*Port Renfrew (PFB)	48.5750	-124.4444	0.4650
12	*PGC (PGC)	48.6500	-123.4505	0.0050
13	*Sechelt (SHB)	49.5930	-123.8805	1.1430
14	*Saturna Island (SNB)	48.7760	-123.1712	0.4080
15	Mount Vedder (VDB)	49.0261	-122.1028	0.4040
16	*Gonzales (VGZ)	48.4139	-123.3244	0.0670
17	*Whistler (WHB)	50.1281	-122.9553	0.6950
18	*Watts Point (WPB)	49.6481	-123.2083	0.2800

Table 1: Location of the 18 stations used to produce the data and their elevations. Asterisks denote those stations used in the final P and S wave data sets.

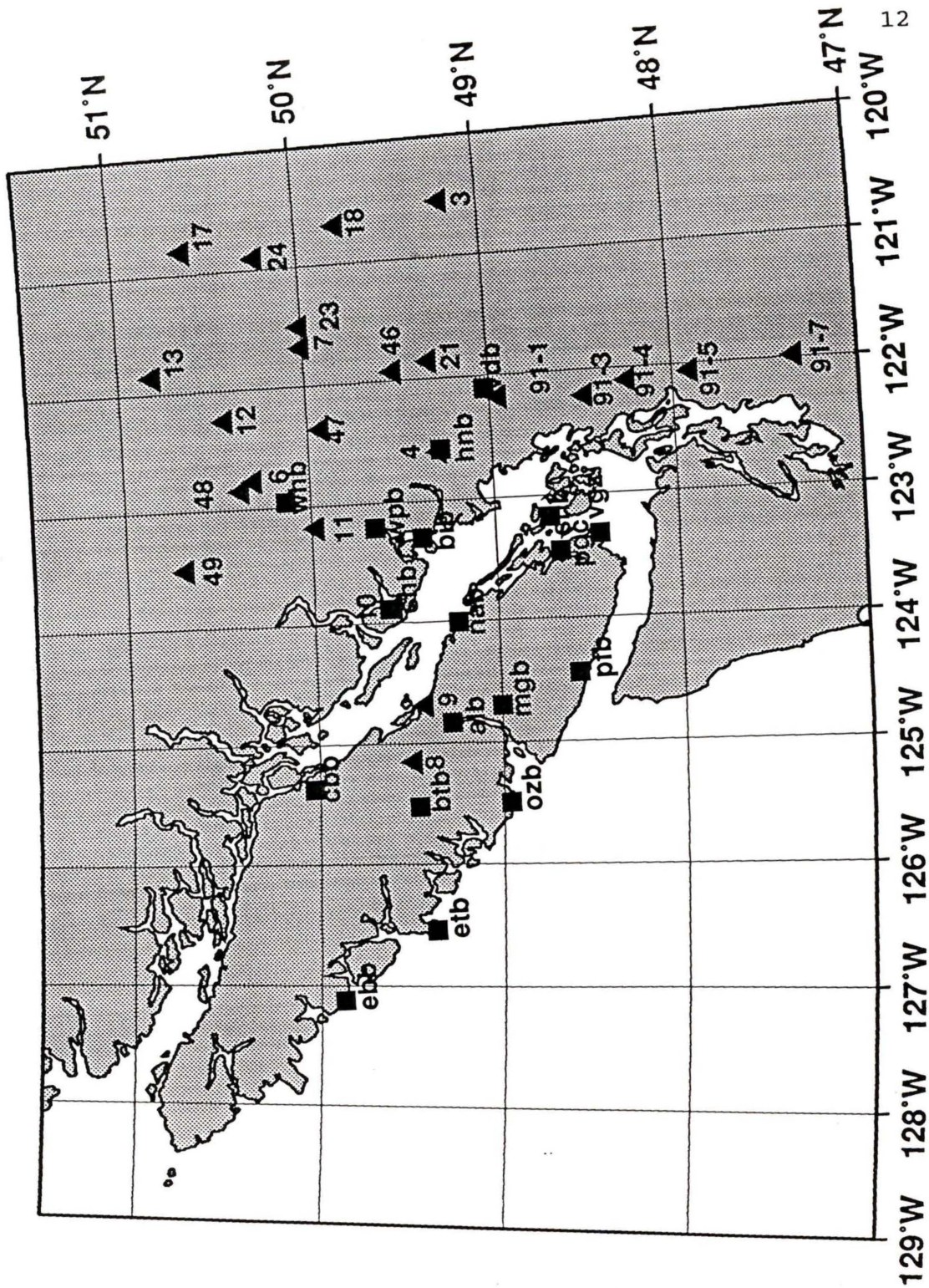


Figure 2: Location map showing the shotpoints (triangles) and receivers (squares) used to obtain the initial data set. The locations of the 18 stations are listed in Table 1, with the shot locations listed in Table 2.

SHOT SITE	LATITUDE	LONGITUDE	ELEVATION (m)	DEPTH (m)	CHARGE (kg)	SIZE
3	49.1992	-120.5432	1028	30	1800	
*4	49.2943	-122.5969	180	30	800	
*6	50.3024	-122.7714	198	30	200	
*7	50.0051	-121.6005	250	30	800	
*8	49.4813	-125.1517	562	30	1800	
*9	49.4206	-124.6872	94	30	200	
*10	49.5686	-123.8638	608	30	200	
*11	49.9711	-123.1897	601	30	200	
*12	50.4463	-122.2552	1071	30	800	
13	50.8141	-121.8590	496	30	200	
17	50.6150	-120.8048	1180	30	800	
18	49.7755	-120.6778	1042	30	200	
*21	49.3178	-121.8708	60	30	200	
*46	49.5144	-121.9274	375	42	2500	
*47	49.9228	-122.3649	100	32	200	
*48	50.3761	-122.8479	221	30	2500	
49	50.6866	-123.5066	716	42	800	
*23	50.0051	-121.5989	337	42	1800	
24	50.2827	-117.7444	1053	42	200	
*91-1	48.7252	-122.1806	606	30	1818	
91-3	48.4785	-122.2034	279	30	909	
91-4	48.2424	-122.1064	114	30	1364	
91-5	47.8993	-122.0625	42	30	909	
91-7	46.7648	-121.9569	256	30	909	

Table 2: Location and charge sizes for the 24 shots used to produce the initial data set. Asterisks denote those shots used in the final P and S wave data sets.

2.2 FILTERING

Spectral analysis was performed on P and S arrivals within the data set. Figure 3 shows the amplitude spectrum of P wave arrivals from shot 8. A 35 second time window around the arrivals was used to determine the spectrum. Signal frequencies fell within a 3-20 Hz bandwidth and the P wave data set was filtered accordingly. The amplitude spectrum of a 50 second time window around the S arrivals from shot 8 is shown in Figure 4. Most of the signal is contained within the 3 to 12 Hz range.

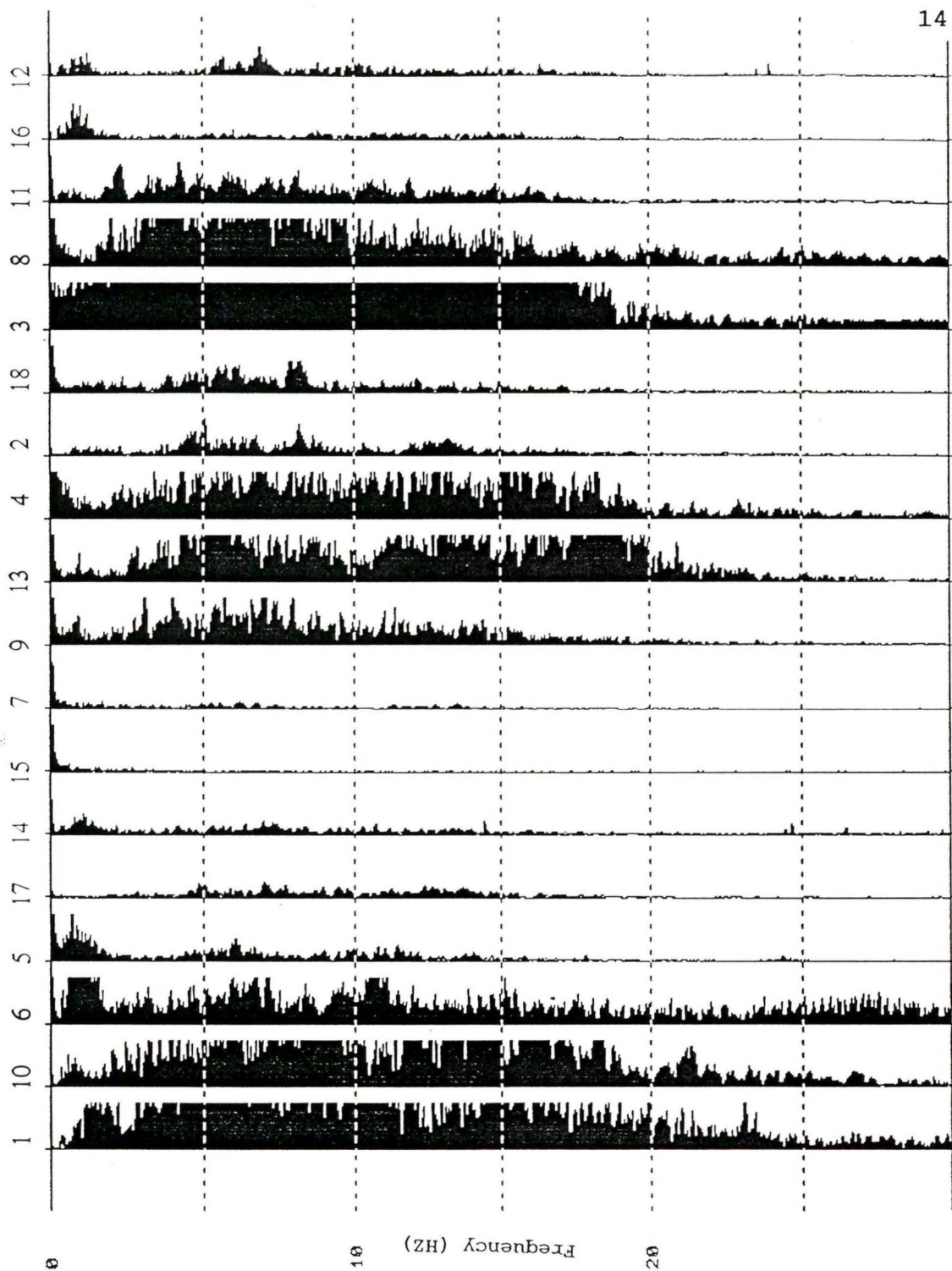


Figure 3: Amplitude spectra for P arrivals from shot 8. Obtained using a 35 second unfiltered time window centred on the arrivals. The vertical axis is in Hertz and the traces are spaced equidistantly along the horizontal axis. The station i.d numbers used are the same as those in Table 1. Most of the signal is contained within a 3-20 Hz range.

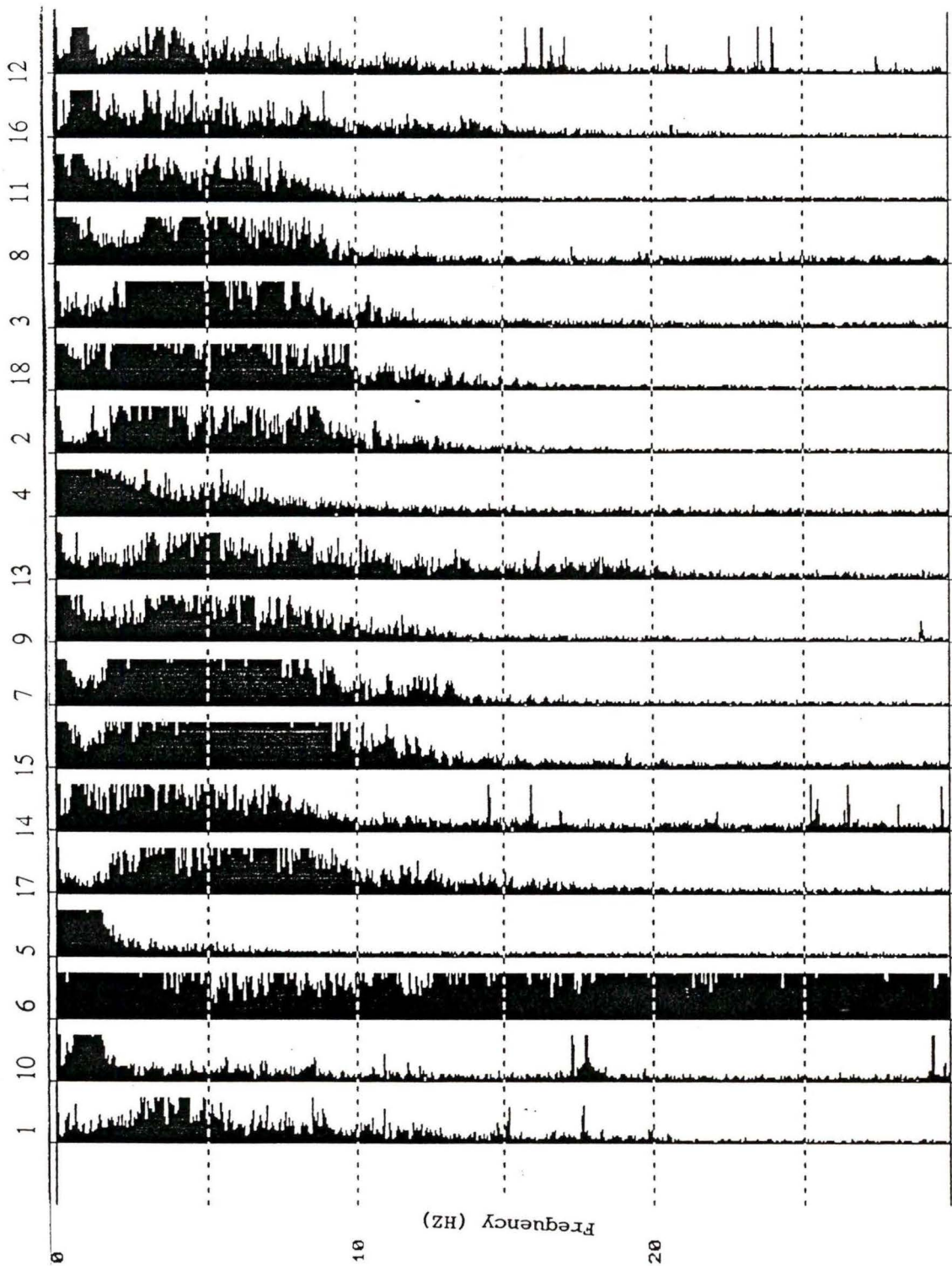


Figure 4: Amplitude spectra for S arrivals from shot 8. Obtained using a 50 second unfiltered time window centred on the arrivals. The vertical axis is in Hertz and the traces are spaced equidistantly along the horizontal axis. The station i.d numbers used are the same as those in Table 1. Most of the signal is contained within a 3-12 Hz range.

S waves were picked with the aid of both the 3-7 and 3-20 Hz filters. The removal of the higher frequencies meant that the exact arrival time is often not well resolved using the 3-7 Hz filter, although the S wavepacket is much easier to discern. As an example Figure 5 shows the three S wave arrivals at the Campbell River station using both filters.

2.3 Initial data characteristics

The P arrivals vary greatly in quality with some of the shots being detectable at only a few stations, while others are not found at all. Both emergent and impulsive arrivals are observed. S wave arrivals are noisier than the P, but are discernable for most shots. Arrivals to an offset of 200 km are seen on most P wave seismograms. Beyond this offset, P arrivals are often not visible.

Most shots were located on the mainland while the receivers were farther west. The mainland stations and those in the Georgia Basin detected most arrivals. The Vancouver Island stations detected fewer arrivals compared to inland stations. The two shots that were fired on the Island were detected at all stations with the exception of one inland station.

The seismograms were plotted against distance by both the station they were received at and also by the shot which produced them. In this manner large scale anomalies could be recognized. The arrivals at the Saturna Island Station were

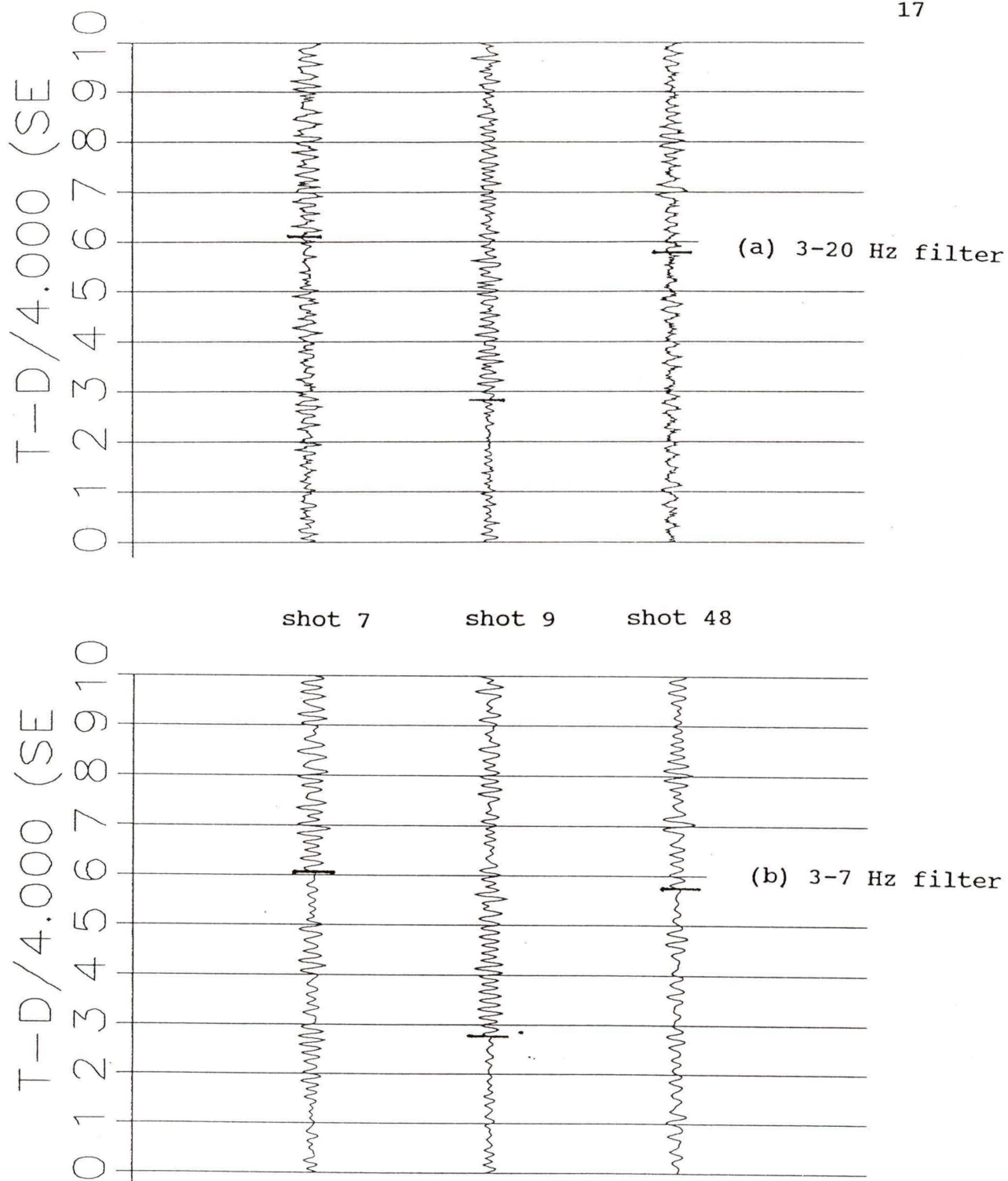


Figure 5: S wave arrivals at the Campbell River station filtered using (a) the 3-20 Hz filter and (b) the 3-7 Hz filter. The traces are plotted with a reducing velocity of 4 km/s and equidistantly along the horizontal axis. The narrower bandwidth filter was often found to help discriminate the S wavepacket from noise. The travel time picks are shown by the horizontal solid lines on the traces.

seen to be consistently slower than those at other stations for similar offsets, and the Mount Vedder Station arrivals varied greatly over time for similar offset distances. The West Coast stations, Estevan and Eliza Dome, were found to be very noisy.

CHAPTER THREE DATA ANALYSIS AND INTERPRETATION PROCEDURES

3.1 INTRODUCTION

The problem of extracting information from explosion data is similar to that of resolving structure from earthquakes detected on a network. However, these data have an advantage in that the precise location and time of the sources are known, whereas the epicentre coordinates, focal depth and origin time still have to be determined when working with earthquake data.

There are a number of methods that invert travel time data, from either explosions or local earthquakes, to determine crustal velocity structure. The techniques differ in how the real earth is modelled and how theoretical travel times through that model are calculated. A short review of some possible methods is presented below.

The time term technique was developed to model a layer (or multiple layers) over a refracting interface (Scheidegger and Willmore 1957, Berry and West 1966). The travel time T_{ij} is expressed as

$$T_{ij} = a_i + a_j + \frac{dis_{ij}}{V} \quad \text{Eq. 1}$$

where dis_{ij} is the distance between source and station, V is the velocity below the refracting interface and a_i and a_j are

the time terms of the source and receiver. The time terms are a function of both velocity above the refracting layer and depth. They can be considered as the time difference between a critically refracted ray path through the layer(s) above the bottom refracting layer and the time for a wave to travel the horizontal offset distance. Three assumptions are made when applying the time term method (Berry and West 1966): (1) velocity varies only with depth within the critically refracted ray cone, (2) the velocity of the base refractor is constant, (3) the slope and curvature of the refracting surface is small. Each observation has an equation in the form of Equation 1 and so a set of simultaneous linear equations can be formed. The unknowns of the data set are the time term and the refractor velocity. The basic time term may be modified to allow for the modelling of more complex structures than those abiding by the above assumptions (Raitt et al. 1969, Zervas and Crossen 1986). Equation 1 can be revised to accommodate: (1) a velocity gradient within the refractor, (2) azimuthal anisotropy in the refractor, (3) a dip in the refractor interface. Zervas and Crossen (1986) applied both the modified and unmodified time term methods to measurements in the State of Washington. Moho P wave arrivals from local earthquakes were recorded on the telemetered network of receivers. The unmodified method was employed over various subregions of the state. The three modified methods were then used over the west and the east of the state independently. It

is advantageous to use several time term methods not only to find which fits the data best but also because of the trade off between crustal velocity and depth implicit within the time term.

Thurber (1983) presented a method for estimating the three dimensional earth structure using data received on an earthquake array. The earth structure is represented by velocities at a large number of discrete points within a three dimensional volume. The velocity of any given point may be interpolated from the surrounding velocity points. The method makes use of an accurate and efficient approximate ray tracing routine rather than analytically mapping rays through the model. The procedure joins the source and receiver with a number of circular arcs; the travel time along each arc is then calculated using the velocity model. The shortest travel time is used in the least squares inversion. Crustal structure has been modelled by Aki and Lee (1976) using several layers of rectangular blocks. Each block is described by its invariant dimensions and by a perturbation of its P wave slowness. The study area for local earthquakes is small enough that a cartesian coordinate system may be used, which may be positioned to align one axis with faults or surface geology transition zones. The input data for the model consists of P wave travel times from local earthquakes gathered on a seismic network. An equation for each observed P wave arrival time is formulated in terms of the perturbation to the structural

model and the source location and origin time. A simple application of Pythagoras' theorem is utilized to calculate the travel time through the model, and perturbations of the slowness in each block in turn perturb this time. A further simplification is made in that not all the blocks that the ray passes through are sampled. Only the block which contains the most ray path within each layer is selected. The data matrix is solved using a damped least squares method.

Zhu and Ebel (1994) use a tomographic refraction ray tracing method in which the earth is modelled by a block array overlain by several single velocity layers. A starting model was obtained by plotting the apparent velocity against the epicentral distance, utilizing all direct P waves including the basement refraction P_g , a mid-crustal refraction P^* , and the mantle refraction P_n . From this graph the crossover distances and average apparent velocities are used to construct a plane layered starting velocity model. The Zhu and Ebel method (1994) inverts the data in a layer-stripping technique. A base depth is chosen above which are plane layers, and below which is a grid of velocity blocks. A generalized SVD technique is employed to compute the inversion for velocities within the grid and in the plane layer above the grid.

In this thesis a three dimensional inversion model similar to that of Zhu and Ebel (1994) was applied to the WCTN data set. The modified method is described in Section 3.4.

3.2 TRAVEL TIME PICKING

The seismograms were plotted against distance in a 7 second time window using a reducing velocity of 7 km/s for the P arrivals and 4 km/s for the S arrivals. The picks were made concurrently from plots showing the seismograms by the shot they were fired from, and by the station they were recorded at. All arrivals were trace equalized. To correct site elevations to a sea level datum, a statics correction of the form

$$\frac{H_s}{V_1} \sqrt{1 - \frac{V_1^2}{V_2^2}} + \frac{H_r}{V_1} \sqrt{1 - \frac{V_1^2}{V_2^2}} \quad \text{Eq.2}$$

was applied to each trace. Where H_s is the height of the shot above sea level, H_r is the height of the receiver above sea level, V_1 is the upper layer velocity (set at 6.0 km/s) and V_2 is the velocity of the refracting layer (set to 6.5 km/s). All arrivals were picked by hand. The S wave arrivals were concurrently picked from data filtered using band widths of 3-20 Hz and 3-7 Hz. The estimated error on the P wave arrivals was between 25 and 100 milliseconds and on the S arrivals between 100 and 200 milliseconds.

3.3 CONSTRUCTION OF THE INVERSION DATA SETS

The final data set was produced from 14 shots within the Coast and Insular Belts. These were recorded at 14 stations of the WCTN. The data set consisted of 116 P wave arrivals and 86

S wave arrivals. The choice of arrivals was not only dependent upon data quality, but also on other criteria such as offset and location; these criteria are reviewed below, as are some other constraints imposed by the data set upon the modelling.

A total of 24 shots was recorded at 18 WCTN stations. Some of the shots were detectable at only a few stations because of the large source to receiver distances or poor shot coupling. Stations and shots with less than three P wave arrivals were deleted from the data set. This included the smaller shots of Line 1 and the noisy stations of Vancouver Island's West Coast, Estevan, Eliza Dome and Ozzard.

In any kind of tomographic inversion, a high ray path density is preferred in the region being studied. The ray sampling east of a latitude 122 (Figure 2) is dependent on four shots; 3, 17, 18 and 24. To include them in the data set would greatly extend the inversion area and number of inversion parameters with only a small increase in information. These shots were therefore excluded from the data set. For similar reasons most of the Pacific Northwest refraction survey shots were also removed.

There are large variations in the source and receiver offsets; these range from under 10 km to the order of 250 km. This implies a large range of depths will be sampled by the seismic rays. Thus, a small offset shot would usually sample shallower crust and lower velocities than a larger offset shot and vice versa.

Arrivals up to an offset of 200 km are seen on most P wave seismograms. Beyond this offset arrivals are often not visible. Figures 6(a) and 6(b) show the velocity model and corresponding travel times for Line 2 (McClean 1994). The figures show that upper crustal P arrivals are the first arrivals up to an offset of approximately 175 km, while at increasing offsets first arrivals are from beneath the Moho, with a velocity of about 8.0 km/s. From this it is recognized that the WCTN stations did not record reliable deep structure arrivals or secondary P arrivals. A high shot/station offset cutoff² of 175 km was applied to the data set, and a low cutoff 21 km. Arrivals within this window should not have penetrated below the upper crust. Modelling of the lithosphere from the data set is then restricted to the upper crust.

For the most part, shots were located in the eastern region and receivers in the west. The mainland stations and those in the Georgia Basin detected most arrivals. The Vancouver Island stations detected less utilizable arrivals due to increased distances from the shots compared with inland stations. The two shots that were located on the Island were detected at all stations with the exception of one inland station. The result was a concentration of ray density in a core area while outlying regions were covered more sparsely.

²The values of 21 and 175 km were convenient to use in the computer programs handling the data, and are only approximations serving to define the offset bandwidth. In Section 4.3.2 the effects of changing the upper limit is investigated.

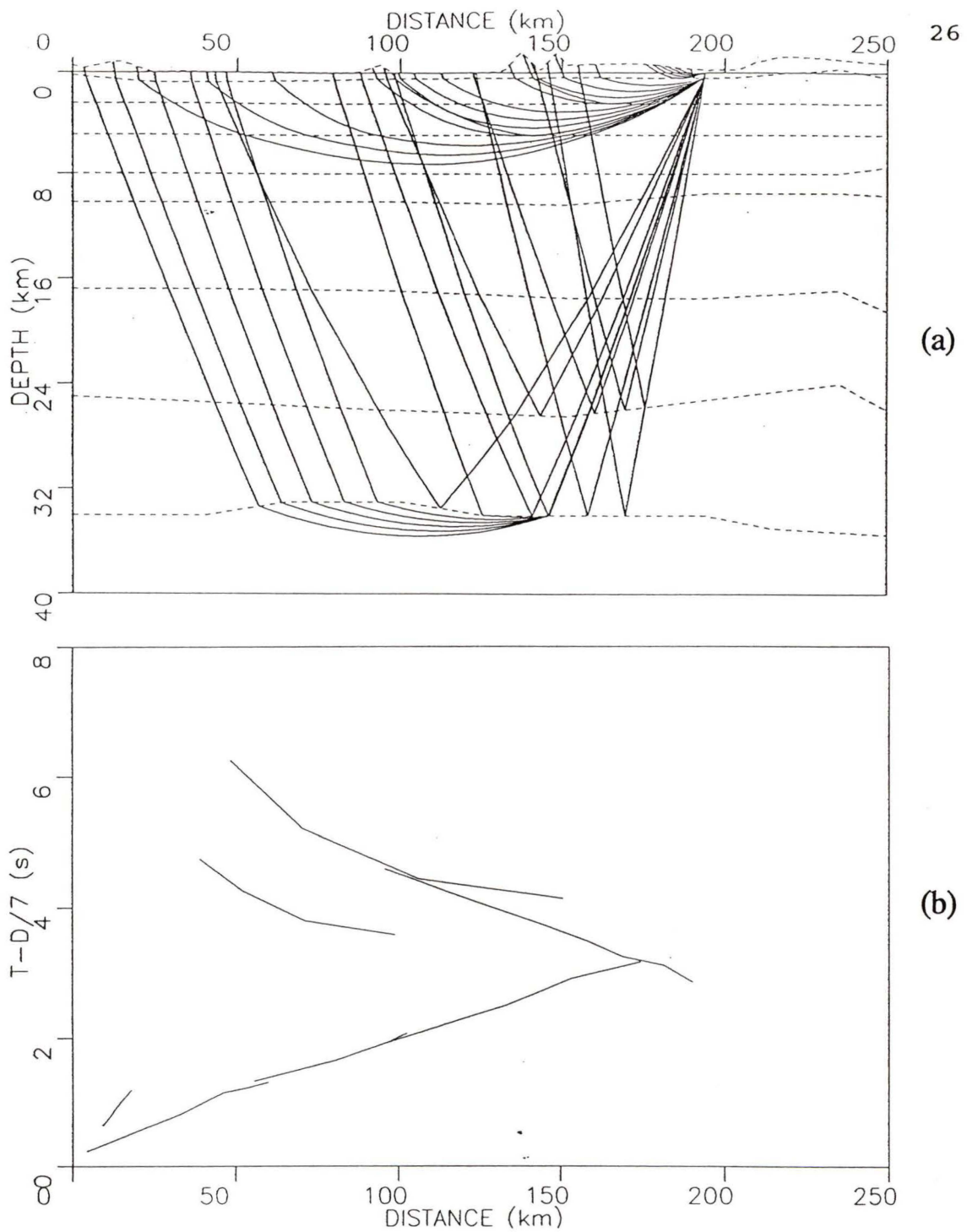


Figure 6: (a) Travel paths through the SCoRE Line 2 model of McLean (1994). The location of this line is shown in Figure 1. The offset distances are measured eastward from shotpoint 8 along the surface of the model. The ray paths shown have been traced westward from shotpoint 12. (b) Theoretical travel times from shotpoint 12 (McLean 1994). The offset distances are measured westward from shotpoint 12. First P wave arrivals up to an offset of 175 km are from the upper crust, beyond here the first arrivals have penetrated deeper structure.

The travel paths of the P wave data set are shown in Figure 7. Coverage is best over the Coast Belt and Georgia Strait. Several areas of good coverage have not been surveyed before by previous refraction lines. In particular the southern part of the Georgia Strait and the Gulf Islands. The shot/station combinations at which travel times were picked are listed in Table 3, and the offset distances and arrival times are listed in Appendix 2. The travel paths for the S waves are shown in Figure 8 and the list of S wave picks in Table 4. The S wave inversion data set offset distances and arrival travel times are listed in Appendix 3.

The study region extends over an area 300 Km by 250 Km and therefore the curvature of the earth was taken into account.

The use of 14 shots and 14 stations means that the near surface layer is sampled at only 28 locations. Isolated near surface velocity anomalies at either a shot or a station need to be separated from crustal velocities in the model.

As previously mentioned, much geological and geophysical work has been carried out in the study region. This knowledge should be considered when choosing how best to model the real earth, without biasing the initial conditions of the model. For example, the northwest to southeast strike of the belts and estimated velocity boundaries suggested that modelling boundaries along the geological strike would be prudent.

	4	6	7	8	9	10	11	12	21	23	46	47	48	9 1
alb	x			x	x	x	x							
bib	x	x	x	x	x	x	x	x	x	x	x	x		x
btb				x	x	x	x							
cbb				x	x	x								
hnb		x	x		x	x	x	x	x	x	x	x	x	x
mgb	x			x	x	x	x							x
nab	x	x		x	x	x	x	x						x
pfb	x			x	x	x	x							x
pgc	x			x	x	x		x			x	x		x
shb	x	x	x	x	x		x	x	x	x	x	x		x
snb	x		x	x	x	x	x			x	x	x		x
vgz	x			x	x	x	x				x	x		x
whb	x	x	x	x	x	x	x	x	x	x	x	x	x	x
wpb	x	x	x	x	x		x	x	x	x	x	x	x	x

Table 3: The number of P wave travel picks made for each shot point. The shot numbers are shown along the top row and the stations are listed in the left hand column. In the final P wave data set 14 shots and 14 stations were utilized.

3.4 INVERSION METHOD

The real earth was modelled as a near surface velocity layer of uniform thickness over a refracting velocity grid. The procedure solved for the near surface velocity at each shot and station site and for each element of the refracting grid. The near surface upper layer at each site and each element of the block array were assigned starting velocities. Source and receiver location were specified on the surface of the model at S and R, respectively. A ray is traced from the

	4	6	7	8	9	10	11	12	21	23	46	47	48	9 1
alb			x	x	x					x				
bib			x	x	x	x	x			x		x	x	
btb			x	x			x			x		x	x	
cbb			x		x								x	
hnb		x	x	x	x	x		x	x	x	x		x	
mgb			x		x	x				x				
nab		x	x	x		x	x	x	x	x			x	
pfb			x	x	x		x			x			x	x
pgc			x	x	x	x	x	x		x	x			
shb				x					x	x	x	x		
snb					x		x							x
vgz			x	x			x			x			x	x
whb				x		x	x	x	x			x	x	
wpb			x	x	x		x	x			x	x		x

Table 4: The number of S wave travel time picks made for each shot point. The shot numbers are shown along the top row and the stations are listed in the left hand column. In the final S wave data set 13 shots and 14 stations are utilized.

shot to the refracting layer, B, using Snell's law. The ray crosses the grid and is then refracted again to the receiver at R (Figure 9a). While the ray is crossing the grid, between P and Q, the distance travelled within each element of the grid was then calculated (Figure 9b). For each ray path many of the blocks are not crossed and so contribute nothing to the travel time. The travel time for such a path is

$$T = \frac{H}{\cos\theta_s} S_s + \frac{H}{\cos\theta_r} S_r + \sum_{k=1}^n D(k) S_k \quad \text{Eq. 3}$$

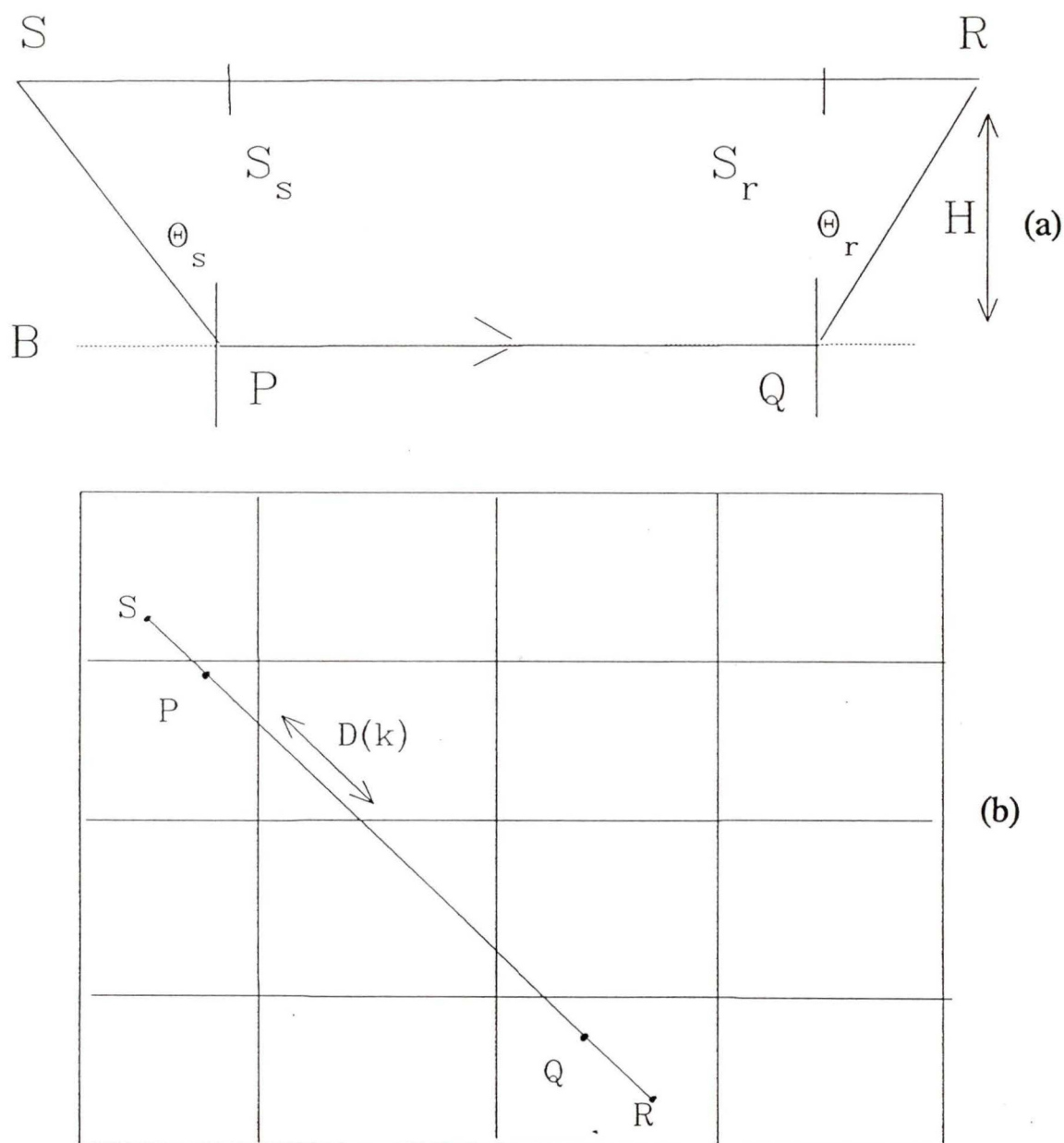


Figure 9: (a) Ray path through the velocity model. From a shot point at S the ray travels to the refracting grid B. The ray enters the refracting layer at point P. The ray crosses the refracting grid (Figure 9b) before arriving at the model surface again at R. Here H is the layer depth, θ_s and θ_r are the critical angles for the source and receiver, and S_s and S_r are the slownesses of the upper velocity layer. (b) Path of a model ray across the refracting grid. Between P and Q the ray travels a distance $D(k)$ through each element.

where H is the layer depth, θ_s and θ_r are the critical angles for the source and receiver, S_s and S_r the slownesses of the upper velocity layers, $D(k)$ the fractional distance travelled through a grid element and S_k the slowness of that element.

The unknowns in the equation are the slownesses of the upper velocity layer, S_s and S_r , and the slownesses of the grid elements, S_k . In the model the depth H is assigned a value by the user rather than being left as a parameter.

For perturbations of slowness δS_k the equation for the travel time residual $\delta(T)$ is

$$\delta T = \frac{H}{\cos\theta_s} \delta S_s + \frac{H}{\cos\theta_r} \delta S_r + \sum_{k=1}^n D(k) \delta S_k \quad \text{Eq. 4}$$

The experimental data consist of observed travel times for known shot and receiver positions. An equation in the form of Equation 4 was produced for each observational travel time to render a set of simultaneous linear equations in matrix form

$$A \cdot S = T \quad \text{Eq. 5}$$

For a data set of N experimental travel times and a grid of J elements, A will be an $N \times (J+NS)$ matrix of partial derivatives, where NS is the number of shot and station sites

$$A(n, 1) = \frac{H}{\cos\theta_1}$$

..

..

$$A(n, NS) = \frac{H}{\cos\theta_{NS}}$$

$$A(n, k+NS) = D(k) \quad k=1, J$$

Eq. 6

S will be the solution vector for the J slowness perturbations of the velocity grid and the single upper layer. T is an N x 1 vector of the travel time residuals, $\delta(T) = T^{\text{obs}} - T^{\text{mod}}$ where T^{obs} is the observational travel time and T^{mod} the travel time through the current model.

The residual travel times are recalculated through a series of iterations. After each iteration, the newly calculated slownesses are applied to the velocity model to update it. Rays are then traced through the new model to produce another matrix of partial derivatives and travel time residuals. This matrix is then solved for the slownesses as before and the iterative procedure continues until the root mean square, r.m.s., of the residual travel times reaches a desired accuracy.

Equation 5 is solved using a damped least squares method (Aki and Richards 1980). As there are more observations than parameters the data set is overdetermined. With the introduction of a weighting factor, the damping stops large variations in the parameters. The modified normal equations

for this method are

$$(A^T A + W) \cdot \delta S = A^T \cdot \delta T \quad \text{Eq.7}$$

W is the diagonal weighting matrix,

$$W = V_{ALL} \begin{pmatrix} \frac{V_{TT}^2}{V_1^2} & 0 & 0 & \dots \\ 0 & \frac{V_{TT}^2}{V_2^2} & & \\ \vdots & & & \\ \vdots & & & \end{pmatrix} \quad \text{Eq.8}$$

where V_{ALL} is the overall damping factor, V_{TT}^2 is an estimate of the variance of the travel time residuals and V_i^2 is an estimate of the variance of the slowness parameter i .

Variations in the slowness parameters are damped by increasing the magnitude of the corresponding weighting element within W. The elements of W are inversely proportional to the individual variances of the slowness V_i and so a small variance will result in a large damping factor and small changes in the slowness.

The substantial latitude range of shot and station sites was accounted for in the same manner as Zhu and Ebel (1994). When projecting the site location, in geographical coordinates, onto the cartesian grid surface a factor of $\text{Cos}(\beta + \sigma\beta) / \text{Cos}\beta$ was multiplied into the east-west components of the sites cartesian coordinate. Here, β is the latitude at the

grid origin and $\sigma\beta$ is the latitudinal displacement from the origin.

The model used in the thesis varied from that of Zhu and Ebel (1994) in two respects: (1) the thesis model had only one refracting layer, whereas Zhu and Ebel (1994) used several, (2) the starting model was obtained from previous refraction interpretations plus new in-line refraction results, rather than apparent velocities estimates from the data set.

3.5 INVERSION METHOD TESTING

Before the inversion program was used with the data set a series of tests were run using artificial data. The aim of these tests was twofold; firstly, they attempted to reveal the best conditions under which to run the program with real data and, secondly, they provided an indication of the reliability of those results. The program tests were designed to answer a number of questions:

- How many grid cells should be used over the study area ?
- What path density is required within each cell ?
- When and to what degree should damping be applied ?
- Are there significant edge effects to the model results ?

The refracting surface was covered by a cartesian grid 300 km in the horizontal and 240 km in the vertical.

In limiting the data set to P arrivals within a 21 to 175 km offset all arrivals should be turning rays in the upper crust which refract at the near surface-upper crust boundary,

and so a single layer is used in the model. The depth of the near surface layer is not a parameter as in the routine of Zhu and Ebel (1994). Inverting for the near surface layer velocity alone will provide a measure of the travel time in this layer. To set the depth of the near surface layer estimates from Zelt et al. (1993), O'Leary et al. (1994) and McLean (1994) were used. The initial value chosen³ was 1.5 km.

The spatial resolution of a given cell can be tested using an artificial data set with a velocity anomaly in that cell against a homogenous velocity background. The routine was then run to find out whether the anomaly remained localized or contaminated other cells. Artificial data travel times were generated from a known test model using the actual shot and receiver distribution and calculating travel times for only those shot-receiver combinations which had observed travel times.

In initial tests, a 10x10 grid was used over the study area. The test model consisted of a homogenous velocity background of 6.3 km/s with a velocity anomaly of 7.0 km/s in the cell (D,6)⁴. The starting model consisted of a uniform 6.0 km/s grid. Figure 10 shows the inversion results after 50 iterations and indicates that the velocities of the refracting

³The near surface layer thickness of 1.5 km also provided low travel time residual r.m.s. values in tests with the observational data set. Results in the velocity grid are not greatly affected by a depth change of 0.5 km in the upper layer.

⁴The element D,6 was chosen for the site of the anomaly due to its typical ray coverage for the 10x10 grid (Table 5).

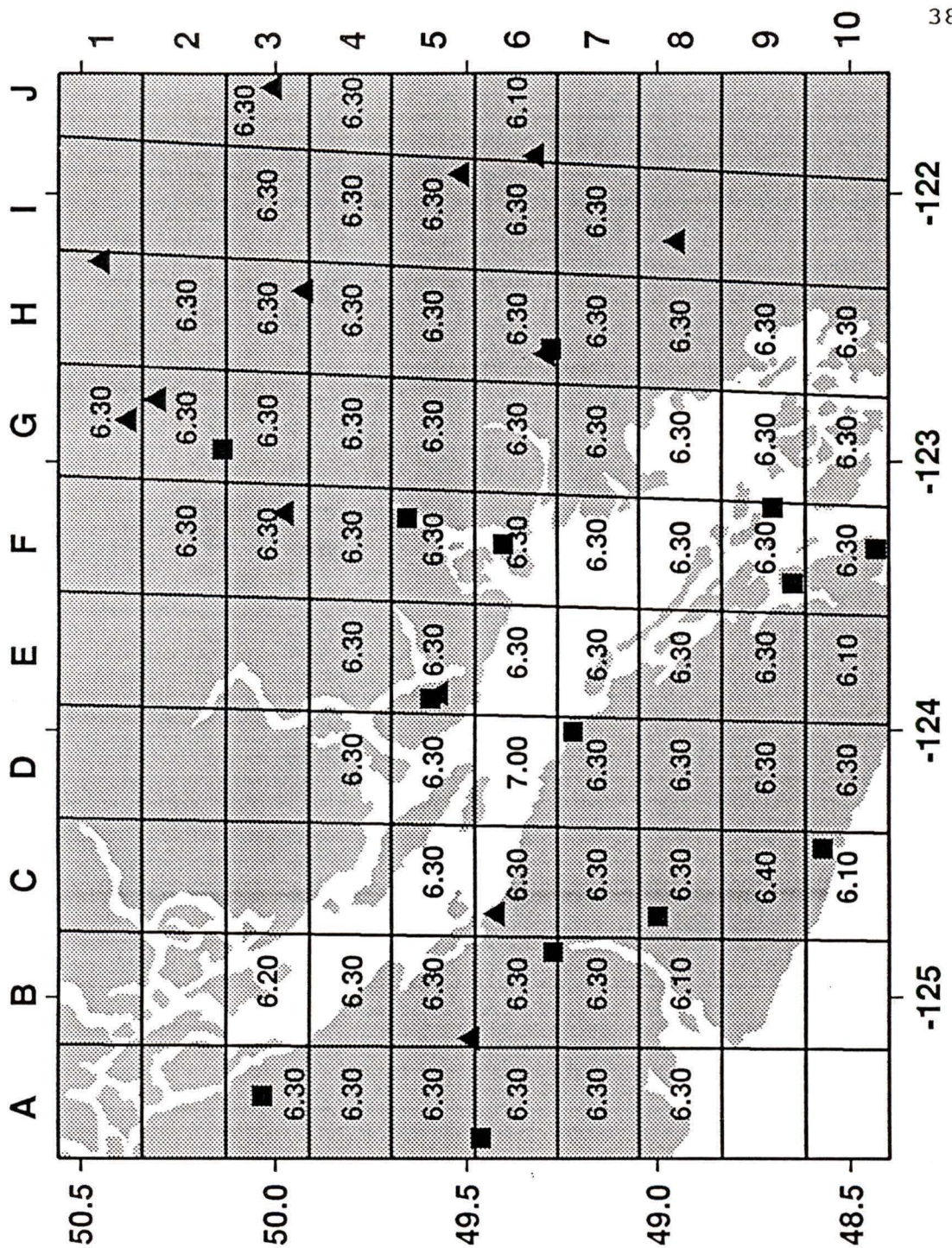


Figure 10: Modelling test P velocities with a single anomaly using a 10x10 grid. An artificial data set was used having one velocity anomaly of 7.0 km/s in element (D,6) set against a homogenous velocity background of 6.3 km/s. The starting model had velocities of 6.0 km/s in all the grid elements. The inversion reproduces the data set well although some elements around the edge of the grid are inaccurate to 0.2 km/s. Elements that have no ray coverage are left blank.

grid are well resolved. The r.m.s. of the residuals between velocities in the test model grid elements and the inverted elements being 0.01 km/s, this quantity shall be referred to at the velocity residual r.m.s. from now on. Table 5 shows the total distance travelled by all the rays in each of the cells. Some cells, very often at the edges of the grid, contain little ray path and those with less than 50 km do not model the test data set well. In order that the final model reproduce the test model grid elements, a larger damping factor was used on elements which had less than 50 km of ray path within them. Figure 11 shows the convergence of the

	A	B	C	D	E	F	G	H	I	J
1	0	0	0	0	0	0	10	71	0	0
2	0	0	0	0	0	3	271	116	0	0
3	41	17	0	0	0	222	406	137	140	15 6
4	30	40	33	14	146	414	393	444	159	25
5	28	122	130	280	542	373	329	306	218	0
6	74	264	478	298	352	395	436	480	272	2
7	47	106	154	239	186	161	235	275	46	0
8	40	5	86	88	152	190	242	193	107	0
9	0	0	63	64	120	276	175	33	0	0
10	0	0	18	19	3	122	34	0	0	0

Table 5: Distance travelled by the ray paths within each grid element on a 10x10 grid. The ray paths are those of the artificial data set used to produce the model shown in Figure 10.

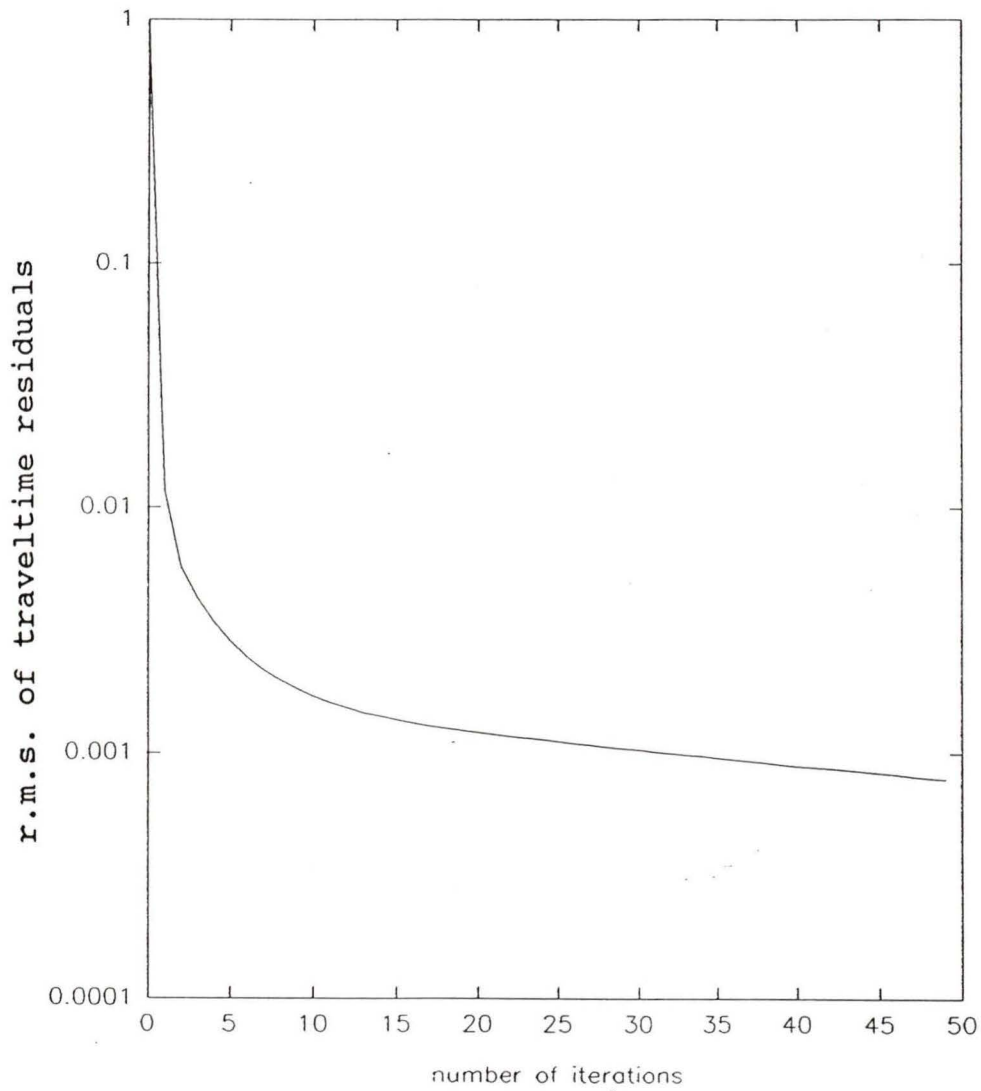


Figure 11: Converging r.m.s. of the travel time residuals with increasing number of iterations for the inversion program producing the results shown in Figure 10. Most convergence is achieved after 10-15 iterations.

travel time residuals, and indicates that most convergence is achieved after 10-15 iterations. After 50 iterations the r.m.s. of the travel time residuals was 0.0008 seconds. Subsequent tests used a 20x20 grid over the study region, with an artificial test model having a velocity anomaly in cell (J,10)⁵. Results are shown in Figure 12. The velocity residual r.m.s. was 1.62 km/s, a large increase from the 10x10 grid. Figure 12 also shows that the test model was not well reproduced, with excessively high and low velocities in some paired elements. Grid cells will be resolved best when they have a high ray path density. Since only 3 cells in the 20x20 grid have a total path distance of more than 100 km (Table 6), this test suggests that a value of at least 100 km is required for a reliable determination of cell velocity.

The program was found to work well with the simple assumption of a single velocity layer over a headwave refracting surface using a 10x10 grid. However, the real earth is much more complex and the problem of variation in the near surface layer should be addressed.

Artificial travel times were produced with several anomalies in the near surface layer; the refracting surface velocities were left as in the 10x10 grid test. Using a starting model with a near surface layer of 4.2 km/s and a homogenous 6.0 km/s velocity grid the results from the

⁵The element J,10 was chosen as the site of the anomalous velocity due to its typical ray coverage for the 20x20 grid (Table 6).

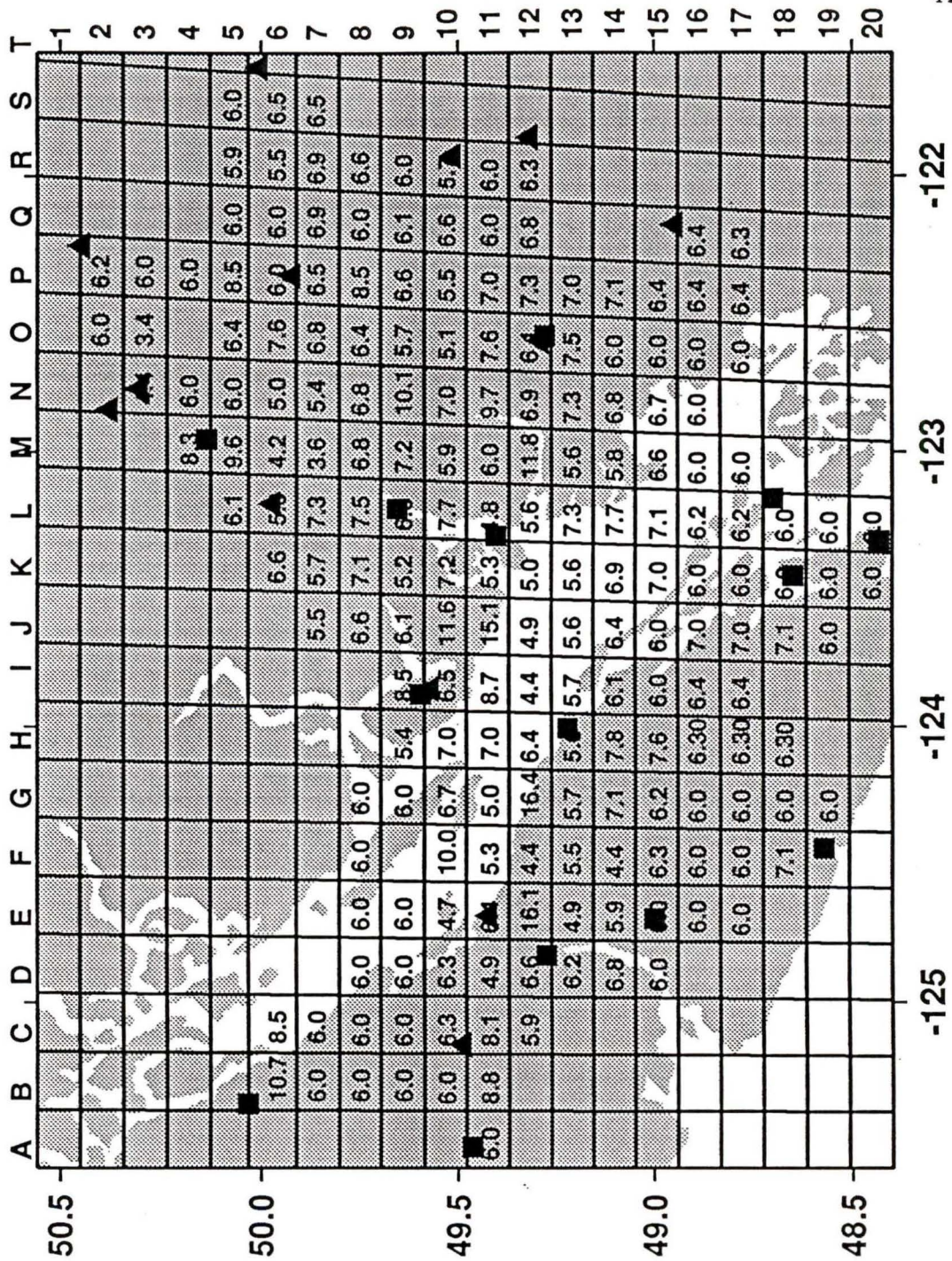


Figure 12: Modelling test P velocities with a single anomaly using a 20x20 grid. An artificial data set was used having one velocity anomaly of 7.0 km/s in element (J,10) set against a homogenous velocity background of 6.3 km/s. The low ray density in many of the elements (see Table 6) has caused a pairing effect in many areas in which one element increases in velocity while a neighbouring element decreases (see text).

	A	B	C	D	E	F	G	H	I	J	K	L	M	N	O	P	Q	R	S	T
1																				
2															4	18				
3													41	30	14	12				
4												11	52	39		12				
5											3	34	66	76	32	42	30	30	12	
6		31	10								28	50	32	41	24	15	6	51	99	
7		18	9	16	12					21	75	59	23	33	96	109	62	37	25	
8		12	15		5	16	7		12	67	25	71	73	104	65	89	18	31		
9		12	1	13	1		10	37	71	67	32	66	72	62	84	31	42	12		
10		14	36	58	60	50	79	77	63	76	39	74	74	76	94	39	80	32		
11	14	31	76	47	47	45	16	24	38	31	48	96	59	62	74	65	59	39		
12			22	38	116	74	59	44	44	49	39	58	64	126	84	70	53	38		
13				27	23	50	35	27	47	28	36	45	42	56	44	32				
14				22	22	21	57	52	18	27	28	20	46	49	48	13				
15				5	19	26	23	38	19	10	24	53	53	49	15	26				
16					13	12	13	14	40	26	20	49	70	20	19	26	15			
17					10	15	13	8	34	35	5	64	11		2	20	36			
18						33	18	10		20	27	15								
19						3	4			3	13	12								
20											9	6								

Table 6: Distance travelled by the ray paths within each grid element on a 20x20 grid. The ray paths are those of the artificial data set used to produce the model shown in Figure 12.

inversion are shown in Figure 13 for the refracting layer, and Table 7 for velocities in the top 1.5 km. The velocity grid results reproduce the test model well with a velocity residual r.m.s. of 0.04 km/s. In the inverted near surface layer three of the anomalies are resolved to within 0.2 km/s, while there is a larger discrepancy of 0.6 km/s at the PGC site.

The work of Zelt et al. (1993) suggests that there is a lateral velocity variation in the upper crust. Across the 300 km horizontal axis, artificial travel times were produced for a test model with two velocity boundaries. The model contained velocities of 6.6 km/s between 0 and 100 km, 6.3 km/s over the second third and 6.0 km/s from 200 to 300 km. Figure 14 shows that the test model was reproduced by the program. As would be expected of the real earth data, the velocity boundaries in the test data do not coincide with the cell boundaries on the 10x10 grid used in its modelling. Cells which contain the boundaries in the 10x10 grid average out the velocities across the boundary. For example the 100 km velocity boundary passes through cells (D,5) to (D,10) of the 10x10 grid with one third of each cell over the 6.6 km/s velocity region and the remainder over a 6.3 km/s velocity region. The 'average' value of all the cells, except (D,8), is 6.4 km/s.

The tests on the artificial data would suggest that there are some characteristics of the 10x10 grid which should be considered in interpreting results gained using it. Grid cells with less than 50 km of ray path are damped more than the

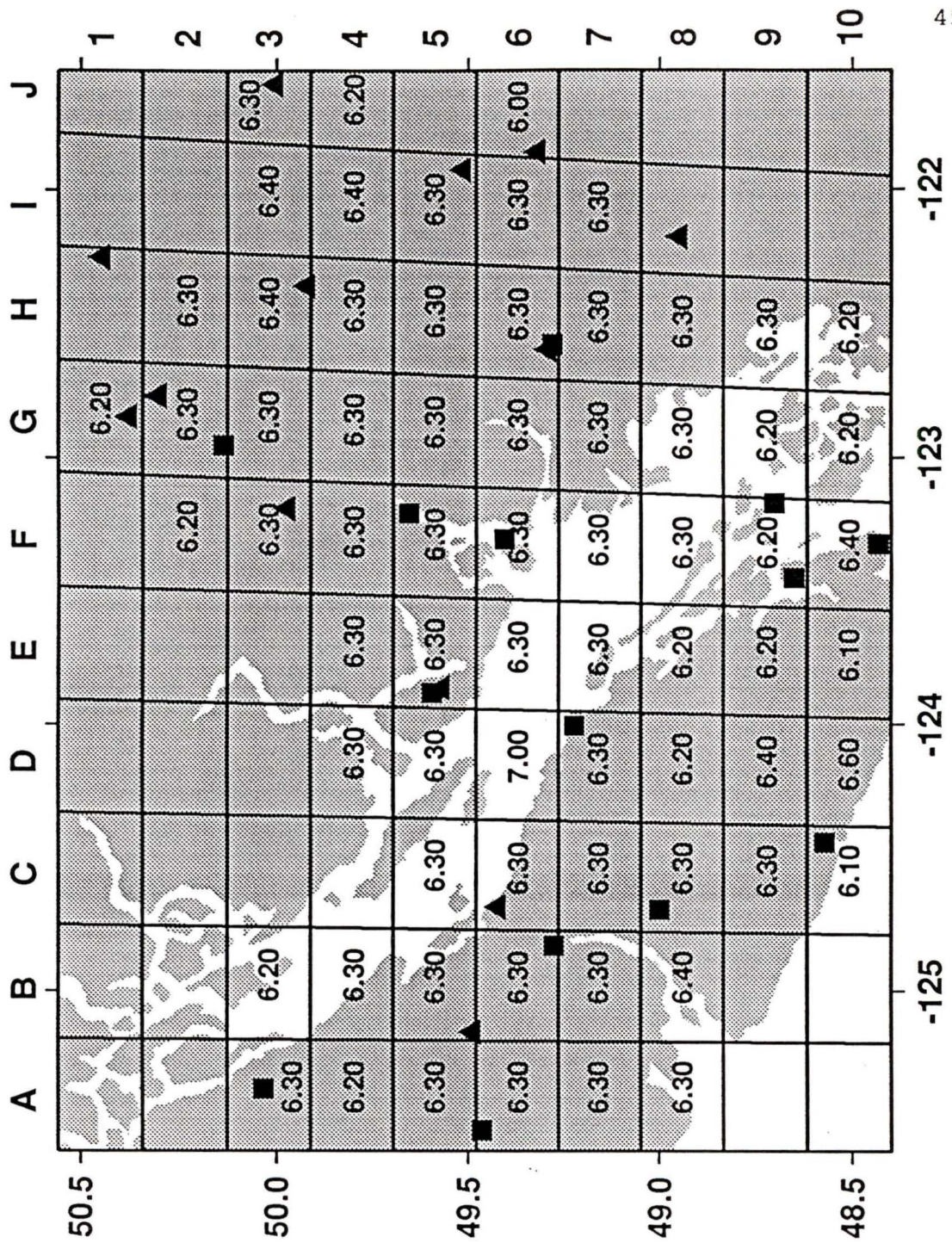


Figure 13: Modelling test P velocities with near surface anomalies using a 10x10 grid. The artificial data set used had several anomalies in the upper 1.5 km layer (see Table 7) and the refracting grid had a velocity anomaly of 7.0 km/s in element (D,6) set against a background of 6.3 km/s.

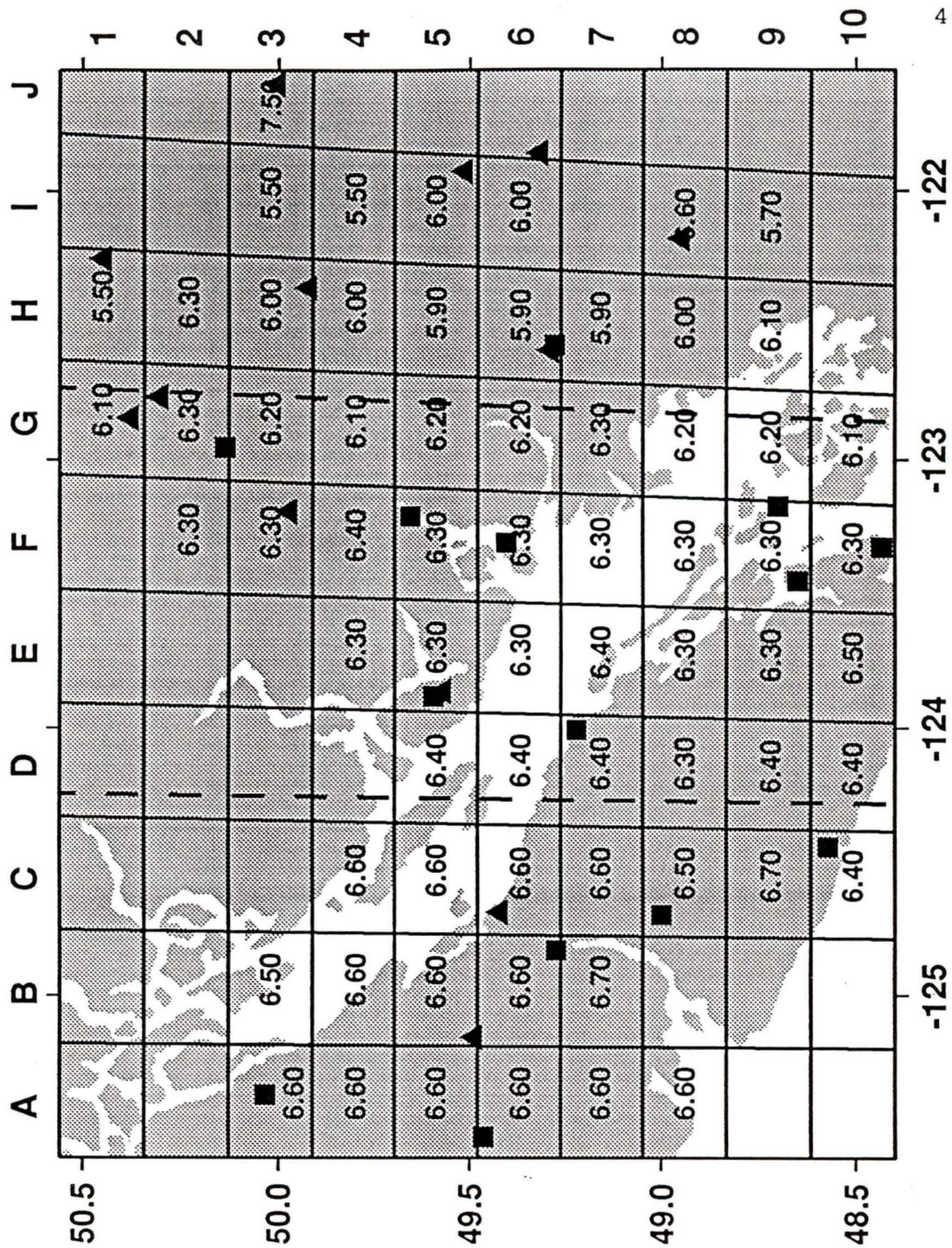


Figure 14: Modelling P velocity zone test data using a 10x10 grid. The test velocity model was divided into three velocity zones of 6.6 km/s, 6.3 km/s, and 6.0 km/s with boundaries at 100 km and 200 km, as marked by the dashed lines. Elements which contain boundaries essentially average over them producing values between those of the corresponding velocity zones.

	Artificial data km/s	Inversion result km/s
ALB	4.2	4.0
BIB	4.2	4.0
BTB	4.2	4.2
CBB	4.2	4.2
HNB	5.2 (fast)	5.2
MGB	4.2	4.0
NAB	4.2	4.0
PFB	4.2	4.2
PGC	3.2 (slow)	3.8
SHB	4.2	4.0
SNB	4.2	4.5
VGZ	4.2	4.2
WHB	5.2 (fast)	5.0
WPB	4.2	4.0
4	4.2	4.5
6	4.2	4.2
7	4.2	4.2
8	3.2 (slow)	3.4
9	4.2	4.4
10	4.2	4.4
11	4.2	4.4
12	4.2	4.2
21	4.2	4.3
23	4.2	4.2
46	4.2	4.2
47	4.2	4.5
48	4.2	4.3
91-1	4.2	4.2

Table 7: Comparison of surface layer test model and its modelling using the inversion program. The test model had a velocity highs at WHB and HNB, and lows at PGC and shot 8.

remaining cells. However these cells still often give unreasonable answers. A pairing effect is sometimes observed between two cells in which one takes an extremely high value while the other takes a correspondingly low value. This may be undetectable to the program as the travel time between the two cells could remain unchanged if the average velocity of the two cells were the same as the average of the true velocities.

CHAPTER FOUR - RESULTS

4.1 INITIAL IN-LINE REFRACTION INTERPRETATION

Before using the tomographic method described in the previous chapter an in-line refraction method was pursued. Seismograms from combinations of shots and receivers were isolated from the main data set to leave only those which sample along a two dimensional profile. As the shot locations were originally positioned for in line refraction experiments, stations falling on or close to the refraction line were chosen to obtain the shot-station combinations used in the data subsets. While drastically reducing the utilizable number of traces and yielding a data density far less than the SCoRE profiles, a simple graphing method can be used to estimate the upper crustal velocity for both P and S waves, and hence an estimate of Poisson's ratio can be made in this region. The previous refraction surveys of SCoRE and VISP80 offered the chance to compare their P wave estimates with those obtained using this method. In addition, the distribution of shots and receivers enabled a region different from the SCoRE lines to be sampled.

Five subsets of data were selected corresponding to five in-line profiles. All but one set corresponded to a previous refraction line. The data subset, called Set80, was composed using travel times and distance offsets between the shotpoints 8 and 9, and the several WCTN stations located over the south of Vancouver Island. Figure 15(a) shows the P wave ray paths

of Set80. These rays traversed roughly the same upper crust as those of VISP80 Line IV (Spence et al. 1985). The seismograms for these paths are shown in Figure 15(b). Similarly, the paths for S waves are shown in Figure 16(a) and seismograms in Figure 16(b). Travel times were plotted against the distance between the source and receiver, using a reducing velocity of 7 km/s for P arrivals and 4 km/s for S wave arrivals. A least squares fit to the arrivals provided apparent velocities.

Set2 covers the same profile as Line 2 of SCoRE89 (Mclean 1994). Figures 17 and 18 show the P and S wave data, respectively. Line 3 of SCoRE89 (Zelt et al. 1993) was duplicated by Set3. The P wave data is shown in Figure 19 and the S wave data in Figure 20. Set10 covers the region of SCoRE Line 10 (O'Leary et al. 1994). The travel paths and seismograms are shown in Figures 21 and 22, respectively for the P waves and S waves. An additional line was constructed using data from six shots and four stations along a path extending northeast from the southern Gulf Islands, termed setnew, the P wave ray paths are shown in Figure 23(a) and the S wave ray paths in Figure 24(a), and the seismograms are shown in Figures 23(b) and 24(b), respectively.

The P velocities, S velocities and Poisson's ratios are shown in Table 8 for the five data sets, along with the upper crustal P wave velocity estimates of the SCoRE and VISP80 surveys.

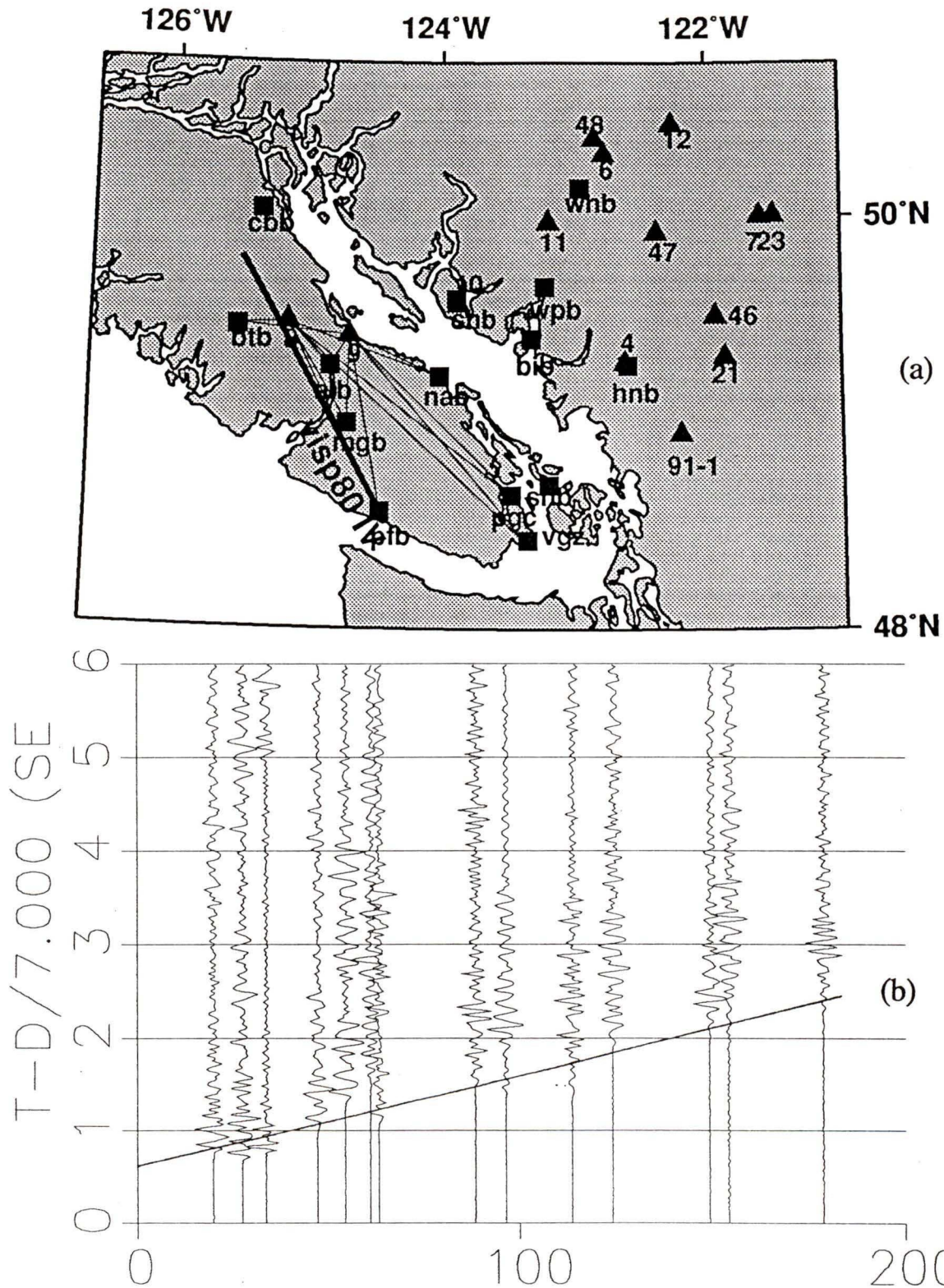


Figure 15: (a) P wave travel paths (thin black lines) in the region of the VISP80 IV refraction profile (bold black line). (b) The P wave arrivals of set80 corresponding to the paths shown in (a). The arrivals were plotted against offset distance using a reducing velocity of 7.0 km/s. The estimated P wave velocity in the region was 6.53 km/s.

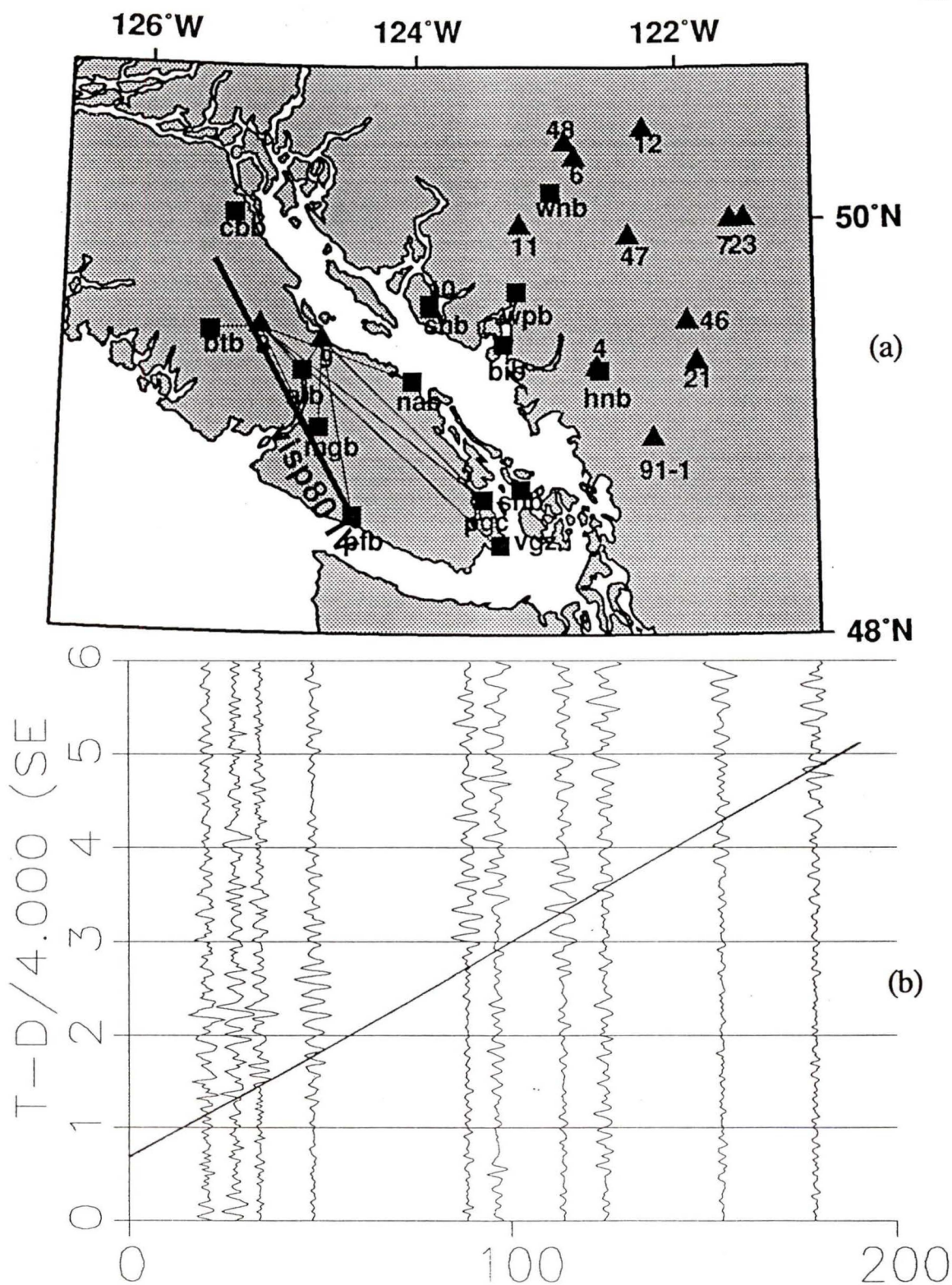


Figure 16: (a) S wave travel paths (thin black lines) in the region of the VISP80 IV refraction profile (bold black line). (b) The S wave arrivals of set80 corresponding to the paths shown in (a). The arrivals were plotted against offset distance using a reducing velocity of 4.0 Km/s. The estimated S wave velocity in this region was 3.65 km/s.

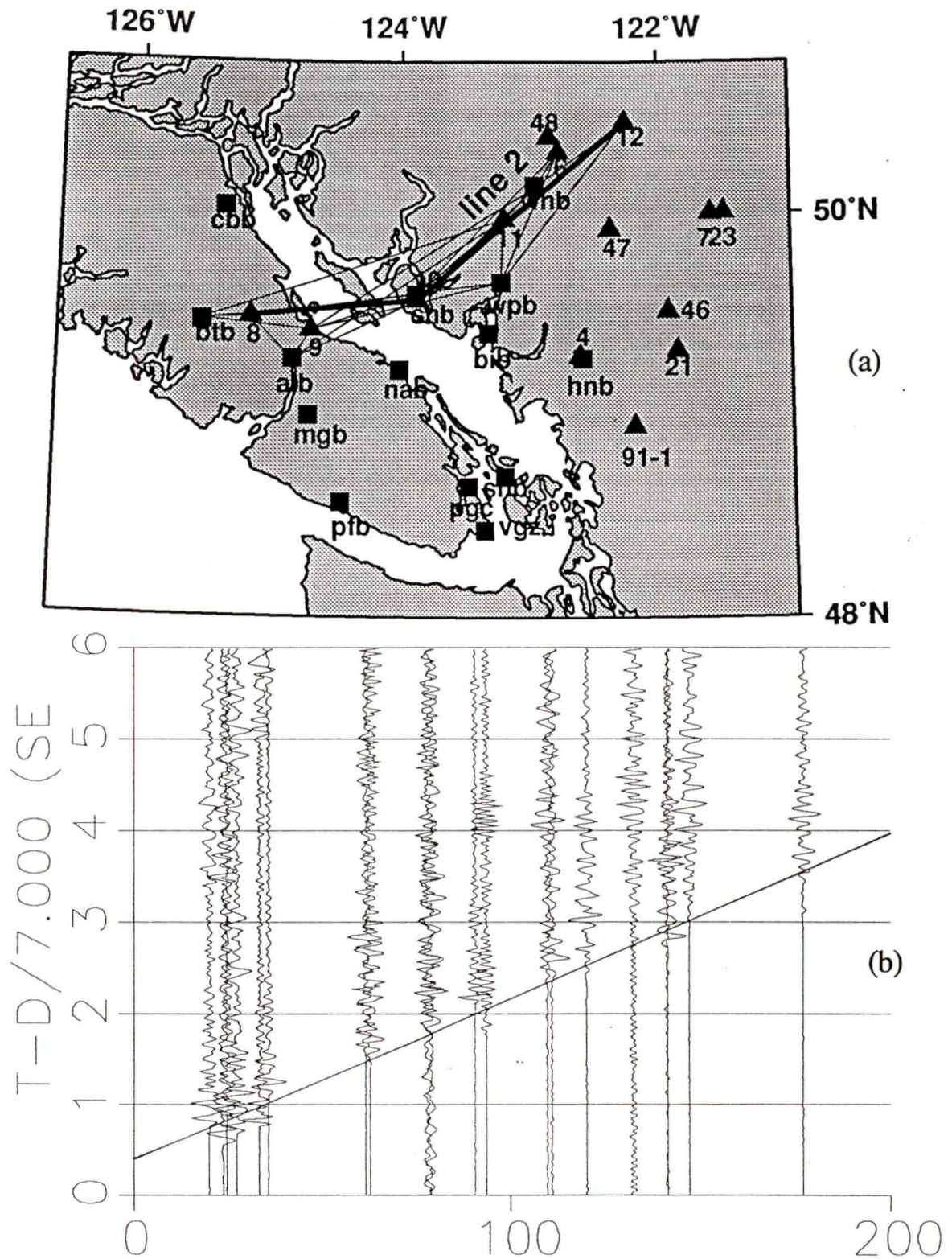


Figure 17: (a) P wave travel paths (thin black lines) in the region of the Line 2 refraction profile (bold black line). (b) The P wave arrivals of set2 corresponding to the paths shown in (a). The arrivals were plotted against offset distance using a reducing velocity of 7.0 km/s. The estimated P wave velocity in the region was 6.2 km/s.

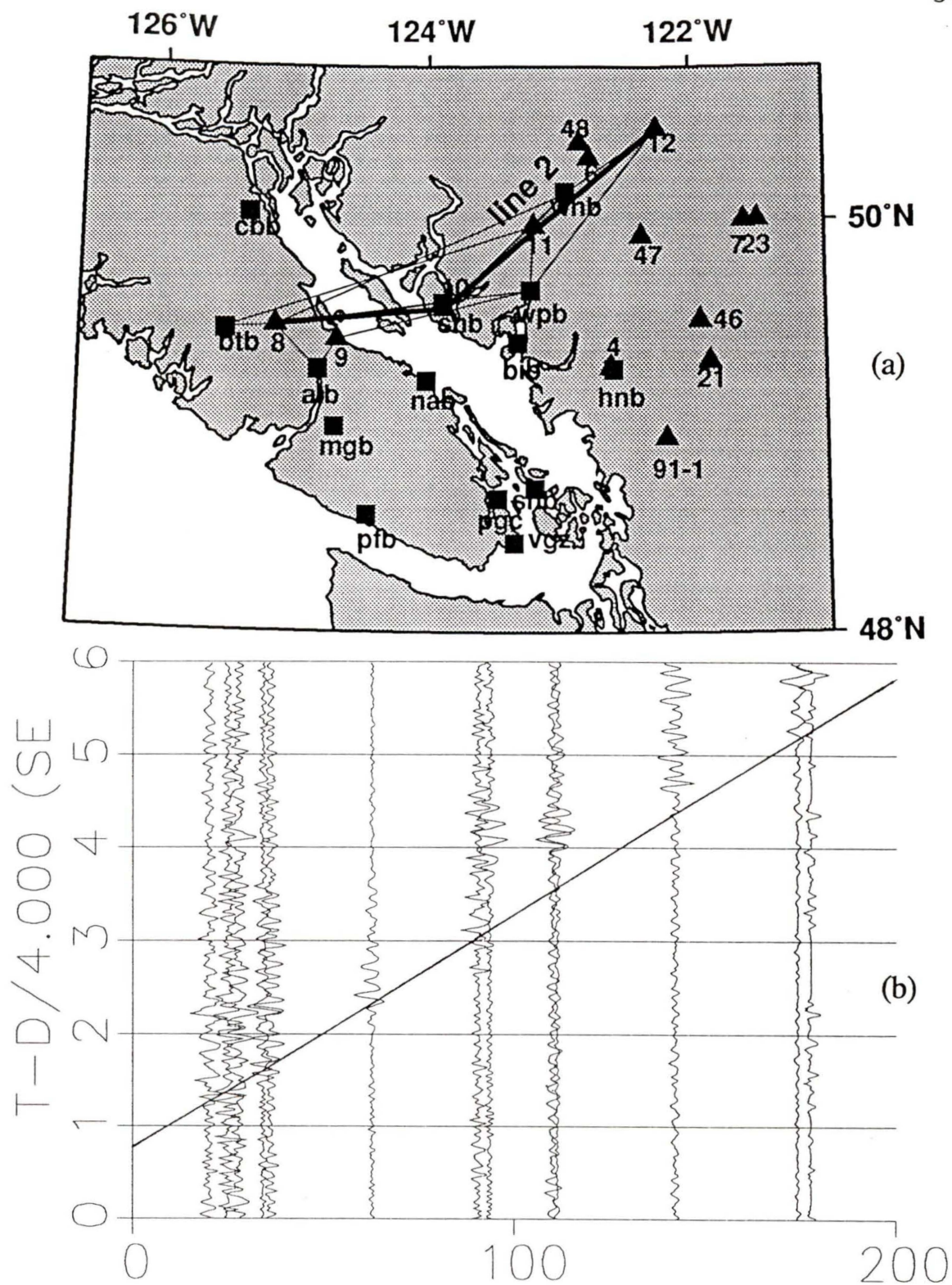


Figure 18: (a) S wave travel paths (thin black lines) in the region of the Line 2 refraction profile (bold black line). (b) The S wave arrivals of set2 corresponding to the paths shown in (a). The arrivals were plotted against offset distance using a reducing velocity of 4.0 km/s. The estimated S wave velocity in the region was 3.62 km/s.

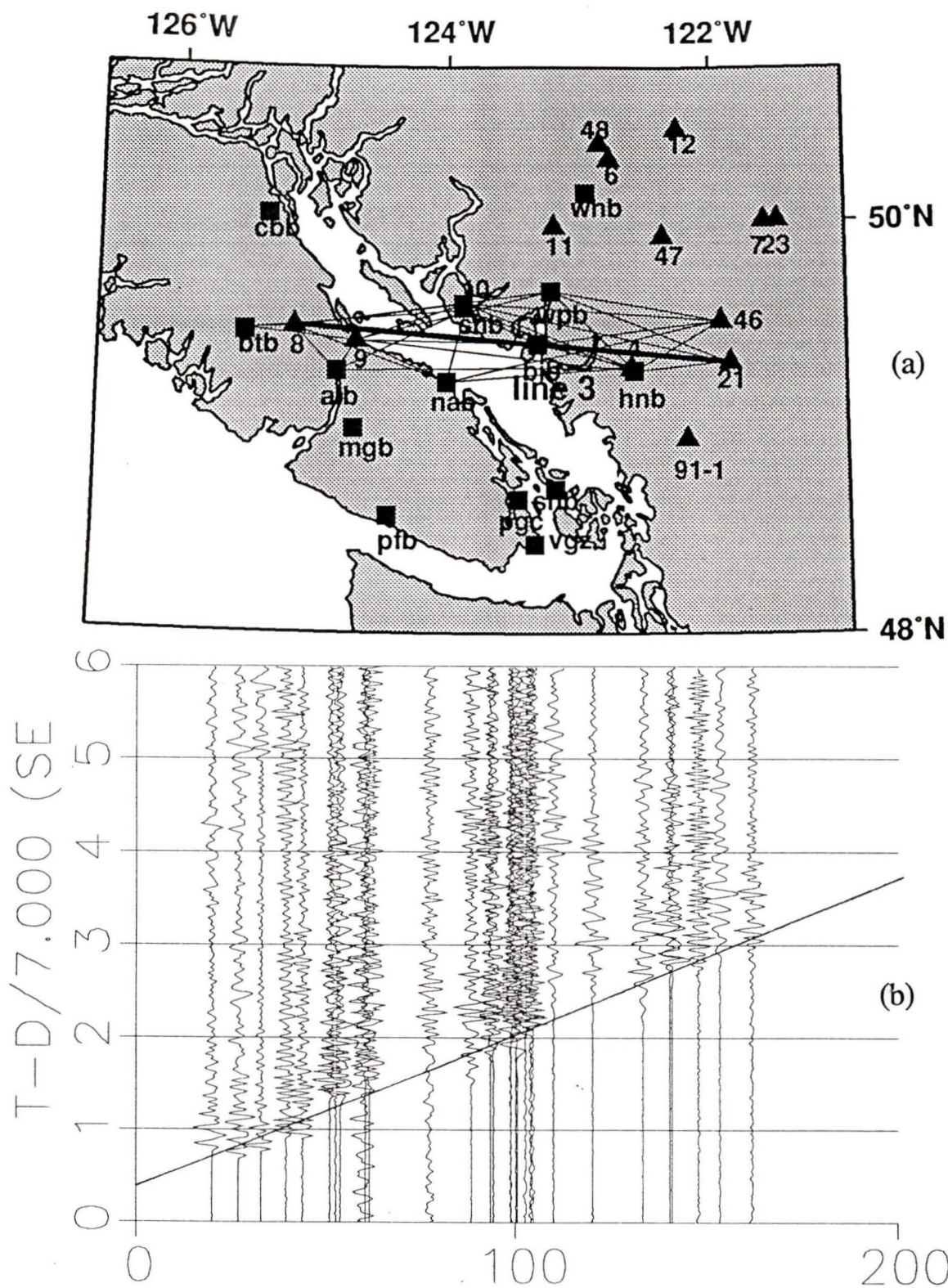


Figure 19: (a) P wave travel paths (thin black lines) in the region of the Line 3 refraction profile (bold black line). (b) The P wave arrivals of set3 corresponding to the paths shown in (a). The arrivals were plotted against offset distance using a reducing velocity of 7.0 km/s. The estimated P wave velocity in the region was 6.31 km/s.

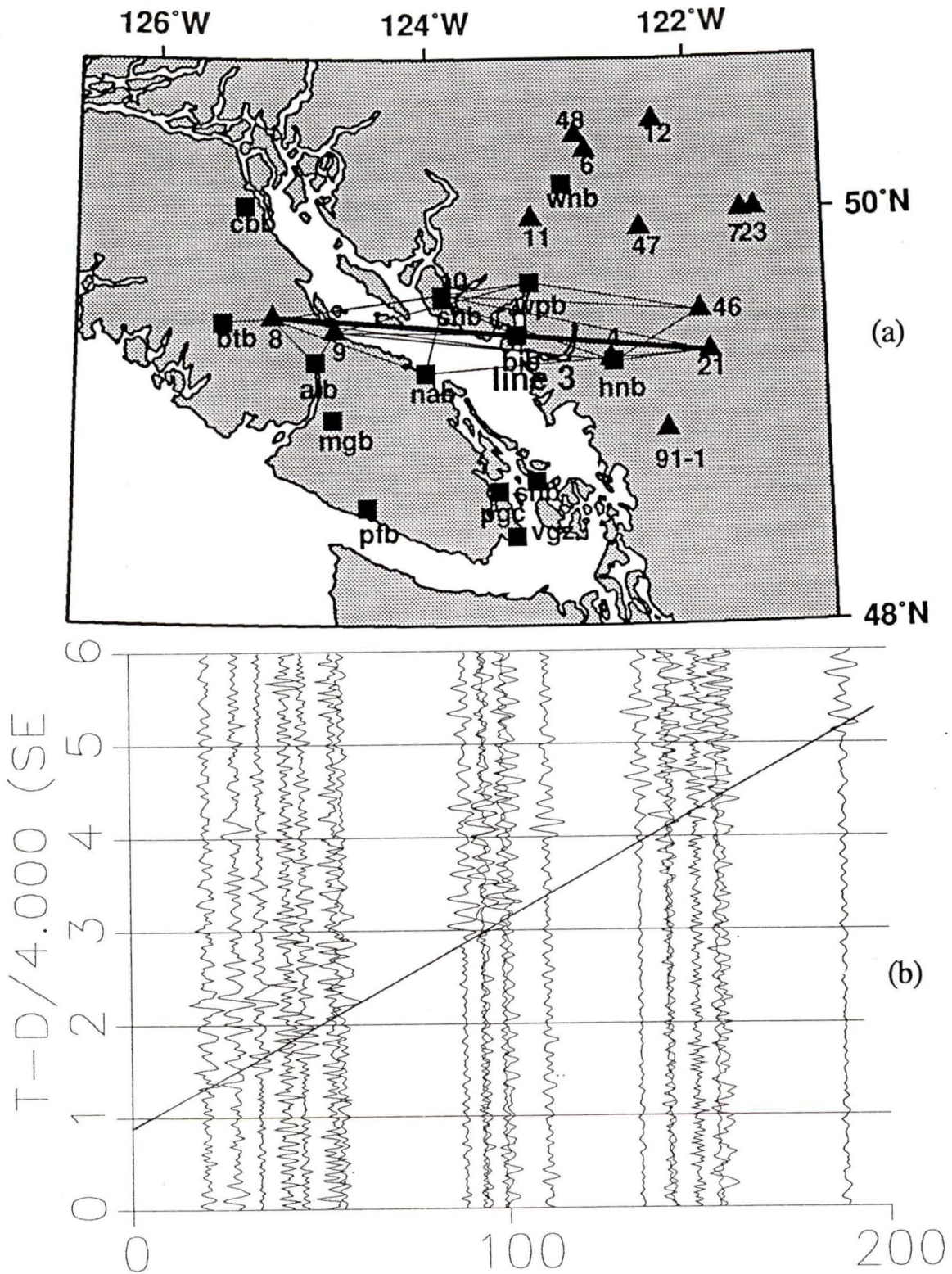


Figure 20: (a) S wave travel paths (thin black lines) in the region of the Line 3 refraction profile (bold black line). (b) The S wave arrivals of set3 corresponding to the paths shown in (a). The arrivals were plotted against offset distance using a reducing velocity of 4.0 km/s. The estimated S wave velocity in the region was 3.64 km/s.

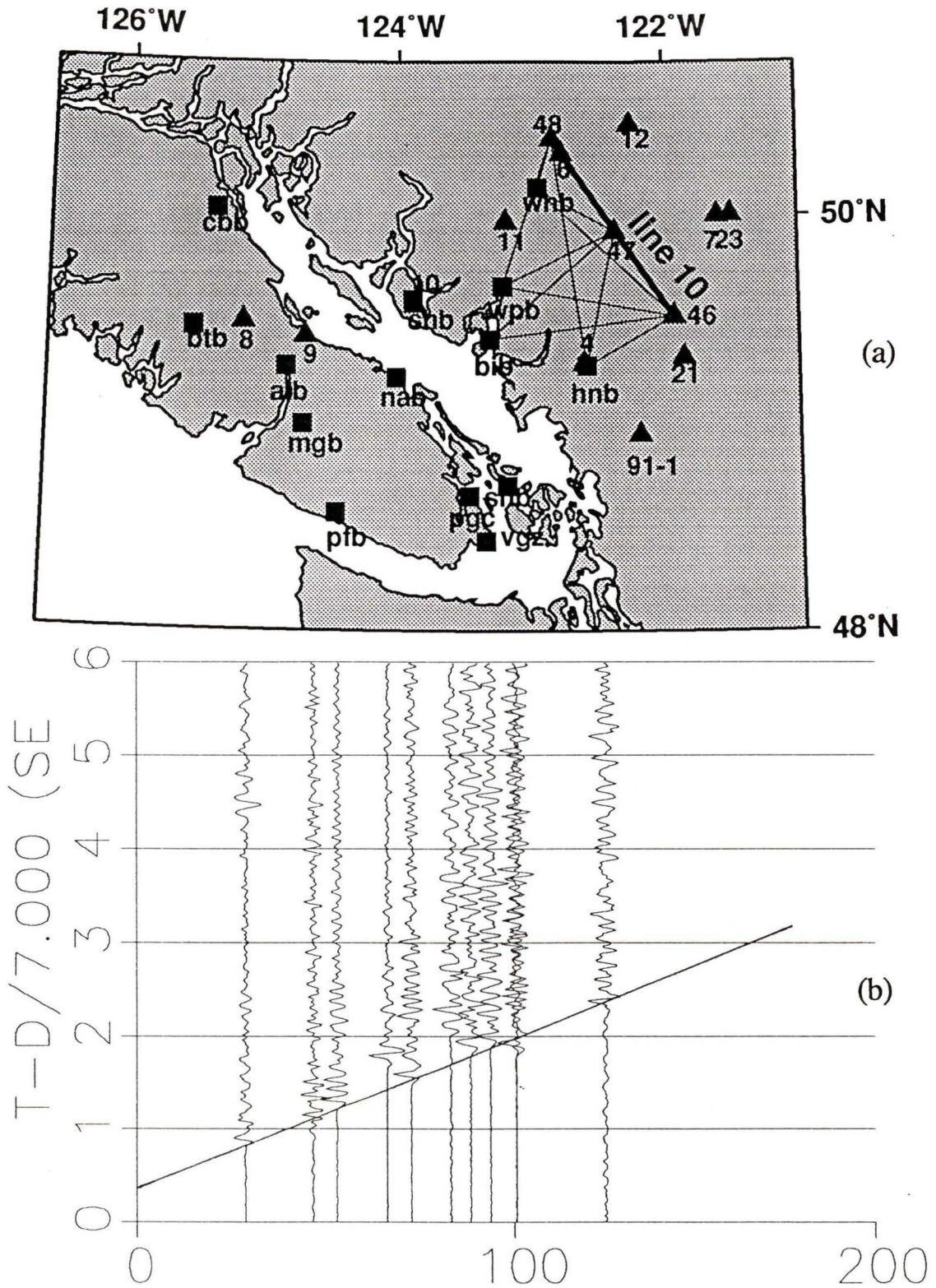


Figure 21: (a) P wave travel paths (thin black lines) in the region of the Line 10 refraction profile (bold black line). (b) The P wave arrivals of set 10 corresponding to the paths shown in (a). The arrivals were plotted against offset distance using a reducing velocity of 7.0 km/s. The estimated P wave velocity in the region was 6.31 km/s.

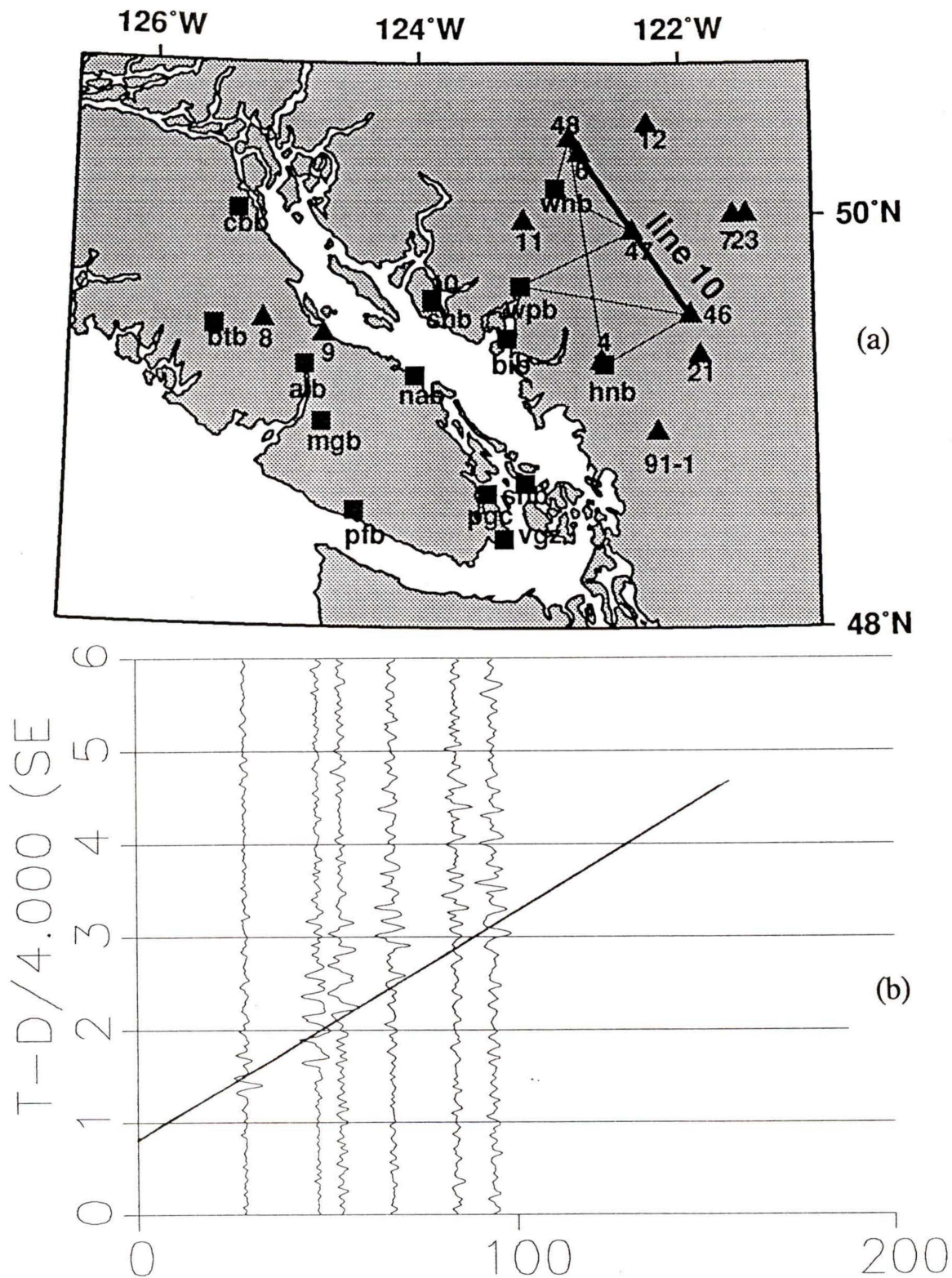


Figure 22: (a) S wave travel paths (thin black lines) in the region of the Line 10 refraction profile (bold black line). (b) The S wave arrivals of set10 corresponding to the paths shown in (a). The arrivals were plotted against offset distance using a reducing velocity of 4.0 km/s. The estimated S wave velocity in the region was 3.62 km/s.

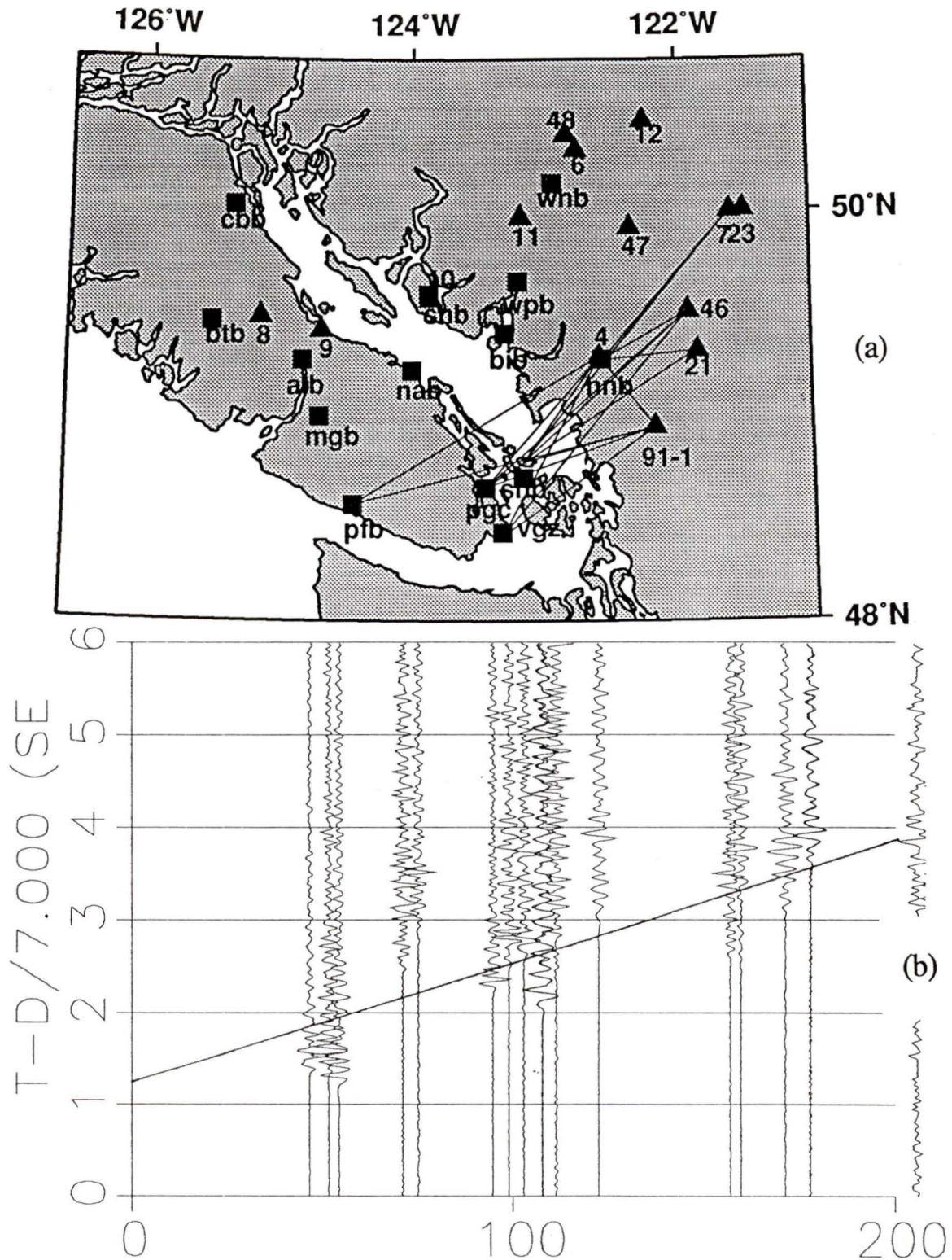


Figure 23: (a) P wave travel paths (thin black lines) used to construct the data set. (b) The P wave arrivals of setnew corresponding to the paths shown in (a). The arrivals were plotted against offset distance using a reducing velocity of 7.0 km/s. The estimated P wave velocity in the region was 6.46 km/s.

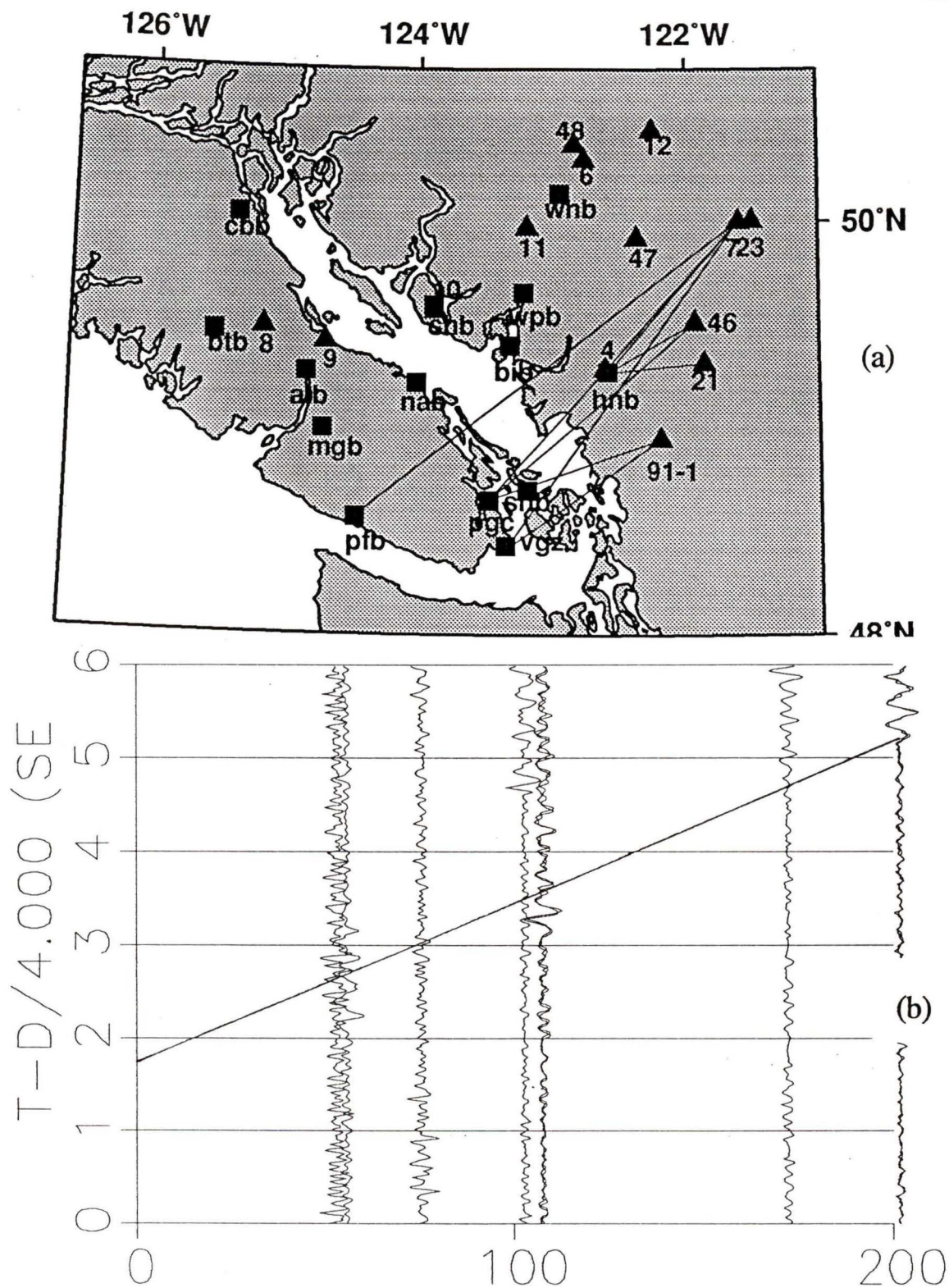


Figure 24: (a) S wave travel paths (thin black lines) used to construct the data set. (b) The S wave arrivals of setnew corresponding to the paths shown in (a). The arrivals were plotted against offset distance using a reducing velocity of 4.0 km/s. The estimated S wave velocity in the region was 3.73 km/s.

Set80 suggests a high upper crustal velocity of 6.53 km/s in southern Vancouver Island. The along strike and cross strike sets in the Coast Belt (Sets 10, 2 and 3) give lower velocities of 6.31, 6.20 and 6.31 km/s, respectively. The cross strike line in the southern Coast Belt (Setnew) has a slightly higher velocity of 6.46 km/s. All results are in good agreement with the former surveys with at most velocity differences of 0.5 km/s. S wave velocities are ~3.6 km/s along all the lines, with the exception of Setnew which produces a slightly higher velocity. Poisson's ratio has somewhat higher values over the southern Vancouver Island at 0.27, compared to the Coast Belt where the value is 0.25.

	P vel. km/s	P vel. of survey km/s	S vel. km/s	Poisson's ratio
Set80	6.53	6.5	3.65	0.27
Set2	6.20	6.25	3.62	0.24
Set3	6.31	6.3	3.64	0.25
Set10	6.31	6.3	3.62	0.25
Set new	6.46	-	3.73	0.25

Table 8: P and S wave velocity estimates for the upper crust from approximately in-line data sets. The P wave velocities in the upper crust from the SCoRE and VISP refraction surveys are shown for comparison. The last column shows estimates of Poisson's ratio along the lines calculated from the P and S wave estimates. P waves have the highest velocities over southern Vancouver Island, while S waves within the study region are highest over the southern most Coast Belt and Georgia Strait. Poisson's ratio is homogenous except for an increase in the south of the island.

4.2 P WAVE INVERSION

The tomographic method described in Section 3.4 required the specification of both the grid orientation and the grid dimensions. A number of along strike grids having dimensions varying from 6x5 to 11x10 were used to model the observational data set. The final model was computed using an 8x7 grid (Figure 25) for which fast-slow pairing was limited to the edge elements of the grid. The dimensions of each grid element were 42 km by 34 km. Despite the reduction in the number of cells from the grids used to test the artificial data sets, Vancouver Island, Georgia Strait, and the mainland are separately distinguishable within the grid structure.

Velocities in the grid elements over southern Vancouver Island range from 6.30-6.70 km/s; while to the east, Georgia Strait has velocities from 6.05-6.35 km/s. The Northern Coast Belt velocities range from 6.15-6.25 km/s and increase slightly to the south with velocities as high as 6.55 km/s.

There are several elements which have unexpected velocities for the upper crust. As in the modelling of artificial data sets it is useful to examine the ray path densities within the elements as an indication of reliability. Table 9 shows the length of ray path within each cell for the grid shown in Figure 25.

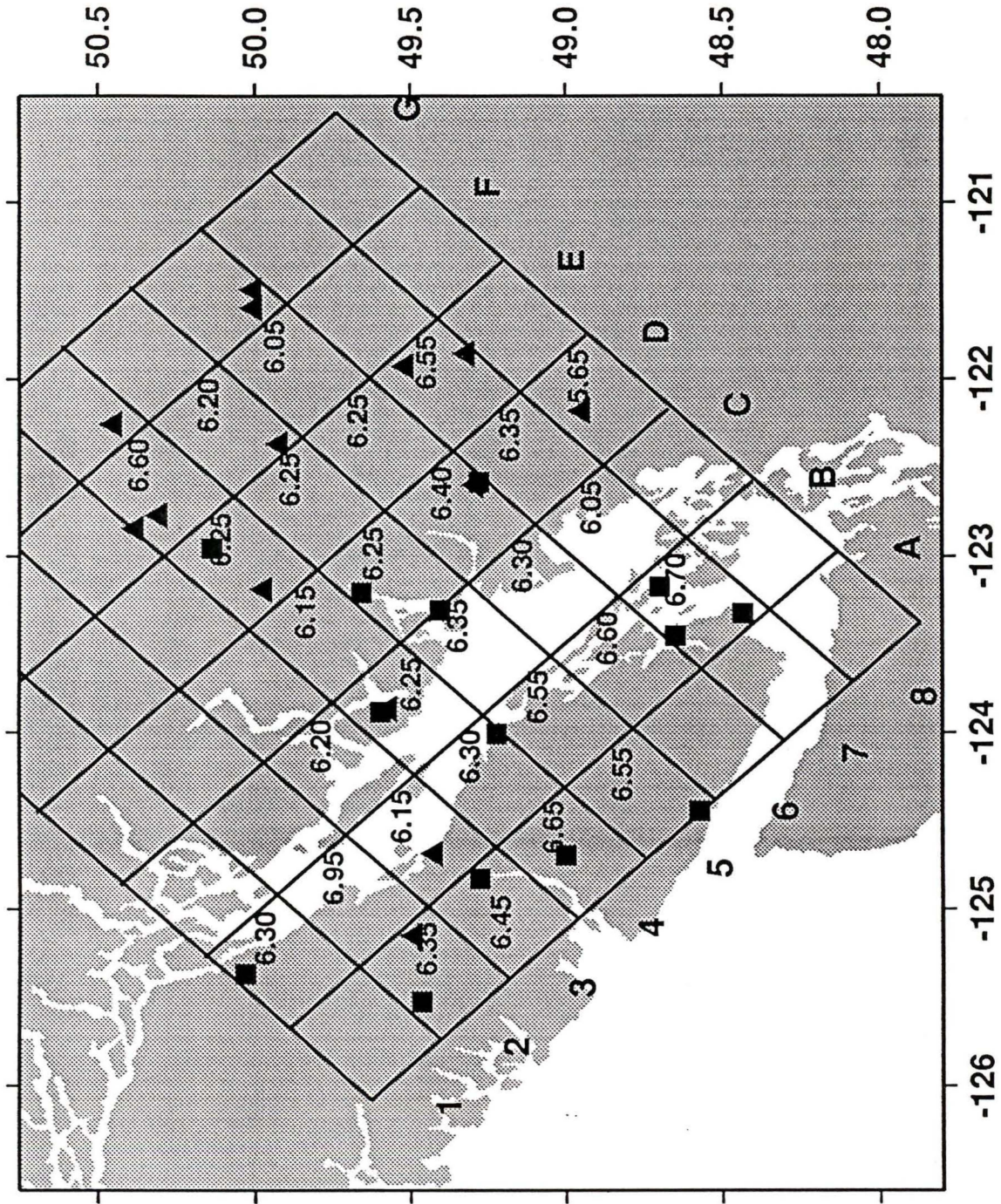


Figure 25: The final P wave inversion velocity model using the observed P wave data set with a 8x7 along strike grid after 50 iterations. The starting model had velocities of 6.3 km/s in all the grid elements and a near surface velocity of 4.2 km/s. Velocities on Vancouver Island are generally higher than in the Georgia Strait or the mainland (see text for further discussion). The offset cutoff on the original data set used here is 175 km which resulted in a 116 trace P wave data set.

	A	B	C	D	E	F	G
1	0	92	0	0	0	0	0
2	187	99	19	0	0	0	0
3	184	594	127	0	0	0	0
4	182	538	866	652	664	281	13
5	144	318	562	891	751	137	0
6	51	355	362	950	548	421	27
7	0	391	471	441	403	0	0
8	0	7	51	146	0	0	0

Table 9: Distance travelled by the ray paths within each grid element on a 8x7 along strike grid. The ray paths are those of the P wave observational data set, used to produce the model shown in Figure 25.

The first anomaly to consider is in element (B,2). This element and its neighbour to the north both contain less than 100 km of ray path, and although this produced sound results with test data sets this may not be so for the noisier observational data set. From Figure 7 it can be seen that only three ray paths sample this region and that they travel through both cells (B,2) and (B,1); this is therefore a likely site for the pairing effect to occur, with cell (B,2) increasing at the expense of its neighbour. Element (F,4) has a value of 6.60 km/s which is significantly higher than the surrounding areas of the Coast Belt. Although the cell contains 281 km of ray path (Table 9), it is at the edge of the model and is also adjoining a square with very low path density, element (G,4). It is therefore best to regard the

velocity in (F,4) with some suspicion. In the southern Coast Belt (D,8) has a much lower velocity than its surrounding elements. The ray path coverage here is relatively low (Table 9); however the low velocity may be the result of low near surface velocities below the shot point, see Section 4.6.

To conclude, upper crustal grid velocities over southern Vancouver Island are seen to be consistently higher than those in the Coast Belt, and Georgia Strait has the lowest velocities in the region.

4.3 ADDITIONAL INVERSIONS USING THE P WAVE DATA SET

4.3.1 ROTATION OF THE GRID

The velocity structure of the study region should obviously be left unchanged by how it is modelled. By rotating the grid so that its X and Y axis roughly correspond to the lines of longitude and latitude, a new inversion for velocity can be performed. Comparing the rotated results with those of the along strike grid enables an estimate to be made of which areas are reliably modelled and thus left unchanged by the movement of the grid.

The results of the 45° rotation are shown in Figure 26. It can be seen that the velocities over southern Vancouver Island are between 6.30-7.00 km/s, which compares well to the 6.30-6.70 km/s of the along strike grid (Figure 25). The grid elements do not outline Georgia Strait well; however east of Vancouver Island velocities in the grid elements that overlay

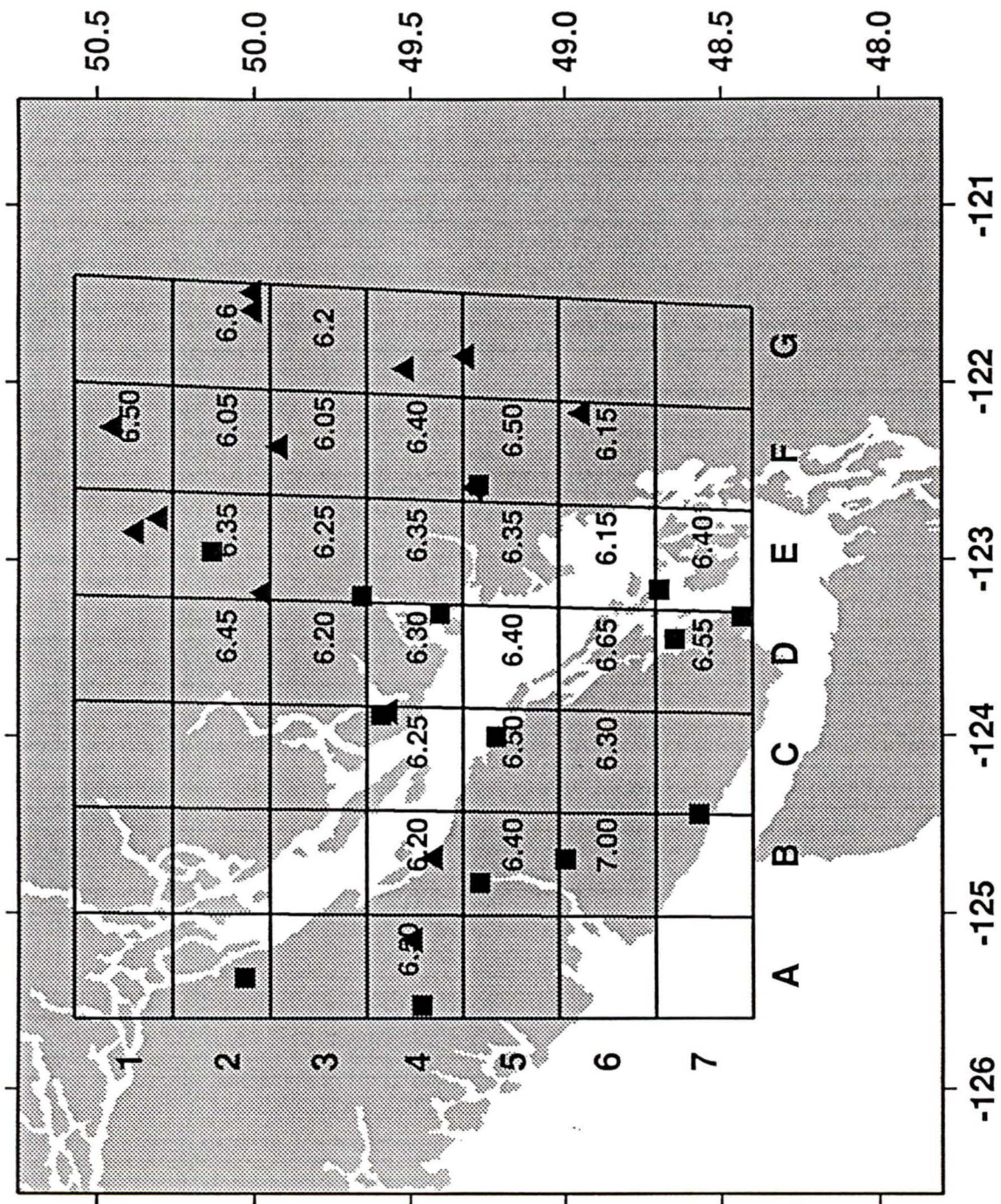


Figure 26: P wave velocities on a rotated 7x7 grid. The rotation does not disturb the main features of the model as seen in Figure 25 with the highest velocities located over Vancouver Island. The average velocity over the coast Belt is ~ 6.3 km/s.

the Georgia Strait decrease to between 6.15-6.40 km/s. Under the rotation the Coast Belt retains its character with velocities between 6.25 and 6.40 km/s. Grid element (F,7) overlies the region covered by the anomalous cell (D,8) in Figure 25. With the rotation of the grid (F,7) has increased to 6.15 km/s. The variability of this region under rotation suggest it should be treated with some suspicion.

4.3.2 DELETION OF HIGH OFFSETS

It is assumed that all observed travel times correspond to travel paths in the upper crust only. Rays travelling from higher offsets may have penetrated deeper and have sampled higher velocity crust. As a test to whether the high velocity areas of the model are caused by such rays the high offset cutoff was systematically lowered from 175 km. It should be noted that changes in the elements cannot be solely attributed to the deletion of high velocity travel paths as the traces removed will also effect the ray density within each of the cells. This may lead to some elements becoming unstable.

The final model, Figure 25, was produced using 116 observed travel times, of which no shot-station offset was greater than 175 km, i.e the offset cutoff applied to the data. The offset cutoff was lowered to 161 km leaving 109 travel times; the resulting model from these travel times is shown in Figure 27. The reduced number of travel paths leaves the model unaltered except for three elements which differ

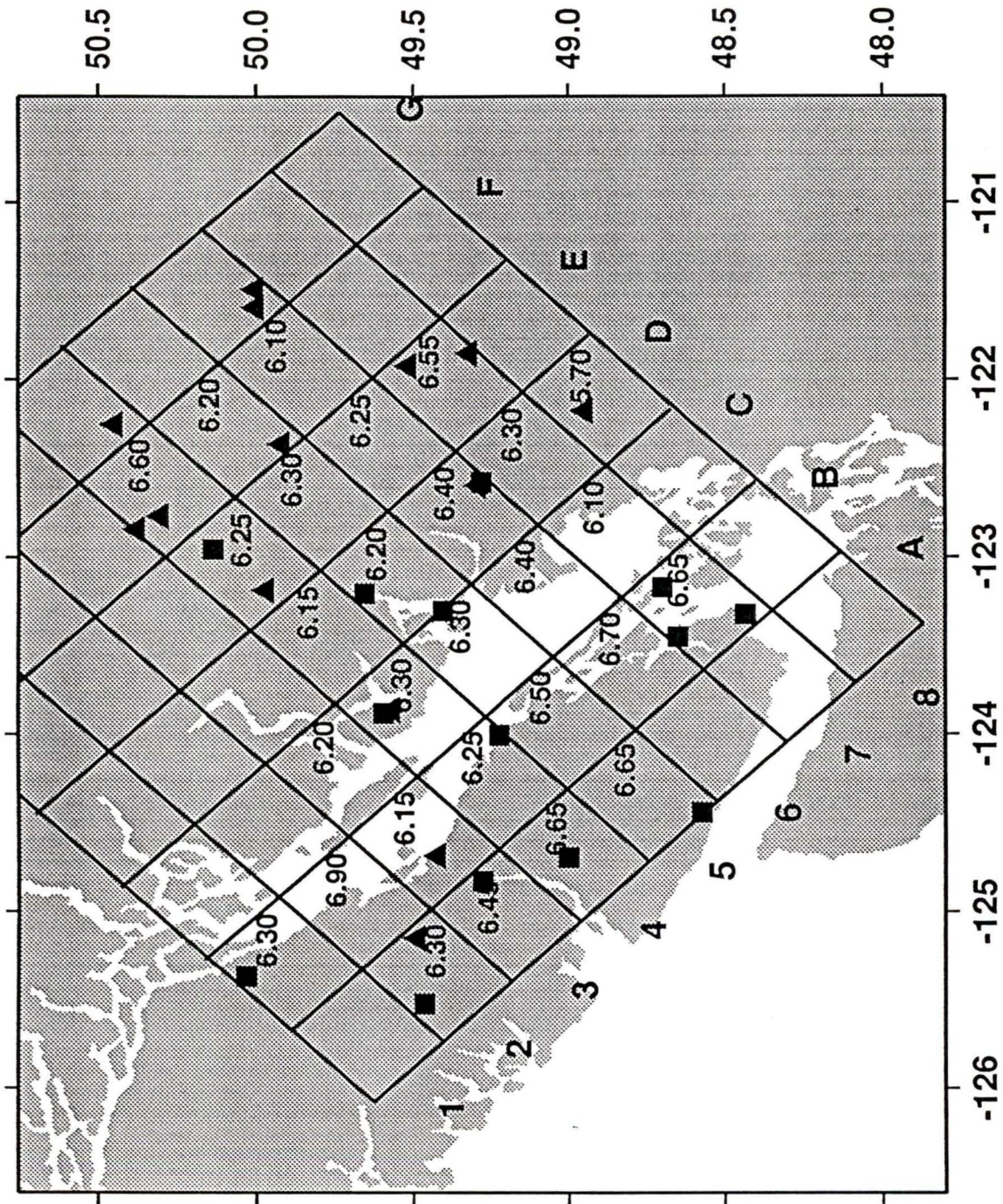


Figure 27: P wave velocities on a 8x7 along strike grid with a 161 km offset cutoff imposed on the data set, resulting in a 109 trace data set. The deletion of high offset travel paths does not result in a coherent reduction of grid velocities. This suggests that high offset rays did not sample lower crustal and therefore higher velocity regions.

from the original by 0.1 km/s. There is no pattern in the resulting changes.

Reducing the offset cutoff to 147 km, and so 95 travel times, produces the model shown in Figure 28. Cells (B,6) and (B,5) on Vancouver Island are low and high, with the pairing effect seemingly evident. This figure shows the lower limit of required travel times for reliable models has been crossed. Unfortunately the breakdown of the model with reduced data input does not allow for complete elimination of the possibility that lower crustal paths are contaminating the data set. However the results from Figure 28 show only a slight decrease in velocities and no change over many cells, a good indication that most lower crustal paths have been removed by the original 175 km offset cutoff.

4.4 S WAVE INVERSION

The S wave velocity model over the study area was produced using an along strike 8x7 grid. The dimensions of the grid were the same as those used for the P wave model in Figure 25.

The final S wave model is shown in Figure 29 and the ray path lengths within each cell in Table 10. The S wave velocities over southern Vancouver Island are non-uniform; the low ray path density in cells (A,2) and (A,5) indicate that this may be a consequence of the modelling procedure rather than real earth structure. To the north of the Island, (B,2),

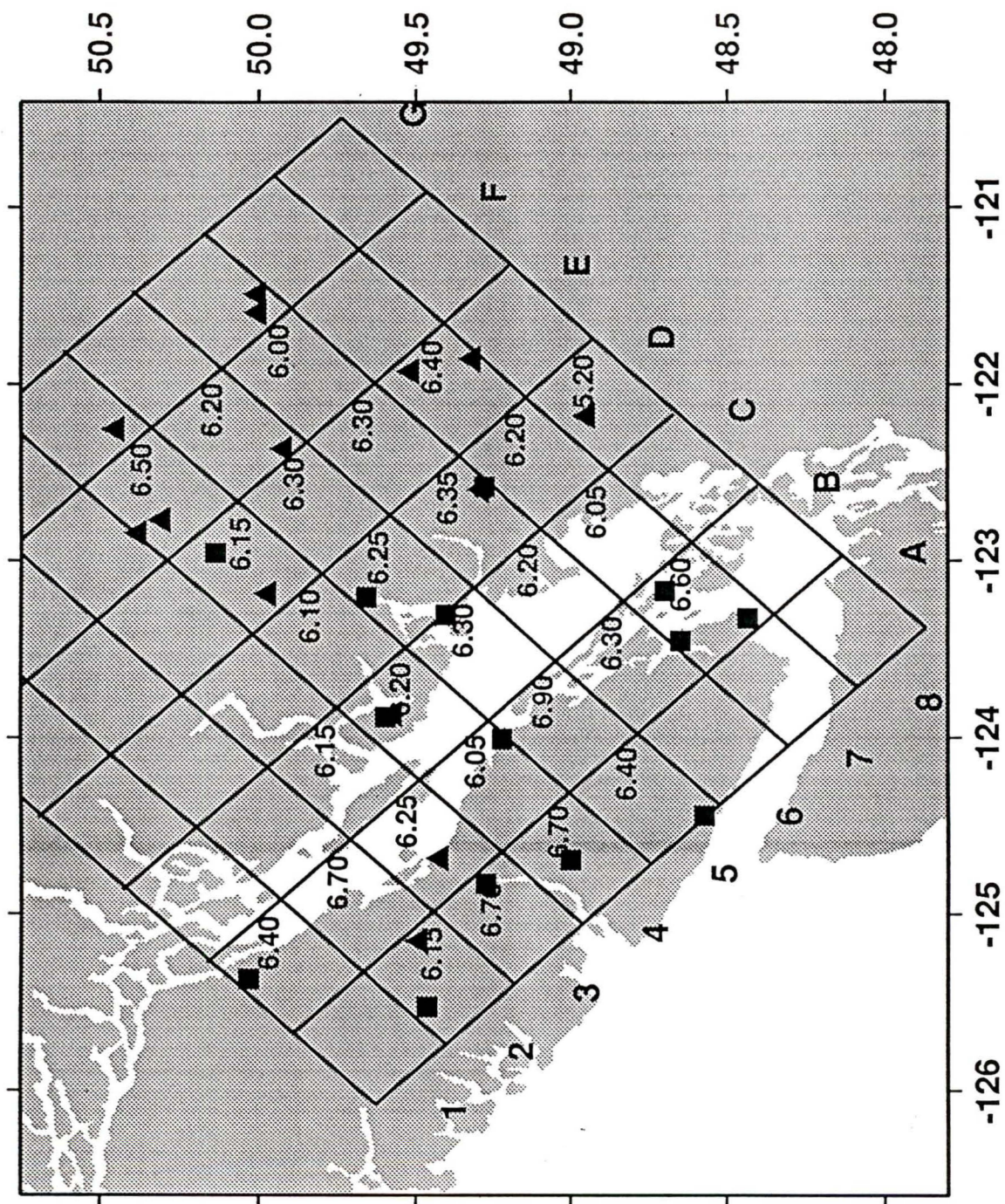


Figure 28: P velocities on a 8x7 along strike grid with a 147 km offset cutoff imposed on the data set, resulting in a 95 trace data set. Most elements have changed little from the final model (Figure 25), indicating that high velocities are not the result of deeply penetrating rays. The results also indicate that the reduced data set is causing instabilities in other areas of the model, especially in the south of Vancouver Island.

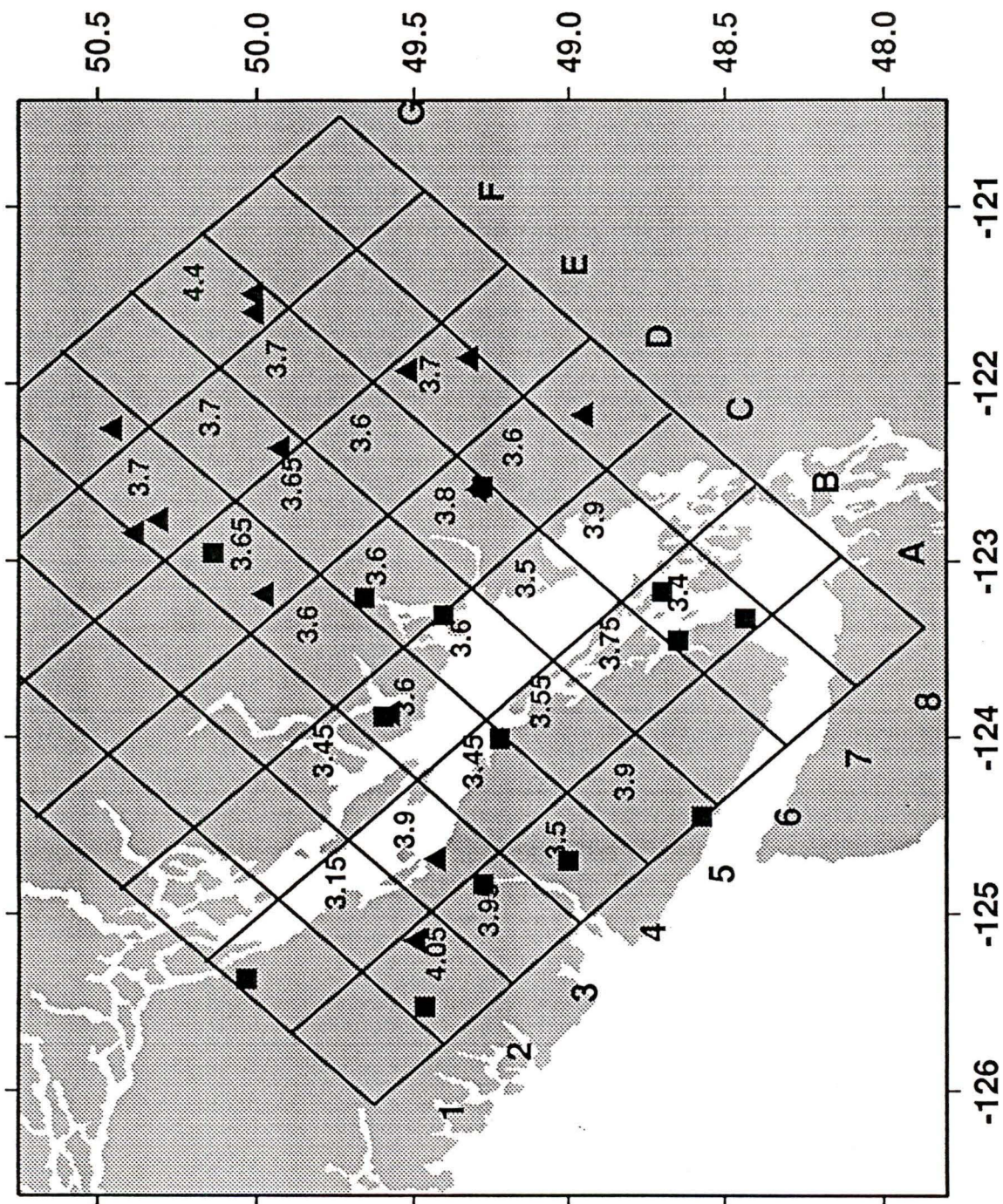


Figure 29: The final S wave inversion velocity model using the observed S wave data set with a 8x7 along strike grid after 50 iterations. The starting model had velocities of 3.60 km/s in all the grid elements and a near surface velocity of 2.40 km/s. Velocities are the same over most of the study area at ~ 3.6 km/s (see text for further discussion). No offset cutoff has been applied to the original data set.

	A	B	C	D	E	F	G
1	0	54	50	0	0	0	0
2	195	202	75	51	0	0	0
3	119	562	239	133	92	7	0
4	160	428	671	623	466	259	32
5	197	311	616	892	689	166	0
6	25	287	332	457	689	891	121
7	0	351	323	347	401	38	0
8	0	25	58	85	3	0	0

Table 10: Distance travelled by the ray paths within each grid element on a 8x7 along strike grid. The ray paths are those of the S wave observational data set, used to produce the model shown in Figure 29.

there is a low velocity of 3.15 km/s, which is surrounded by cells with velocities greater than 3.9 km/s. It is possible that the grid spacing is too fine in this region. The average velocity of these four cells is 3.75 km/s; a more plausible estimate for the area. Grid elements over the Georgia Strait and mainland both show S wave velocities between 3.60 and 3.70 km/s.

4.5 POISSON'S RATIO RESULTS

The final P and S wave velocity models, as shown in Figures 25 and 29 respectively, were both produced using the same grid dimensions. These results allow for estimates of the Poisson's ratio, σ , to be made over the grid using the equation

$$\sigma = \frac{1 - \frac{1}{2} \frac{V_p^2}{V_s^2}}{1 - \frac{V_p^2}{V_s^2}} \quad \text{Eq.9}$$

which can be obtained by simple manipulation of the basic equations for V_p , V_s and σ in terms of the elastic constants (Sheriff and Geldart 1982). The Poisson's ratio model for the upper crust is shown in Fig 30. The non-uniform S wave structure for Vancouver Island has produced equally scattered Poisson's ratio values. The S wave velocities in (B,2) and (B,3) give unreliable Poisson's ratios. However, averaging the nine grid elements that overlie Vancouver Island results in a Poisson's ratio of 0.27. Eastward in the Strait of Georgia and over the mainland values decrease to ~0.25. In the north Coast Belt all but one cell have a Poisson's ratio of 0.20-0.24.

The results from grid elements with unreliable P or S wave velocities are not shown in Figure 30.

4.6 NEAR SURFACE LAYER RESULTS

The near surface layer has been shown to vary greatly over the area being modelled (Zelt et al. 1993, O'Leary et al. 1994, McLean 1994). Along Line 3 of SCORE89, Zelt et al. (1993) found the near surface layer was between 600 m and 3.2 km in depth, whilst the average velocity in this layer was 5.4 km/s there were regions of low velocity (~3.2 km/s).

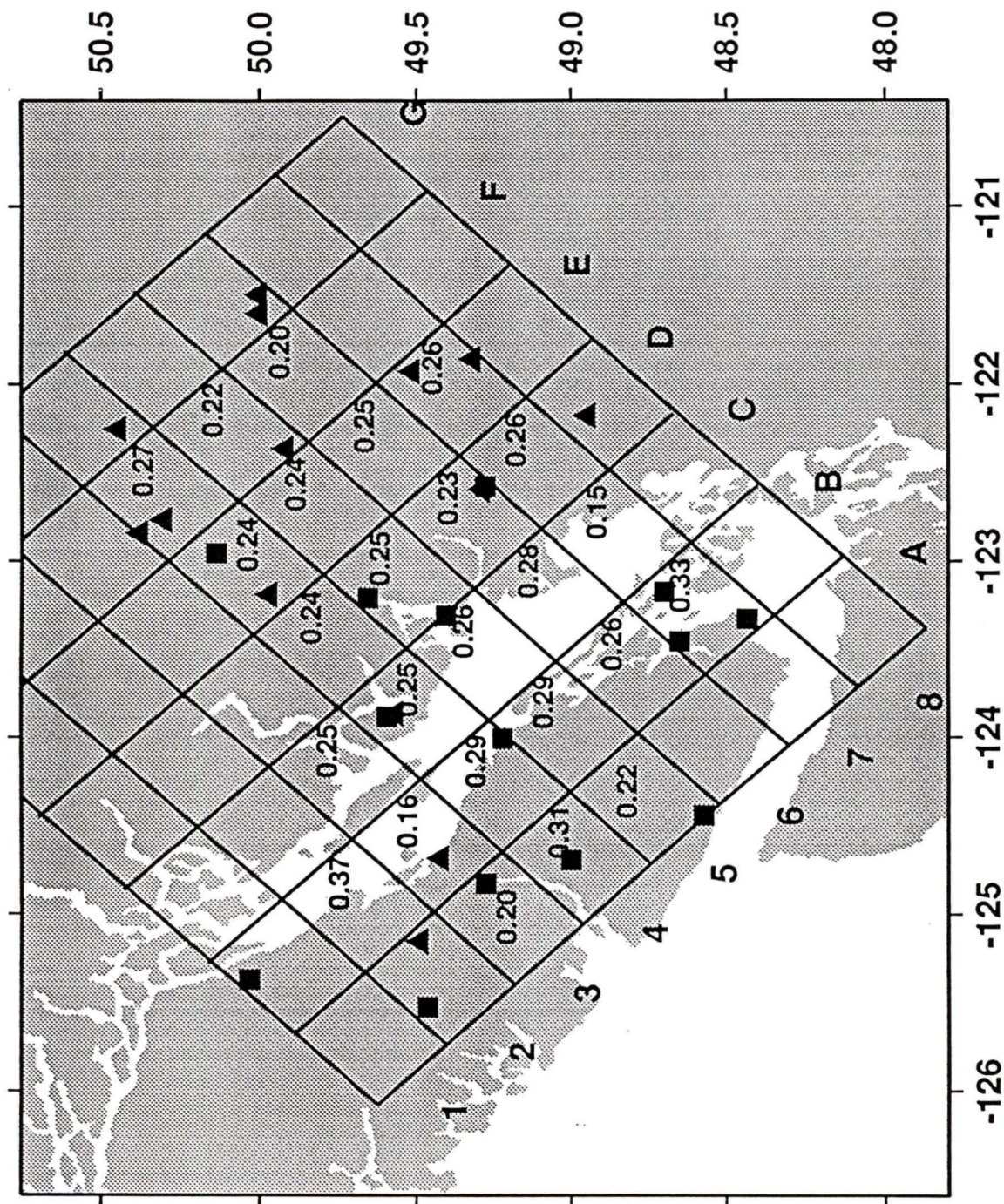


Figure 30: The final Poisson's ratio model using a 8x7 along strike grid. The model was constructed using P waves from Figure 25 and S waves from Figure 29. Vancouver Island has higher values of Poisson's ratio than the Georgia Strait and the mainland.

The inversion program fixed the near surface layer at 1.5 km throughout the model, and then calculated the velocity in this layer. Although this is not an accurate depiction of the real earth it does allow for the differentiation between velocities in the near surface and refracting layer.

The velocities in the near surface layer for 8x7 and 6x5 along strike grids, and rotated grids with the dimensions 7x7 and 5x5 are shown in Table 11. The values at each site vary, for the most part, by less than 1.0 km/s throughout the series of models. Sites which are consistently fast are the Whistler (WHB) and Haney (HNB) Stations and shotpoint 8, while low velocities are found at the Saturna Island Station (SNB) and shot point 91-1.

Sites whose velocities vary with the grid size and orientation used can be explained by changes in their underlying grid element. The elements beneath the near surface layer will cover different areas for each model and these changes will cause differing velocities in the grid elements. The near surface is seen to be effected also by this changes. The near surface velocities and grid velocities are not totally independent from each other when using the real data sets.

The shot points 7 and 23 were less than 1 km apart and the near surface velocities at the sites are within 0.5 km/s of each other for all the models. However other sites in close proximity do not show similar velocities to one another. The

	8X7	7X7	6X5	5X5	T-T
ALB	4.1	3.8	3.3	4.4	2.9
BIB	4.9	4.7	5.1	4.5	3.7
BTB	4.7	3.7	4.6	4.0	3.1
CBB	4.4	4.0	4.2	4.1	5.5
HNB	5.5	5.2	5.6	5.2	5.0
MGB	3.4	3.7	3.4	3.8	5.0
NAB	6.3	5.7	5.5	5.7	4.3
PFB	4.7	4.6	5.7	4.0	6.3
PGC	3.6	4.1	2.9	4.0	3.7
SHB	5.4	4.8	5.9	4.0	3.3
SNB	2.0	1.8	1.4	1.9	1.7
VGZ	4.5	4.7	6.2	6.3	5.8
WHB	6.1	6.1	6.5	6.1	5.3
WPB	4.3	3.7	4.6	3.8	3.2
4	3.2	3.1	2.5	3.8	3.0
6	4.6	4.6	4.3	5.0	3.5
7	5.1	3.7	3.9	4.2	2.1
8	5.8	6.2	6.1	5.7	5.9
9	4.8	5.2	4.6	5.2	4.7
10	3.4	3.5	3.7	3.4	3.3
11	4.7	4.5	4.5	4.5	2.8
12	2.8	3.9	3.0	3.6	2.4
21	3.2	3.3	4.9	3.1	3.3
23	5.5	4.1	4.2	4.6	2.3
46	5.2	3.7	4.8	4.9	4.5
47	4.6	5.9	4.0	5.1	3.4
48	3.7	4.9	3.9	4.2	3.0
91-1	4.3	2.6	2.6	3.1	2.2

Table 11: Velocities in the near surface layer for 8x7 and 6x5 along strike grids, and 7x7 and 5x5 rotated grids. The last column shows the results using a time term method.

velocity difference between shot point 10 and Sechelt Station (SHB), which are separated by 3 km, is 2.0 km/s and the difference between shot point 4 and Haney Station (HNB), a distance of 2.5 km apart, is 2.3 km/s. Possible explanation of the discrepancies are highly localized variations in upper crust velocities. The near surface velocities at shot point 7 and Haney Station (HNB) disagree in all models implying that rays from the two sites travel through different structure.

A further test was run using the P wave data set. By not allowing the upper velocity layer to vary from its starting model value of 4.2 km/s at all site locations the dependency of the grid elements on the near surface layer will become apparent. Figure 31 shows the results of this test. The overall velocity character of the grid remains similar to the final model shown in Figure 25, but several changes are evident. The r.m.s. of the residuals between grid velocities in Figures 25 and 31 is 0.15 km/s. Sites which were found to have fast or slow upper layer velocities in the final model have 'transferred' some of the anomaly to the underlying grid element. For example the 6.35 km/s velocity at (A,2) in Figure 25 is 6.45 km/s in Figure 31. This increase is suspected to have been caused by the fast near surface layer around shot point 8.

An independent estimate of the near surface layer was made using a time term method as described briefly in Section 3.1 which assumes a constant velocity refracting layer.

Details of the method applied to the explosion data set are described in Appendix 4. The results are included in Table 11 for comparison with the inversion method results. The time term method requires the addition of an arbitrary time term at one site to produce a non-singular solution. This value was chosen so that the shotpoint 10 and Sechelt Station had the same near surface velocity. The five anomalous sites observed in the inversion results are also seen in the time term data.

4.7 Uncertainties in velocities and Poisson's ratio

The P velocities, S velocities and Poisson's ratio given in the grid elements of Figures 25, 29 and 30, respectively have no associated uncertainty estimate with them. This omission was made primarily because the inversion routine provides no such error estimates. A qualitative error analysis may still be undertaken by considering the factors that control the accuracy of results. As previously mentioned high ray path density within a grid element will produce a more reliable result; a convenient measure of this quality is the number of km of ray path within an element. Secondly, a large number of ray paths within a cell is preferable as this will reduce the effects of anomalous near surface results at one site spreading throughout the model. Third, coverage over a large range of azimuths is desirable. Finally the quality of the arrival picks will affect the results.

In the testing of the inversion program it was found that

the ray path length within grid elements made a good measure of result reliability. This quantity will be used as the only constraint on creating error bound estimates for the final velocity inversions and Poisson's ratio models.

The results in Figure 10 and corresponding path lengths in Table 5 show that the inversion reproduces the test model in cells which have a path length of less than 50 km. However, such low path densities produce spurious results with the P and S wave observational data sets. From this we may conclude that the test results would produce lower error estimates than are likely to be seen on the noisier observational data set.

In order to calculate velocity and Poisson's ratio error bound estimates for each element of the refracting grid the results of Figures 26, 27 and 28 were used, along with other inversions using grid sizes of various dimensions and orientations. Table 12 shows the qualitative error estimates made from this analysis in which four ranges of error bound are given in relation to the number of km of ray path within that cell. The error estimates for a velocity apply to both the P and S wave results. The errors for Poisson's ratio will be affected by errors in both the P and S velocities. However, for simplicity the Poisson's ratio error estimates were calculated with the assumption that it was affected by only S wave ray path lengths.

Ray path (km)	Error in velocity (km/s)	Error in σ
0-50	± 1.0	± 0.05
100-250	± 0.2	± 0.04
250-400	± 0.1	± 0.03
400+	± 0.05	± 0.01

Table 12: Velocity and Poisson's ratio error estimates for a grid element as given by the length of ray path in that element.

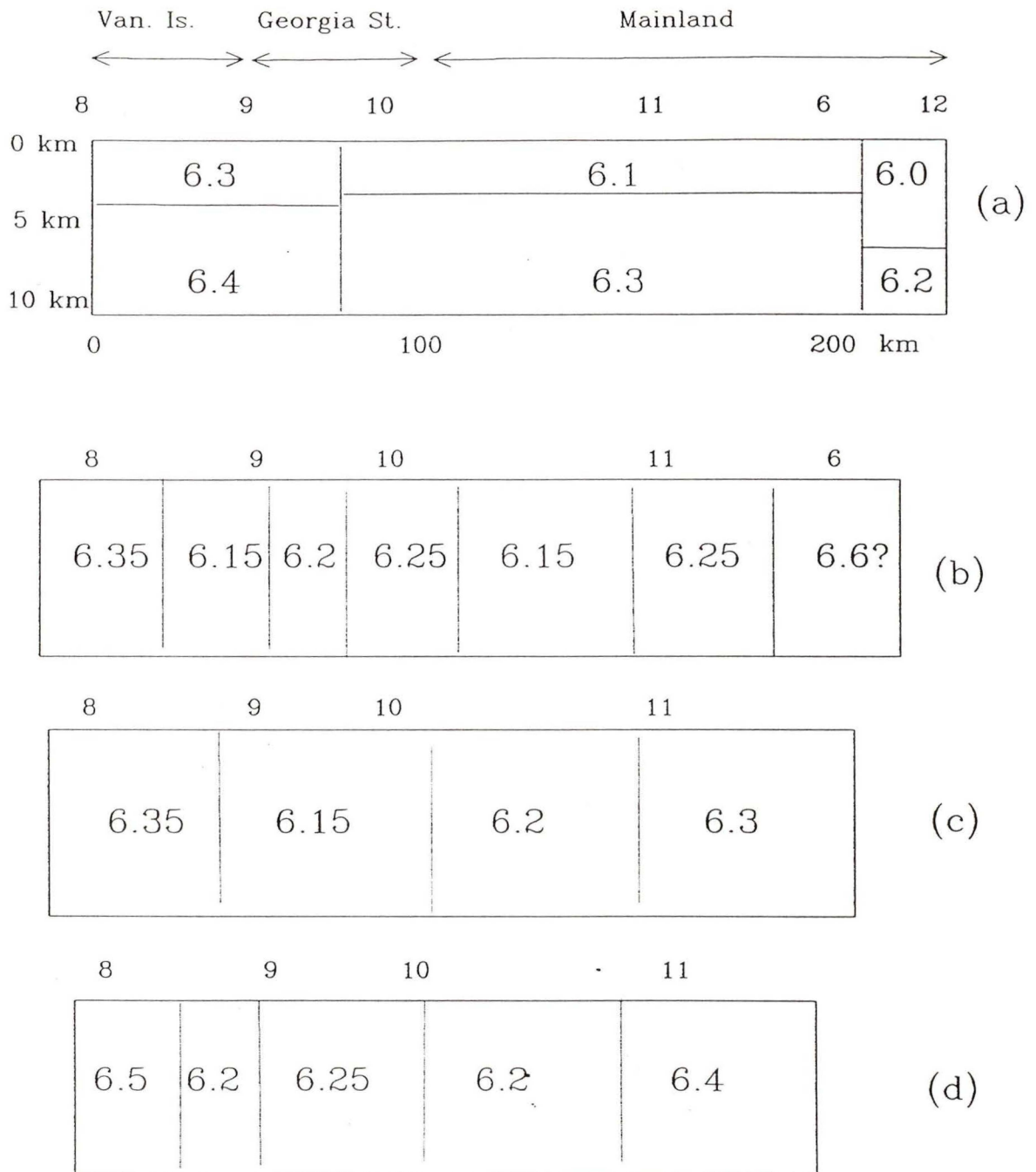


Figure 32: (a) Upper crust from the SCoRE Line 2 interpretation (Mclean 1994). Shotpoints are given across the top of the model and offset distances from shotpoint 8 along the bottom. The velocities along this profile for grids of various dimensions produced by the inversion are shown below for comparison. (b) 8x7 along strike grid (c) 6x5 along strike grid (d) 7x7 rotated grid. In all models, high velocities over Vancouver Island which decrease eastward over the Georgia Strait and into the Coast Belt are seen.

CHAPTER FIVE - DISCUSSION

5.1 COMPARISON WITH REFRACTION PROFILES

Many areas of the P wave inversion grid have been covered by traditional in-line two dimensional experiments. By considering cross sections of the final three dimensional grid, comparisons of velocity with the P wave estimates of previous refraction profiles will now be undertaken.

The results of the Line 2 of SCoRE89 (McClean 1994) are summarized in Figure 32(a) which shows the average structure of the upper 10 km. A cross section which followed the same path as Line 2 was taken from the 8x7 grid (Figure 32b). Comparing figure 32(a) and 32(b), we see the Vancouver Island P velocities are highest in both models at approximately 6.4 km/s. Both models also produce a decrease to the east of Georgia Strait although the boundary is not well resolved due to the fixed grid dimensions. Beyond 200 km offset the Line 2 interpretation decreases again in the upper crust to 6.0-6.2 km/s (Figure 32a); this is not observed in the along-strike model (Figure 32b), but this is not a reliably modeled section of the crust (see Section 4.1).

The results of an along strike grid with dimensions 6x5 are shown in Figure 32(c) and the 7x7 rotated grid in Figure 32(d). The general eastward velocity decrease is resolved by both of the models. The 6x5 grid more closely resembles the Line 2 interpretation (McClean 1994) at the eastern edge, with low velocities of 6.2-6.3 km/s.

The upper crustal P wave structure from Line 3 of SCoRE (Zelt et al. 1993) is shown in Figure 33(a). The profiles for 8x7 and 6x5 along-strike grids and the 7x7 rotated grid are shown in Figures 33 (b), (c), and (d), respectively. The shots 8,9, and 10 were used in both Lines 2 and 3 of Score and so the first 100 km of the profiles have already been discussed in reference to line 2 above. The Line 3 interpretation (Zelt et al. 1993) depicts the top of the upper crust decreasing eastward from 6.25 km/s at a 50 km model distance to 6.15 km/s at 250 km, while at 10 km depth varies little with a velocity of 6.45 km/s. The results from the 8x7 grid at distances greater than 150 km show velocities associated with the bottom of the upper crust, between 6.30-6.50 km/s. This is understandable when considering that the high offset region is modelled by rays which come from the eastern edge of the study region and so have travelled large distances to receivers. The results in Figures 33 (c) and (d) are similar to the 8x7 model.

McMechan and Spence (1983) resolved an upper crustal velocity of 6.50-6.75 km/s along southern Vancouver Island. Velocities in the final P wave inversion over this region range from 6.45 to 6.65 km/s.

In doing this type of comparison discrepancies may arise for several reasons. (1) The two dimensional nature of the refraction line interpretations means that some velocity structures may be limited in lateral extent. These may not

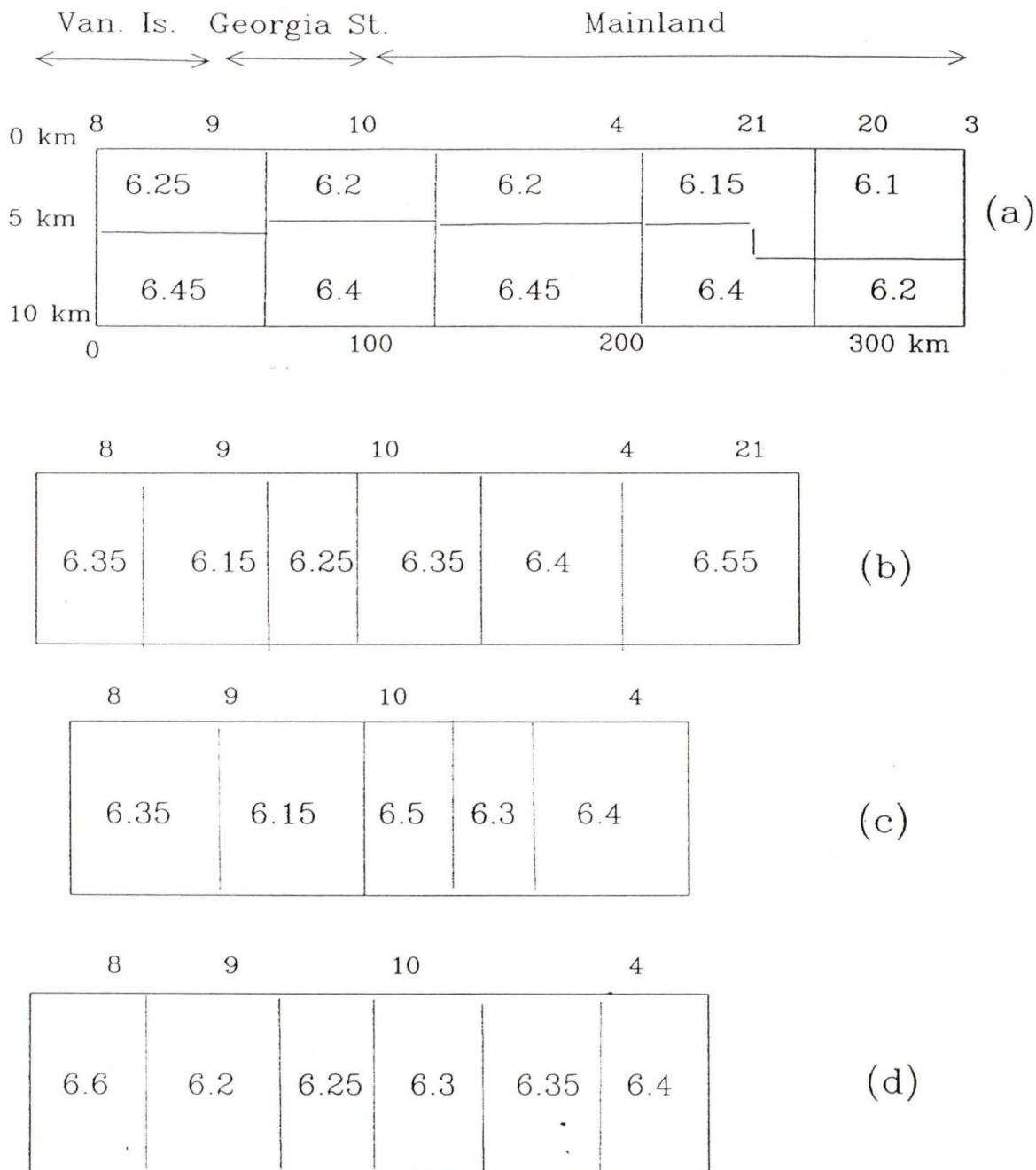


Figure 33: (a) Upper crust from the SCoRE Line 3 interpretation (Zelt et al. 1993). Shotpoints are given across the top of the model and offset distances from shotpoint 8 along the bottom. The velocities along this profile for grids of various dimensions produced by the inversion program are shown below for comparison. (b) 8x7 along strike grid (c) 6x5 along strike grid (d) 7x7 rotated grid. Over the first 100 km the same region as in Figure 32 was covered. Beyond here the inversion models show velocities associated with the bottom of the upper crust as interpreted by Zelt et al. (1993).

have been crossed by the travel paths producing the three dimensional travel times. (2) The velocities within each cell of the grid are essentially averages within predetermined boundaries, and so will not correspond to the velocity boundaries from the SCoRE interpretations. (3) There is always the possibility of anisotropy within the rocks.

5.2 IMPLICATIONS OF RESULTS

P and S wave velocities were calculated over the Southern Insular and Coast Belts using travel times from refraction experiment explosions recorded on the WCTN seismic network. Velocities were determined by two methods: an in-line refraction graphical method and a tomographic inversion procedure. Only ray paths considered to be travelling in the top 10 km of the crust were used, and so all velocity estimates are for the upper crust.

Results from both the in-line refraction and inversion methods indicate that P wave velocities, at around 6.55 km/s, are higher over Southern Vancouver Island than they are within the Coast Belt, where representative velocities are 6.30 km/s. The inversion model results also show a low velocity region in the Georgia Strait which may be associated with the Nanaimo sediments. The P wave results are generally consistent with previous refraction interpretations in the region.

S wave information can provide additional constraints in estimating rock properties. The in-line refraction data reveal

that the S wave velocities over the study region are about 3.6 km/s, with slightly higher velocities of 3.73 km/s over the Southern Gulf Islands. The tomographic inversion also reproduces this anomalous zone in the Gulf Islands and the ~3.6 km/s velocities of the mainland. Velocities on Vancouver Island are also approximately 3.7 km/s but vary from 3.15-4.05 km/s, which is more likely a product of low ray coverage rather than a representation of the real earth.

The P and S wave velocities allow for the calculation of Poisson's ratio. Poisson's ratio is affected by several physical properties of crustal rocks. The felsic-mafic composition of the rocks is an important control on Poisson's ratio with more mafic rocks producing a higher Poisson's ratio. In laboratory experiments Poisson's ratio was found to be 0.206 for granites with a high proportion of quartz (Hall and Ali 1985), while fresh basalt and gabbro are typically 0.30 (Hyndman 1979, Robbinson et al. 1982). The water content within pores and cracks can also be of great influence, with Poisson's ratio increasing when water is present (Nur and Simmons 1969). The grain geometry of pores and fractures also influences Poisson's ratio, with thin cracks exhibiting a greater increase than equidimensional pores. (O'Connell and Budiansky 1977). Figure 34(a) shows the amount of variation that both porosity and the aspect ratio of the grain boundaries can produce in Poisson's ratio. For thin cracks, represented by small aspect ratios, Poisson's ratio rises

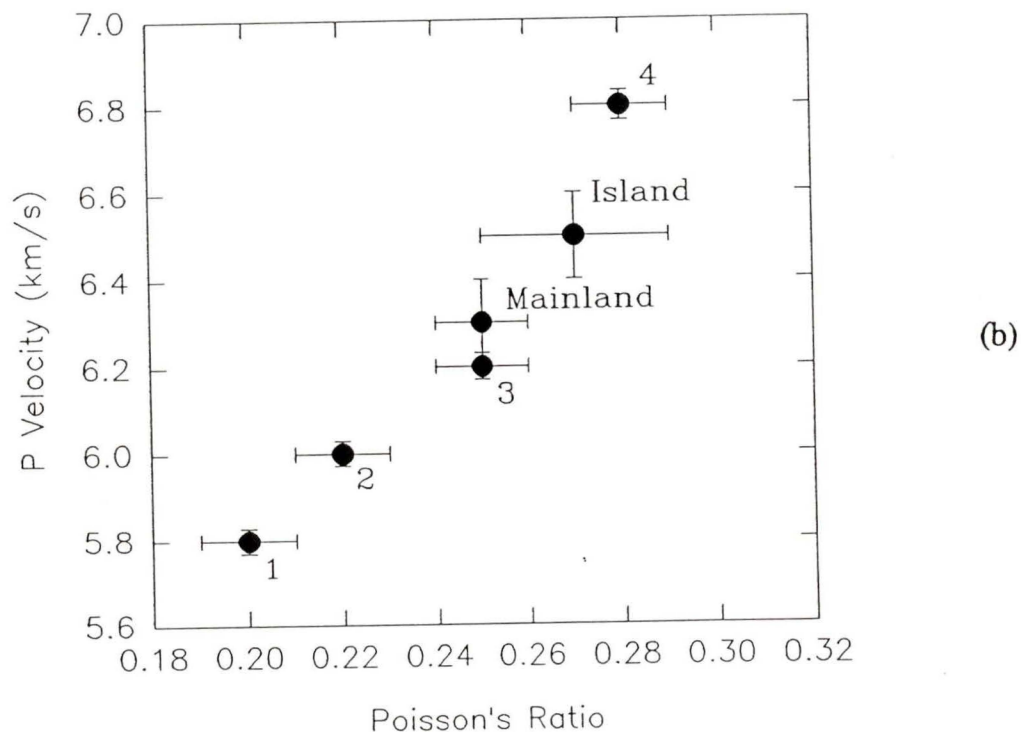
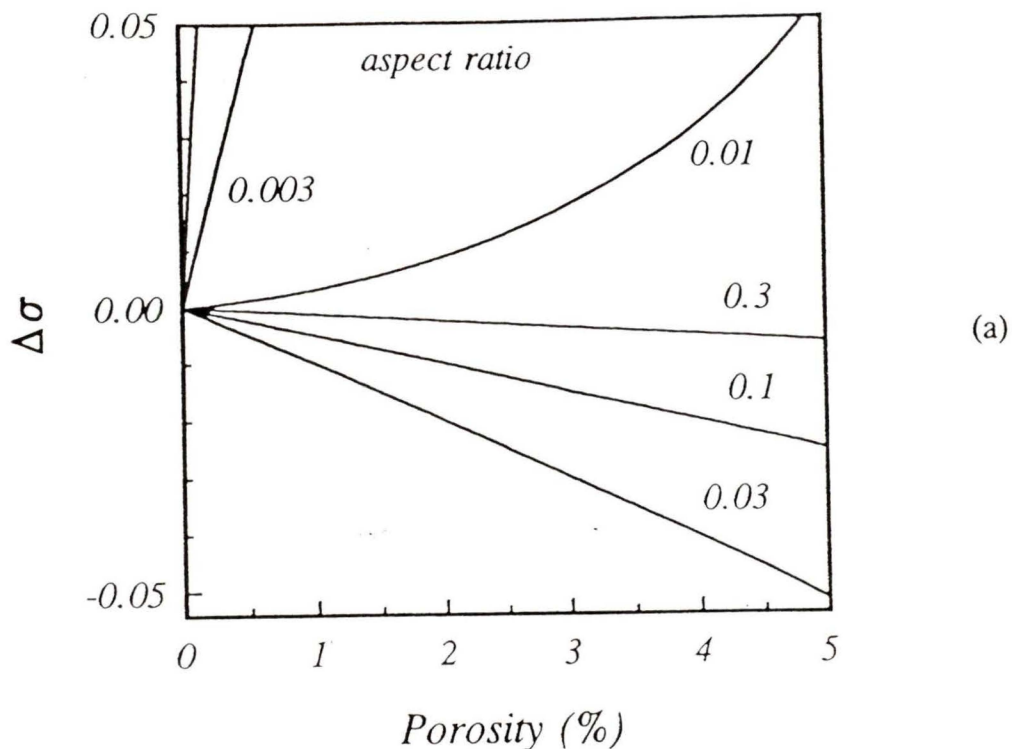


Figure 34: (a) Poisson's ratio - Porosity relation for selected pore aspect ratios (from Marquis 1992) (b) P velocity against Poisson's ratio for several rock-forming compositions (from Hall and Ali 1985) : (1) Quatzofeldspathic gneisses (2) Granities (3) A lithology transition between 2 and 4 (4) Pyroxene granulities. From the in-line refraction results P velocities and Poisson's ratio's are also shown for Vancouver Island and the mainland.

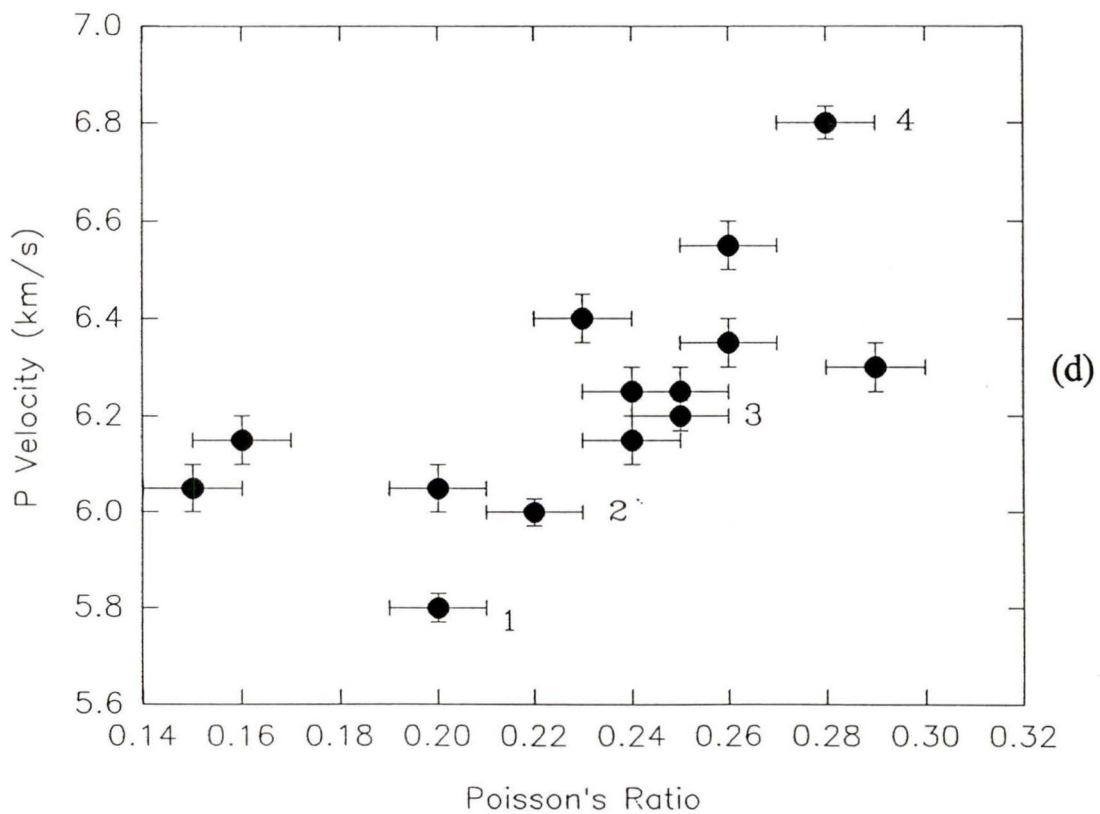
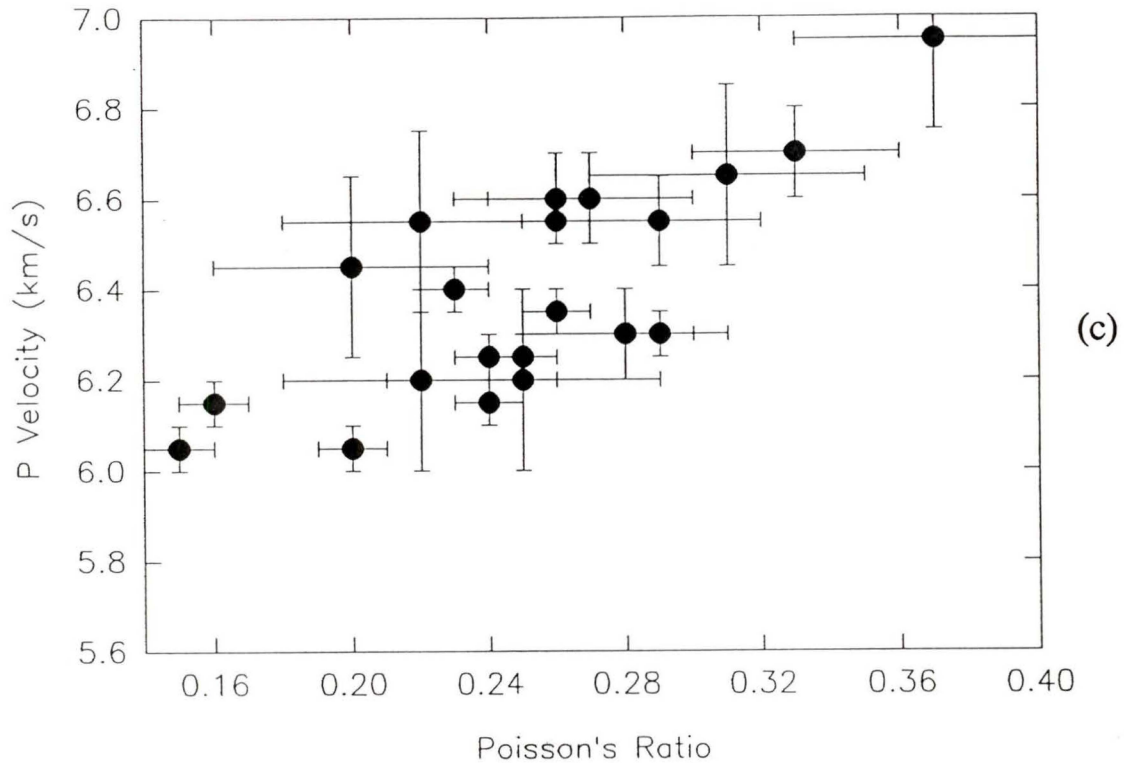


Figure 34: (c) P Velocity against Poisson's ratio, with all tomographic results shown. (d) P velocity against Poisson's ratio with well constrained tomographic results shown.

rapidly with increasing porosity. However, as the pore size approaches spherical, Poisson's ratio decreases with increasing porosity (Marquis 1992).

Poisson's ratio results from the in-line data sets show a high of 0.27 over southern Vancouver Island. The uncertainty associated with the S wave velocities from the tomographic inversion over Vancouver Island also bring to bear some reservations about the Poisson's ratio estimates in this area. However, the overall pattern is seen to be that of high values of 0.27-0.28.

In-line Poisson's ratios for the mainland range from 0.24 to 0.25, while the inversion procedure over this area gives values between 0.20 and 0.27. Both the Georgia Strait and mainland have lower Poisson's ratios than Vancouver Island.

Information on P velocities and Poisson's ratio can also be used in conjunction to make estimates of composition which are compatible with both sources. Figure 34(b) shows a graph of P velocity against Poisson's ratio from some common rock types, taken from Hall and Ali (1985), which are representative of the upper 3 km of Lewisian basement. Imposed upon the plot are points representative of Vancouver Island (P velocity=6.50 km/s, $\sigma=0.27$) and the mainland (P velocity=6.30 km/s, $\sigma=0.25$) from the in-line refraction results. Figure 34(b) shows that rocks with a high mafic content have higher P velocities and Poisson's ratios than more felsic rocks. The increase in P wave velocities and Poisson's ratio from the

Coast Belt to southern Vancouver Island are caused by a geological transition from the Triassic-Jurassic volcanics of the island to the Jura-Cretaceous intrusives of the Coast Belt. Figure 34(c) shows the final inversion model results of the P velocities and Poisson's ratios for all grid elements. The trend of P velocity and Poisson's ratio decreasing together is not readily observable, with a large range of P velocities being seen for any given Poisson's ratio. The removal of results in which P ray path lengths were less than 400 km should leave only the most reliable estimations of P velocity and Poisson's ratio from the final inversion models (the anomalous values being attributed to the pairing effect). Figure 34(d) shows such a plot. The points are in better agreement with those of Hall and Ali (1985), and so suggest the same conclusions as those reached for the in-line data.

The northern region of the Coast Belt has Poisson's ratios between 0.20 and 0.24. The high resistivity in this region, derived from magnetotelluric studies (Jones et al. 1992), means that the presence of free water is unlikely here. Gough and Majorowicz (1992) associate this high resistivity with granitoid plutons. Laboratory experiments and Poisson's ratio estimates from seismic work (Hall and Ali 1985) show that a high quartz content produces a drop in Poisson's ratio. The presence of the plutons, with a high quartz content, would suggest that they are responsible for the decrease in Poisson's ratio.

BIBLIOGRAPHY

Aki, K., and Richards, P.G. 1980. Quantitative Seismology, volume 2, W.H. Freeman, New York.

Aki, K., and Lee, W.H.K. 1976. Determination of three-dimensional velocity anomalies under a seismic array using first P arrival times from local earthquakes, 1, A homogeneous initial model. *Journal of Geophysical Research*, 81:4381-4399.

Berry, M.J., and Forsyth, D.A. 1975. Structure of the Canadian Cordillera from seismic refraction and other data. *Canadian Journal of Earth Sciences*, 12:182-208.

Berry, M.J., and West, G.F. 1966. An interpretation of the first-arrival data of the lake superior experiment by the time-term method. *Bulletin of the Seismological Society of America*, 56:141-171.

Coney, P.J., Jones, D.L., and Monger, J.W.H. 1980. Cordilleran suspect terranes. *Nature*, 288:329-333.

Drew, J.J., and Clowes, R.M. 1990. A re-interpretation of the seismic structure across the active subduction zone of western Canada. In *Studies of laterally heterogeneous structures using seismic refraction and reflection data*. Edited by A.G. Green, Geological survey of Canada, Paper 89-13, p. 115-132.

Gabrielse, H., and Yorath, C.J. 1989. DNAG#4. The Cordilleran orogen in Canada. *Geoscience Canada*, 16:67-83.

Gough, I.G., and Majorowicz, J.A. 1992. Magnetotelluric soundings, structure, and fluids in the southern Canadian Cordillera. *Canadian Journal of Earth Science*, 29:609-620.

Hall, J., and Ali, M. 1985. Shear waves in a seismic survey of Lewisian basement: an extra control on Lithological variation and porosity. *Quarterly Journal of the Geological Society of London*, 142:677-688.

Hyndman, R.D. 1979. Poisson's ratio in the oceanic crust-a review. *Tectonophysics*, 59:321-333.

Jones, A.G., Gough, D.I., Kurtz, R.D. et al. 1992. Electromagnetic images of regional structure in the southern Canadian Cordillera. *Geophysical Research Letters*, 12:2373-2376.

Journey, J.M., and Friedman, R.M. 1993. The Coast Belt thrust system: evidence of Late Cretaceous shortening in southwest British Columbia. *Tectonics*, 12:756-775.

Kanasewich, E.R., Burianyk, M.J.A., Ellis, R.M., Clowes, R.M., White, D.J., Côté, T., Forsyth, D.A., Luetgert, J.H., and Spence, G.D. 1994. Crustal velocity structure of the Omineca Belt, southeastern Canadian Cordillera. *Journal of Geophysical Research*, 99:2653-2670.

Massey, N.W.D. 1986. The Metchosin Igneous Complex, southern Vancouver Island; ophiolite stratigraphy developed in an emergent island setting. *Geology*, 14:602-605.

Marquis, G. 1992. Geophysical studies of saline fluids in the deep crust. Ph.D. thesis, University of Victoria.

McLean, N.A. 1994. Velocity structure from seismic refraction across Coast Plutonic and Intermontane Belts. M.Sc. Thesis, University of Victoria. (in preparation).

McMechan, G.A., and Spence, G.D. 1983. P-wave velocity structure of the Earth's crust beneath Vancouver Island. *Canadian Journal of Earth Sciences*, 20:742-752.

Monger, J.W.H. 1986. Geology between Harrison Lake and Fraser River, Hope map area, southwestern British Columbia. In *Current research, part B*. Geological Survey of Canada, Paper 86-1B, p.699-706.

Monger, J.W.H., and Price, R.A. 1979. Geodynamic evolution of the Canadian Cordillera-progress and problems. *Canadian Journal of Earth Sciences*, 16:770-791.

Monger, J.W.H., Price, R.A., and Tempelman-Kluit, D.J. 1982. Tectonic accretion and the origin of the two major metamorphic and plutonic belts in the Canadian Cordillera. *Geology*, 10:70-75.

Monger, J.W.H., and Journeay, J.M. 1992. A field guide to accompany the Penrose Conference on the Tectonic evolution of the Coast Mountains orogen, May 1992. 97 pp.

Muller, J.E. 1977. Evolution of the Pacific margin, Vancouver Island and adjacent regions, *Canadian Journal of Earth Science*, 14:384-396.

Nur, A., and Simmons, G. 1969. The effect of saturation on velocity in low porosity rocks. *Earth and Planetary Science Letters*, 7:183-193.

O'Connell, R.J., and Budiansky, B., 1977. Viscoelastic properties of fluid-saturated and cracked solids. *Journal of Geophysical Research*, 82:5719-5735.

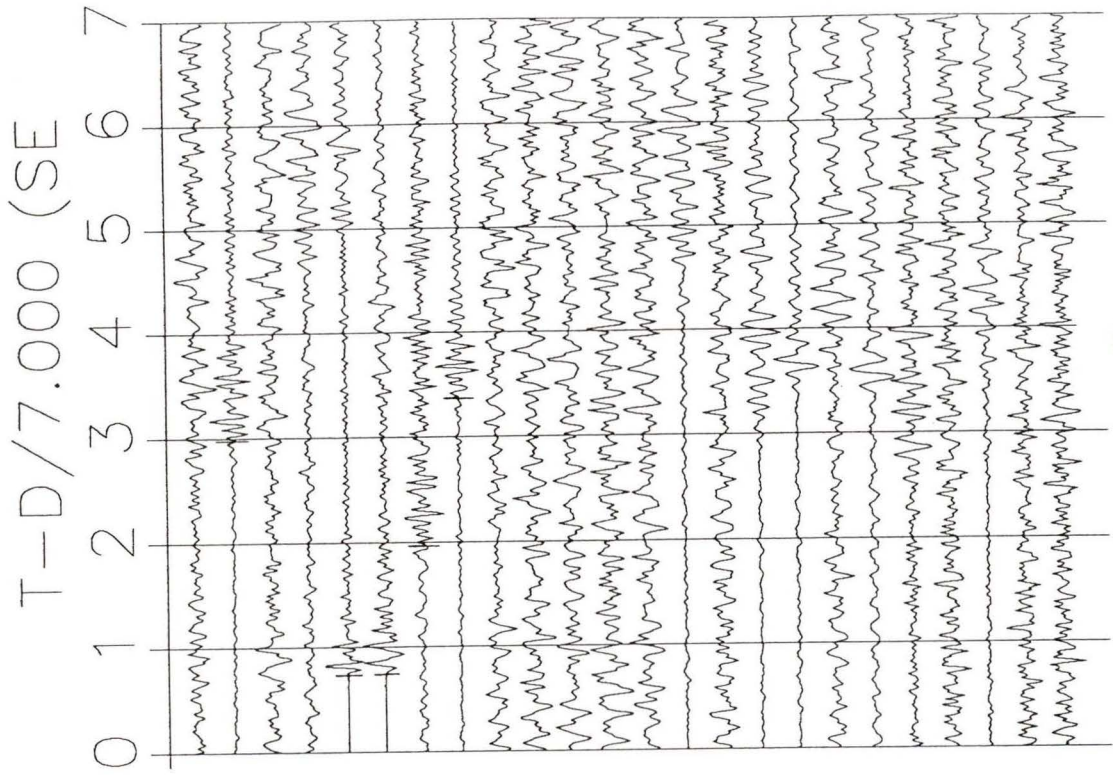
- O'Leary, D.M., Clowes, R.M., and Ellis, R.M. 1994. Crustal velocity structure in the Southern Coast Belt, British Columbia. *Canadian Journal of Earth Sciences*, (in Press).
- Raitt, R.W., Shor, G.G., Francis, T.J.G., Morris, G.B. 1969. Anisotropy of the Pacific upper mantle. *Journal of Geophysical Research*, 74:3095-3109.
- Riddihough, R.P. 1984. Recent movements of the Juan de Fuca plate system. *Journal of Geophysical Research*, 89:6980-6994.
- Robbinson, P.T., Hall, J.M., et al. 1982. The Iceland Research Drilling Project: synthesis of results and implications for the nature of Icelandic and oceanic crust. *Journal of Geophysical Research*, 87,6657-6667.
- Spence, G.D., Clowes, R.M., and Ellis, R.M. 1985. Seismic Structure across the active subduction zone of western Canada. *Journal of Geophysical Research*, 90:6754-6772.
- Scheidegger, A.E., and Willmore, P.L. 1957. The use of a least squares method for the interpretation of data from seismic surveys. *Geophysics*, 22:9-22.
- Sheriff, R.E., and Geldart, L.P. 1982. *Exploration seismology*, Volume 1, Cambridge University Press, Cambridge.
- Thurber, C.T. 1983. Earthquake locations and three-dimensional crustal structure in the Coyote Lake area, Central California. *Journal of Geophysical Research*, 88:8226-8236.
- Varsek, J.L., Cook, F.A., Clowes, R.M., Journeay, J.M., Monger, J.W.H., Parrish, R.R., Kanasewich, E.R., Spencer, C.S. 1993. Lithoprobe crustal reflection structure of the southern Canadian Cordillera II: Coast Mountains transect. *Tectonics*, 16:334-360.
- Zelt, B.C., Ellis, R.M., Clowes, R.M. 1994. Three-Dimensional velocity structure of the southwestern Canadian Cordillera from tomographic inversion of wide-angle seismic data. *CGU, Banff. Program with Abstracts*, 34.
- Zelt, B.C., Ellis, R.M., Clowes, R.M., Kanasewich, E.R., Asudeh, I., Luetgert, J.H., Hajnal, Z., Ikami, A., Spence, G.D., Hyndman, R.D. 1992. Crust and upper mantle velocity structure of the Intermontane Belt, southern Cordillera. *Canadian Journal of Earth Sciences*, 29:1530-1548.
- Zelt, B.C., Ellis, R.M., Clowes, R.M. 1993. Crustal velocity structure in the Eastern Insular and Southernmost Coast Belts. *Canadian Journal of Earth Sciences*, 37:1014-1027.

Zervas, C.E., and Crossen, R.S. 1986. P_n observation and interpretation in Washington. Bulletin of the Seismological Society of America, 76:521-546.

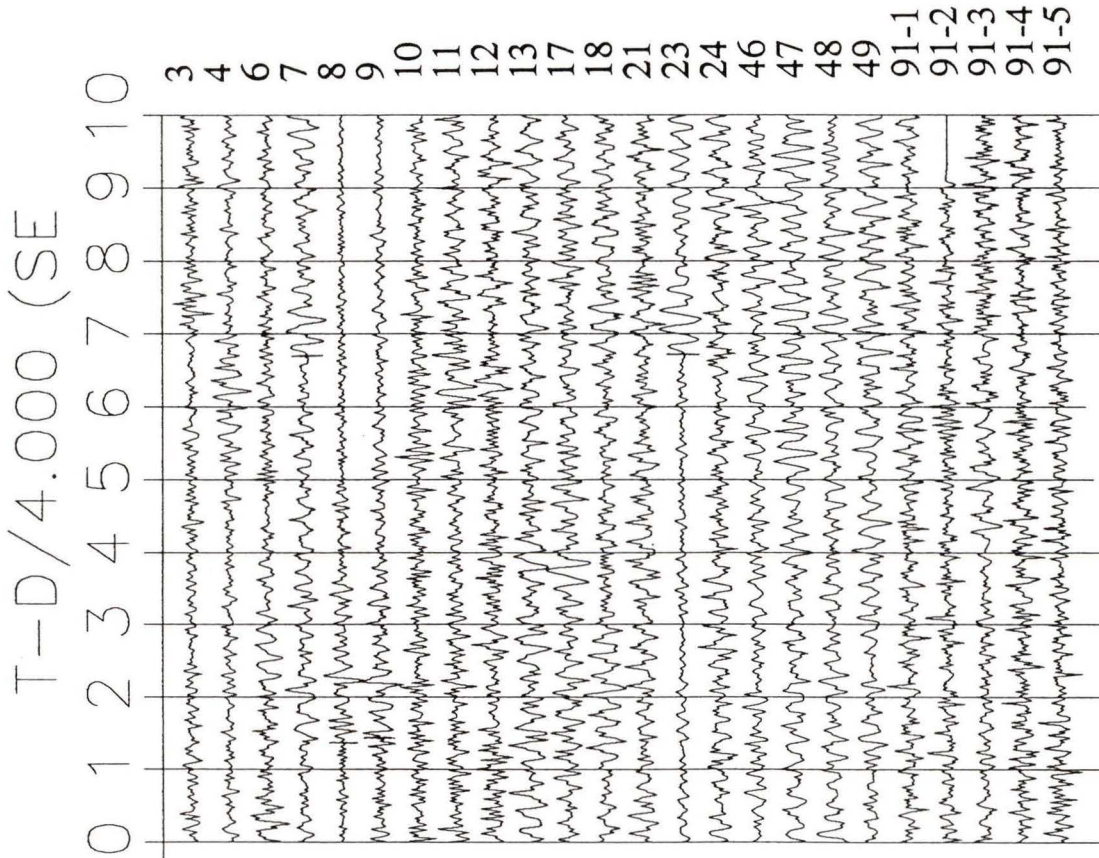
Zhu, H. and Ebel, J.E. 1994. Tomographic inversion for the seismic velocity structure beneath northern new england using seismic refraction data. Journal of Geophysical Research, 99:15331-15357.

APPENDIX 1

P and S wave seismograms recorded on the WCTN seismic network. The 18 stations used are listed in Table 1, and the 24 shots in Table 2. Travel time picks are shown by horizontal lines on the traces.



(a)



(b)

Figure 35. Seismograms at Port Alerni Station: (a) P wave arrivals (b) S wave arrivals.

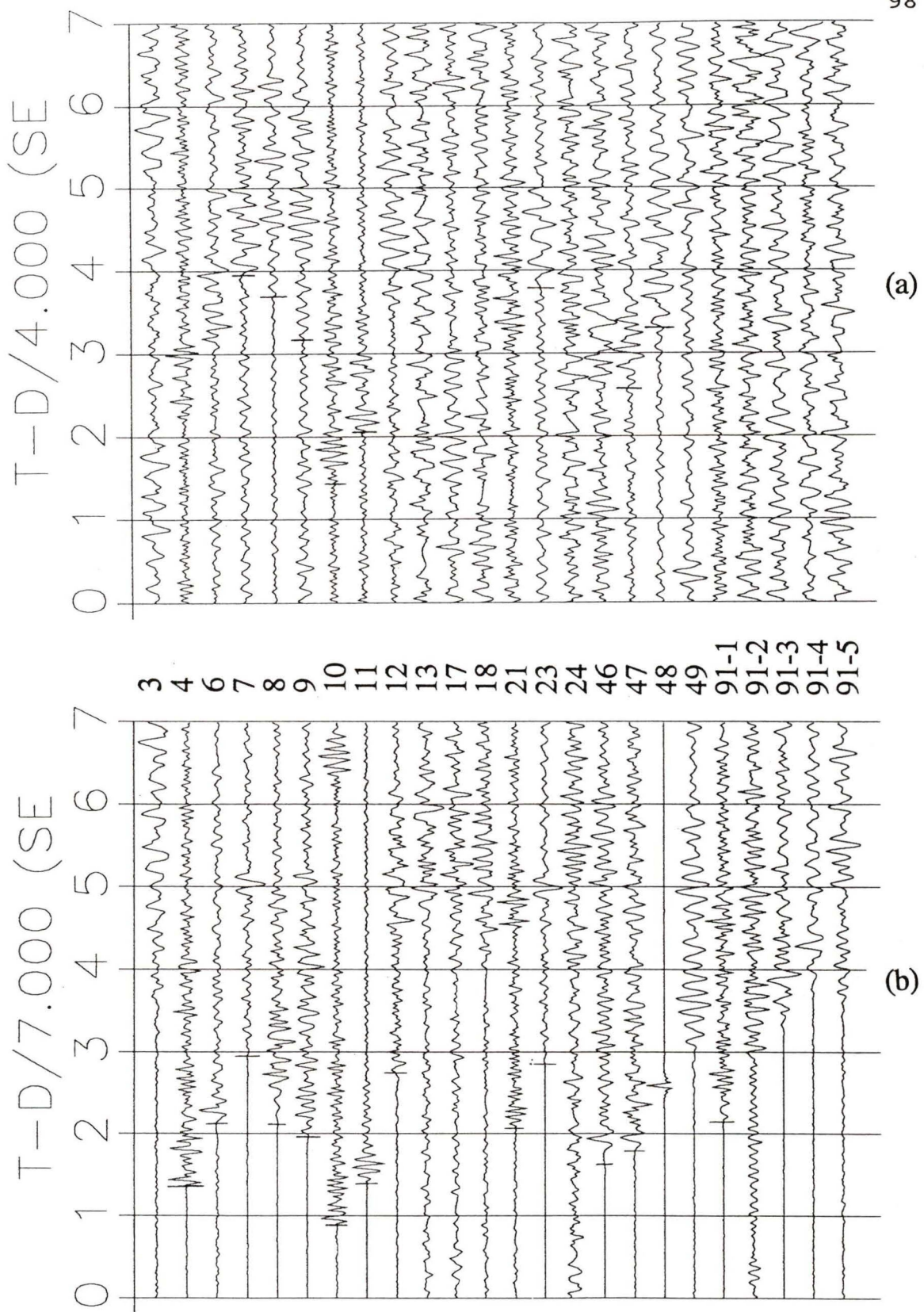
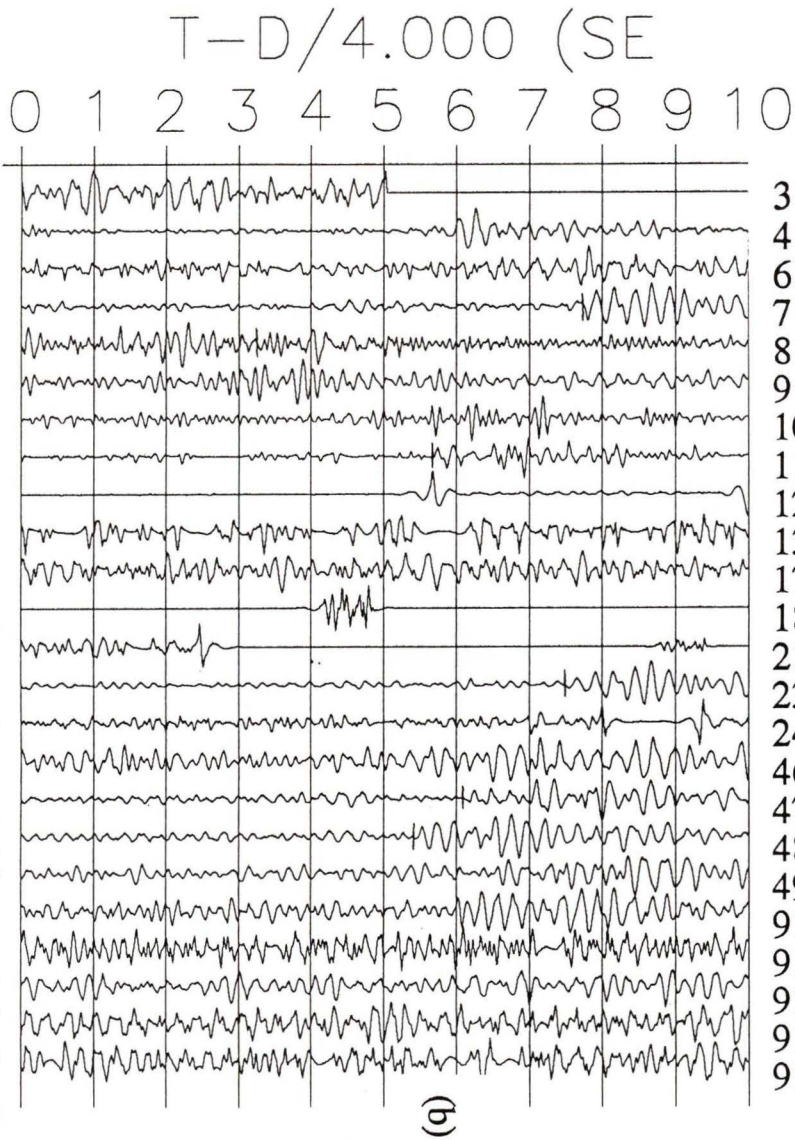


Figure 36. Seismograms at Bowen Island Station: (a) P wave arrivals (b) S wave arrivals.

Figure 37. Seismograms at Buttle Lake Station: (a) P wave arrivals (b) S wave arrivals.



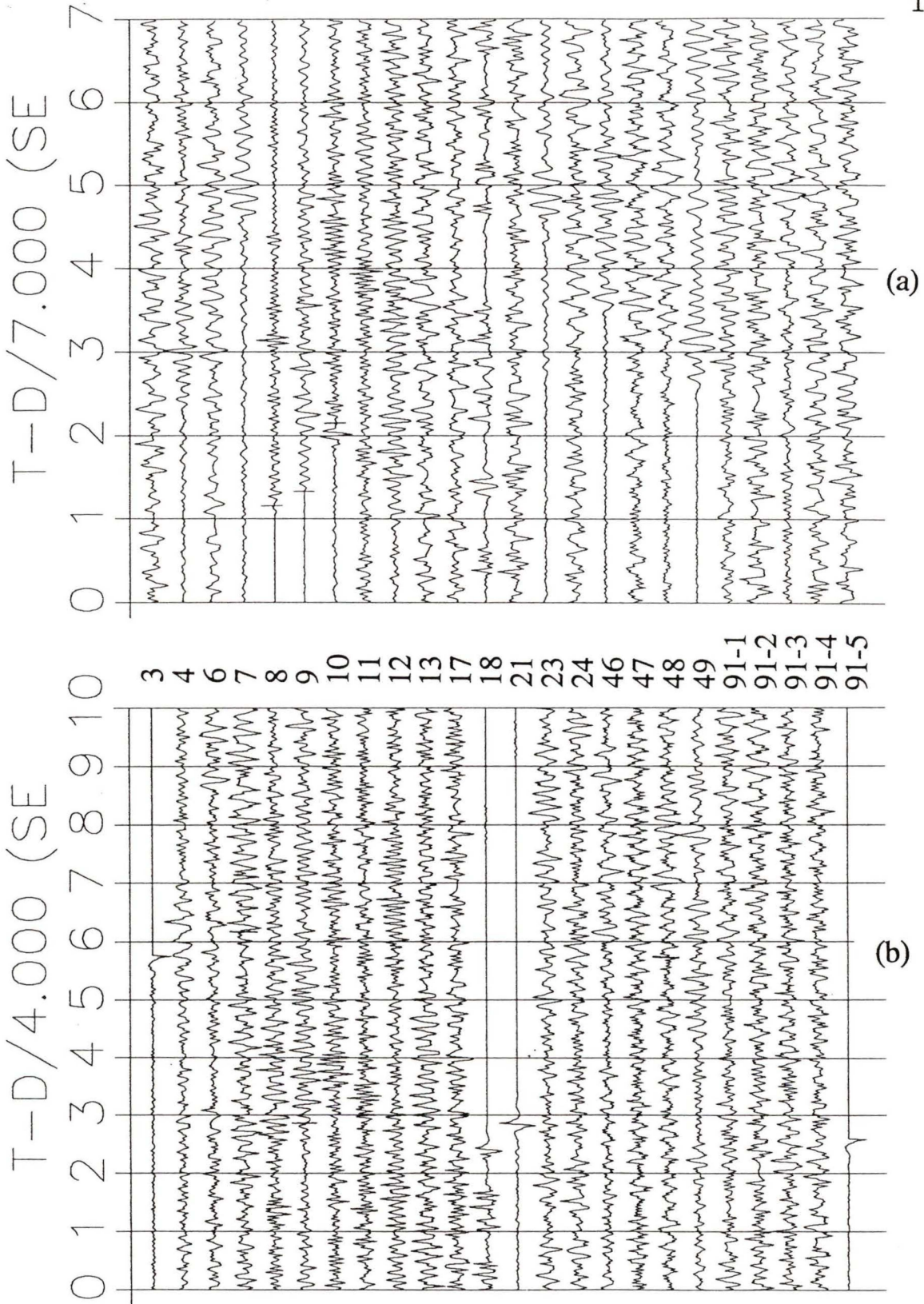


Figure 38. Seismograms at Campbell River Station: (a) P wave arrivals (b) S wave arrivals.

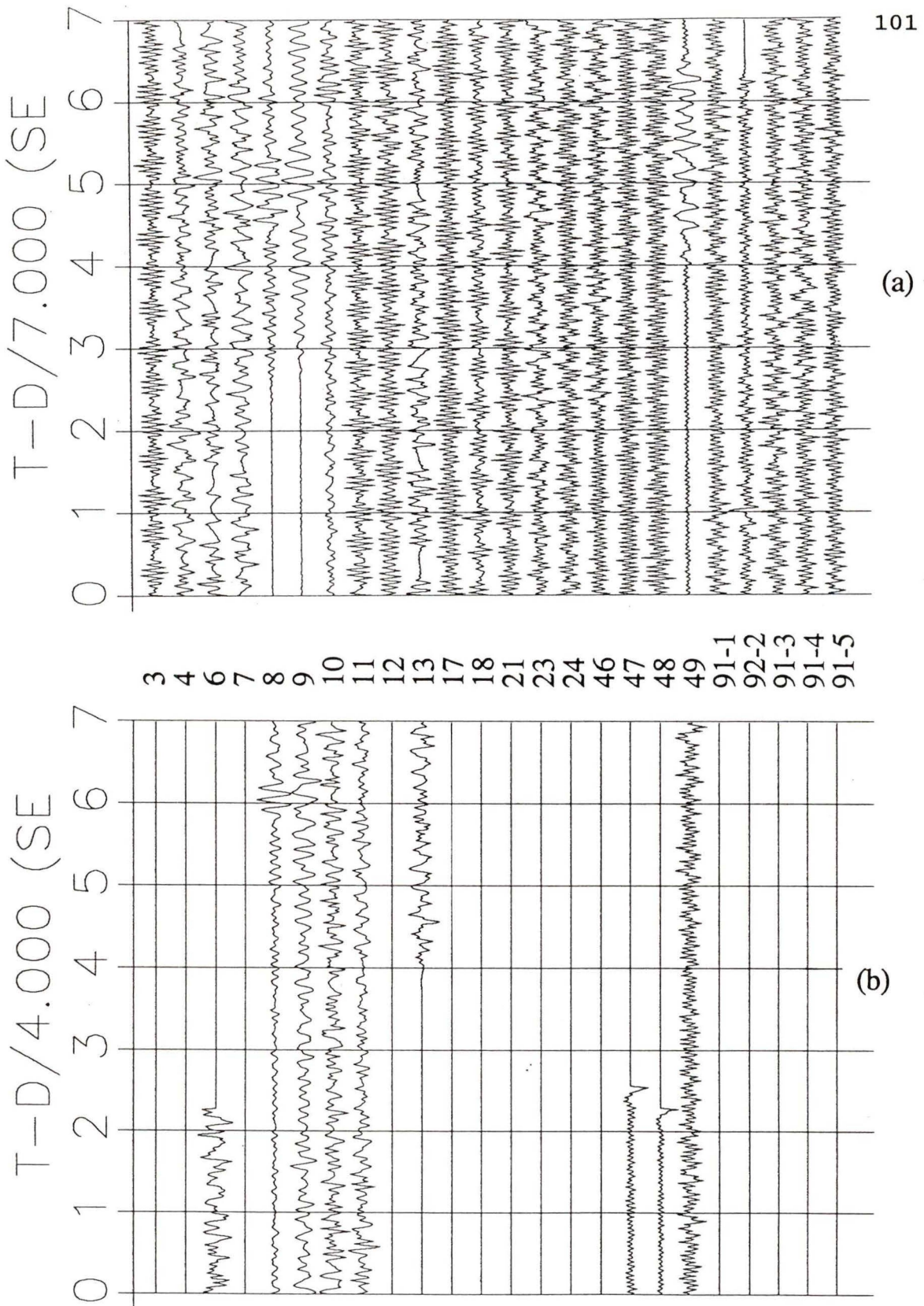
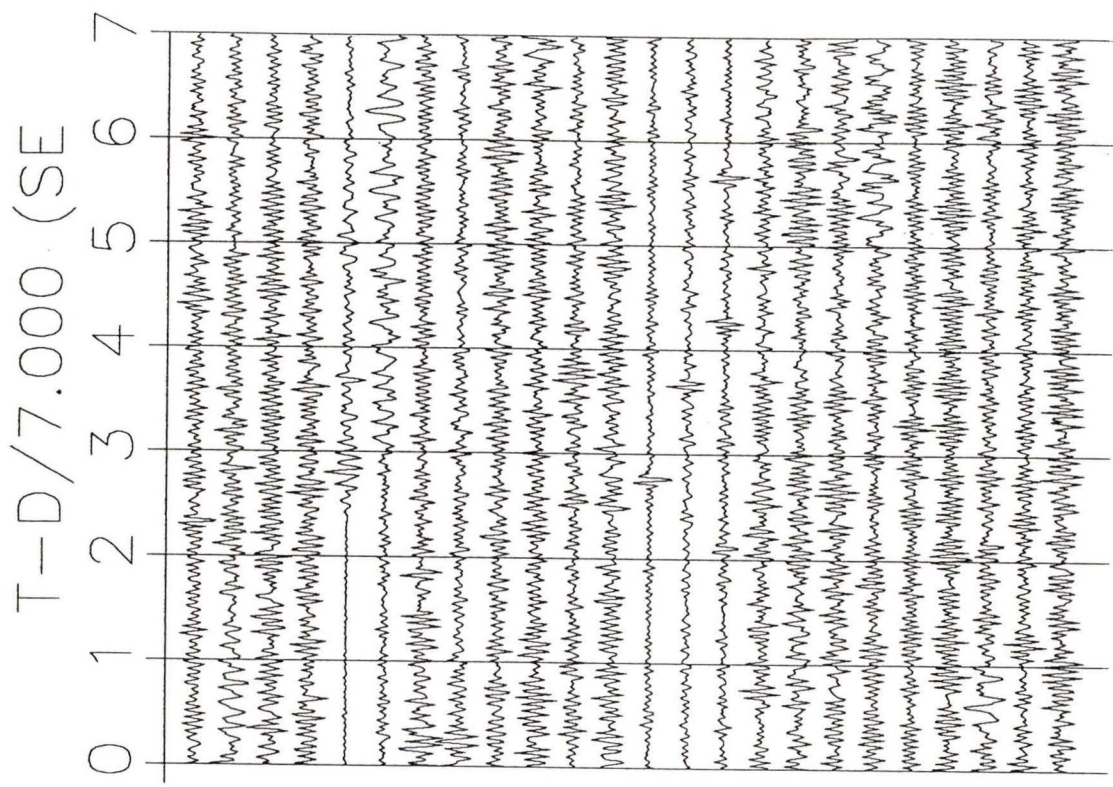
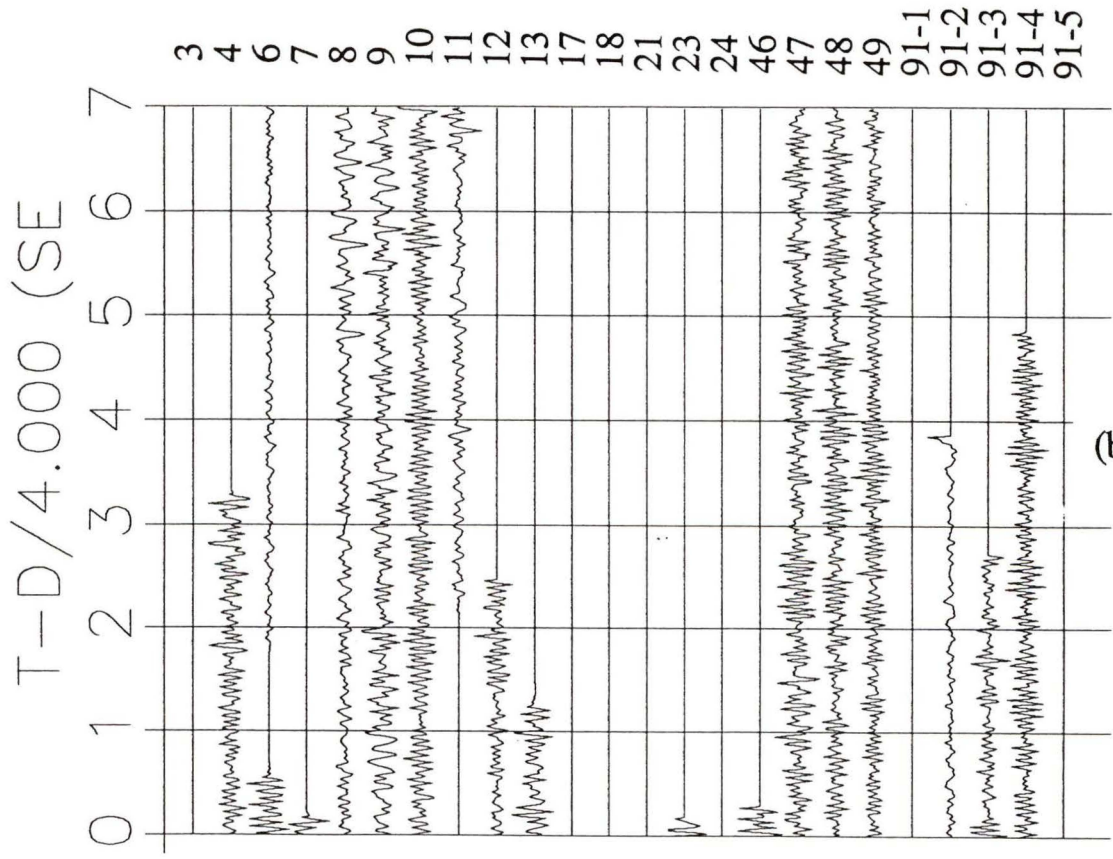


Figure 39. Seismograms at Eliza Dome Station: (a) P wave arrivals (b) S wave arrivals.



(a)



(b)

Figure 40. Seismograms at Estevan Point Station: (a) P wave arrivals (b) S wave arrivals.

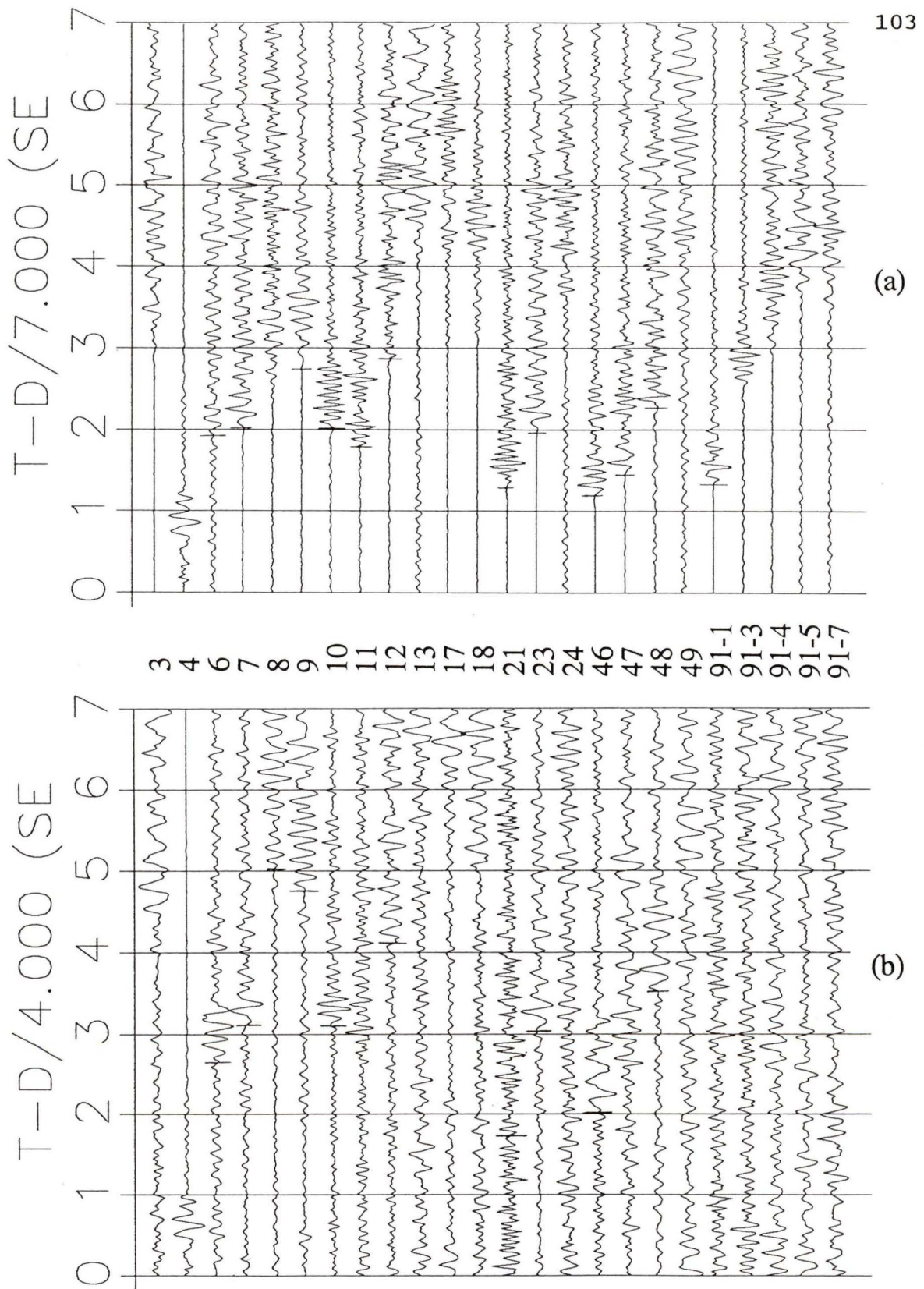


Figure 41. Seismograms at Haney Station: (a) P wave arrivals (b) S wave arrivals.

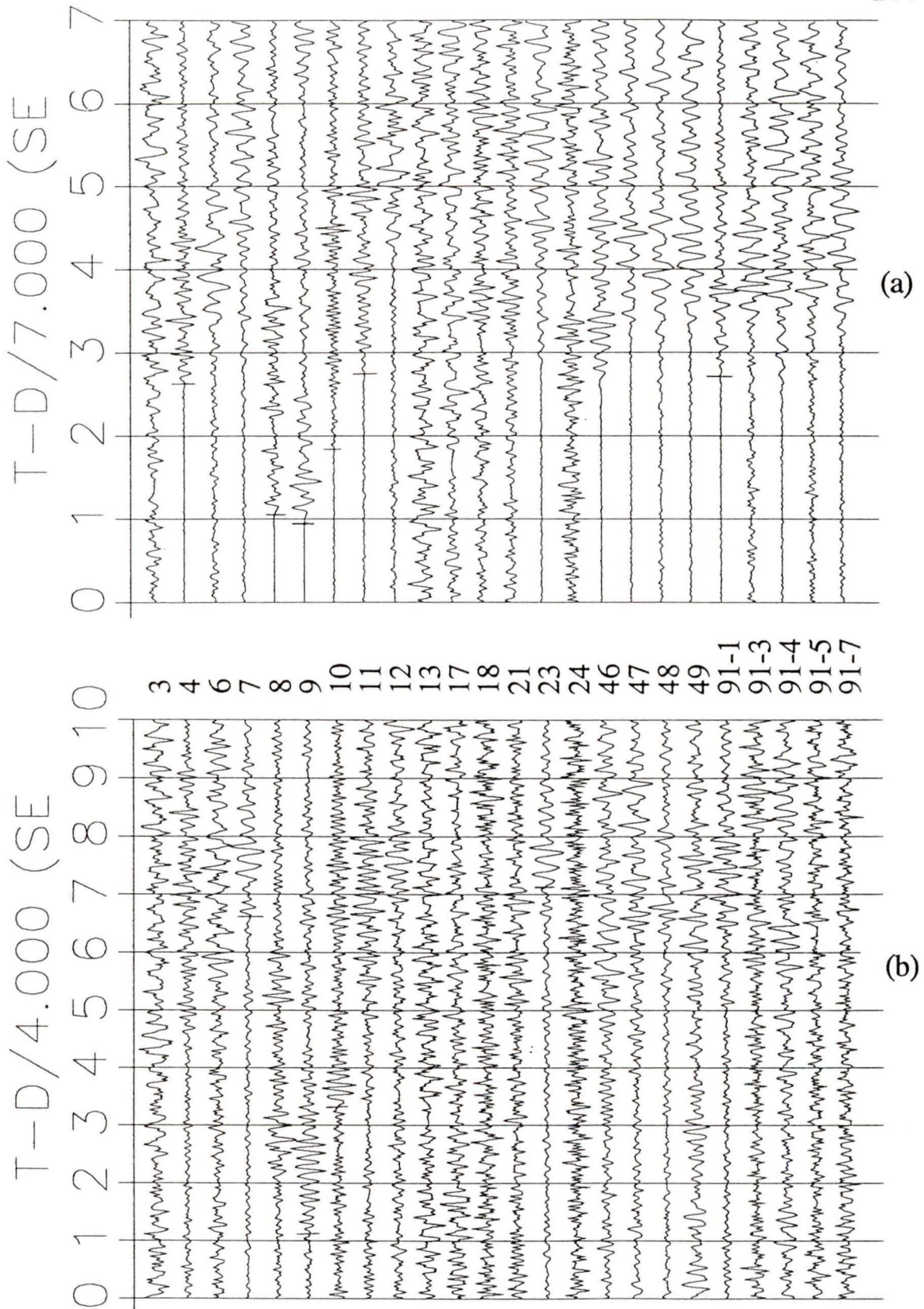
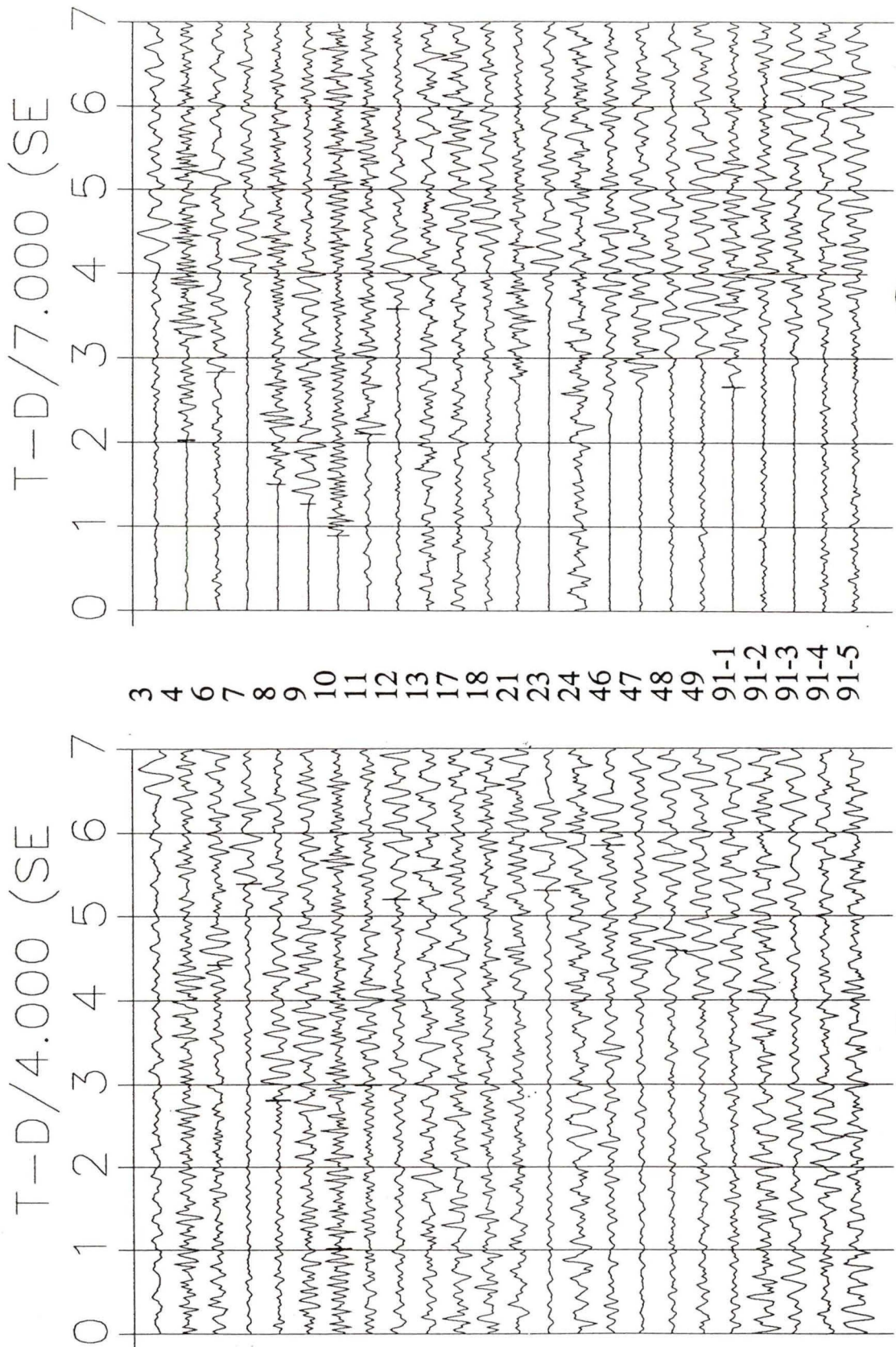


Figure 42. Seismograms at Mount Grey Station: (a) P wave arrivals (b) S wave arrivals.



(a)

(b)

Figure 43. Seismograms at Nanaimo Station: (a) P wave arrivals (b) S wave arrivals.

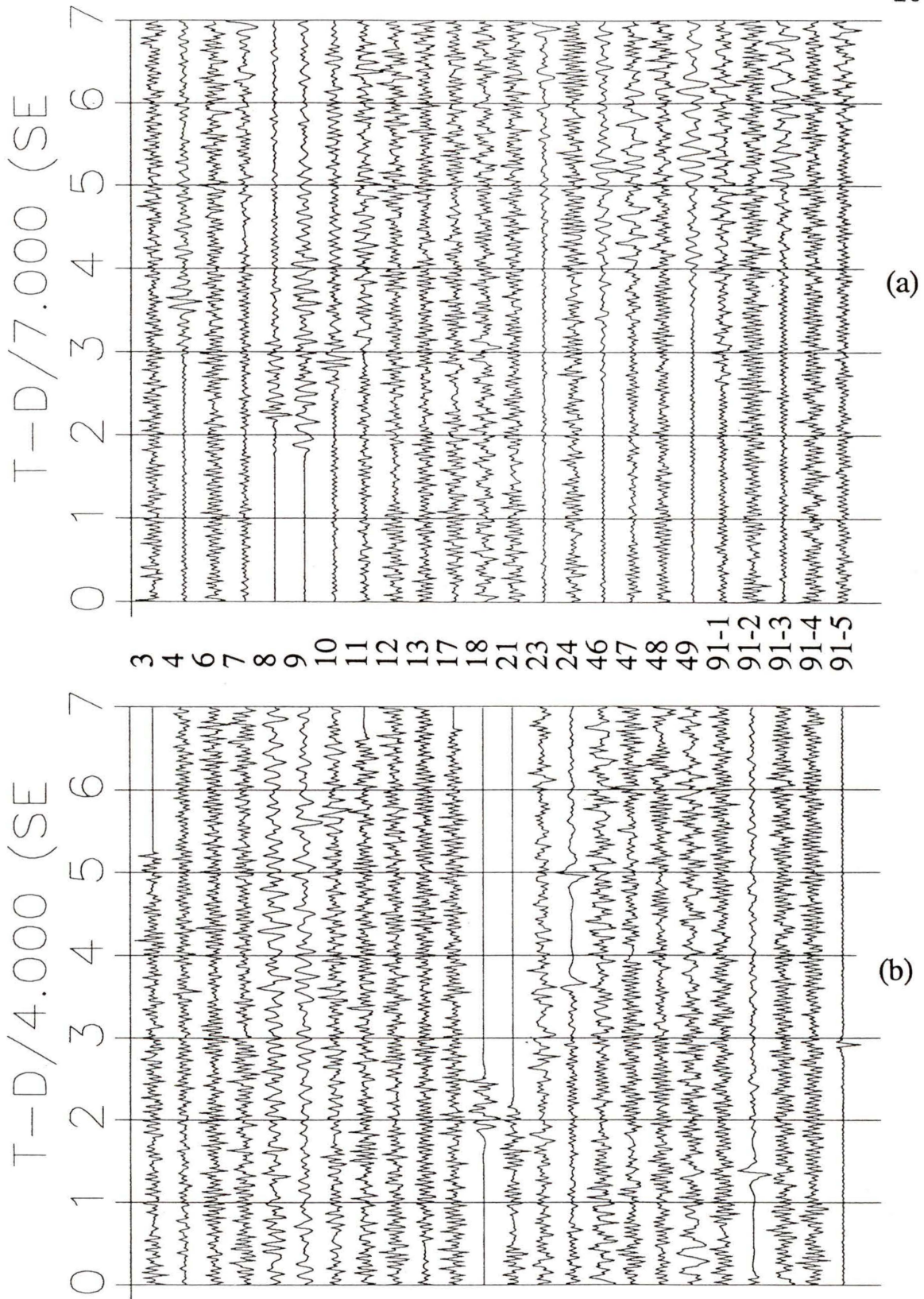


Figure 44. Seismograms at Mount Ozzard Station: (a) P wave arrivals (b) S wave arrivals.

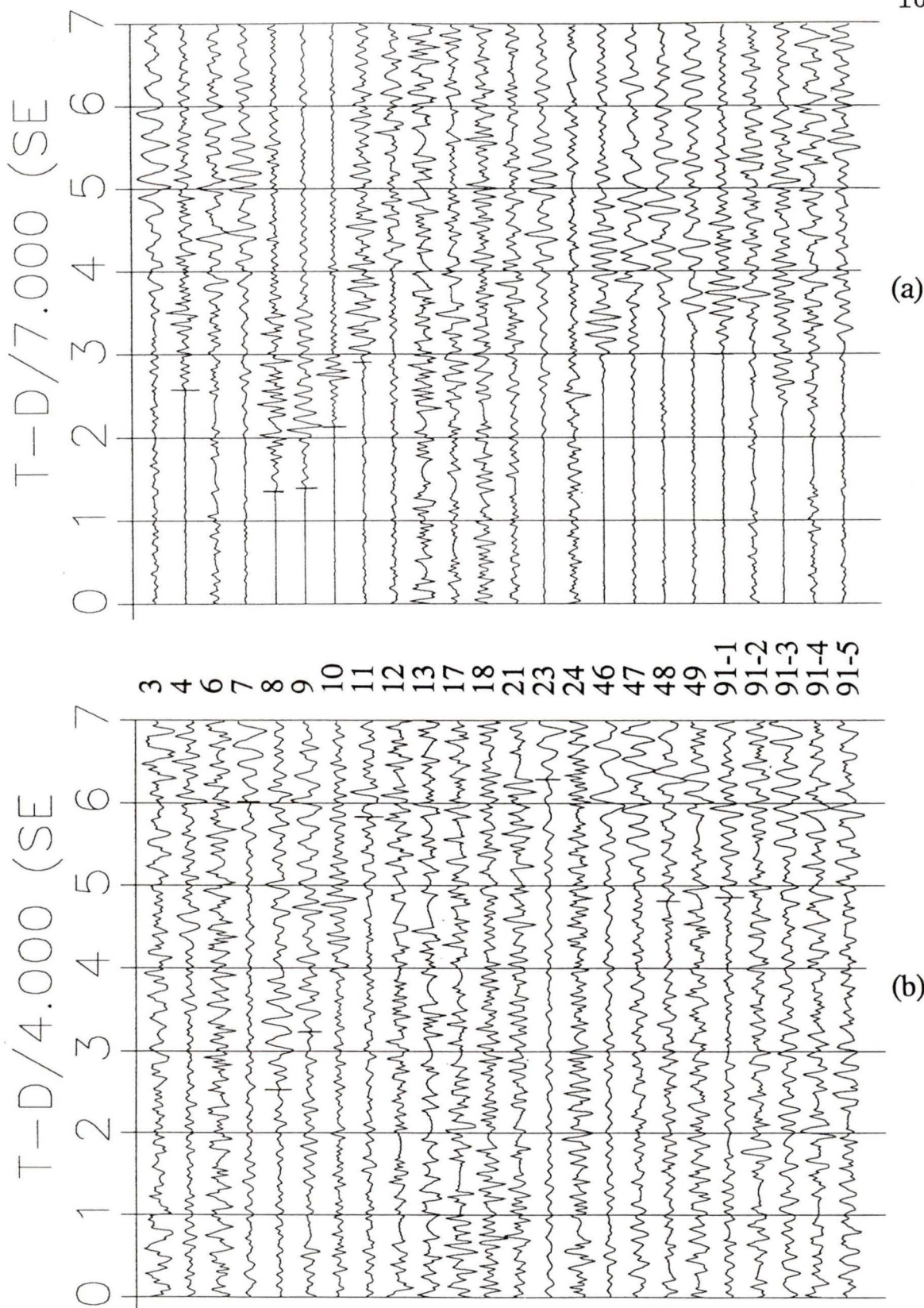


Figure 45. Seismograms at Port Renfrew Station: (a) P wave arrivals (b) S wave arrivals.

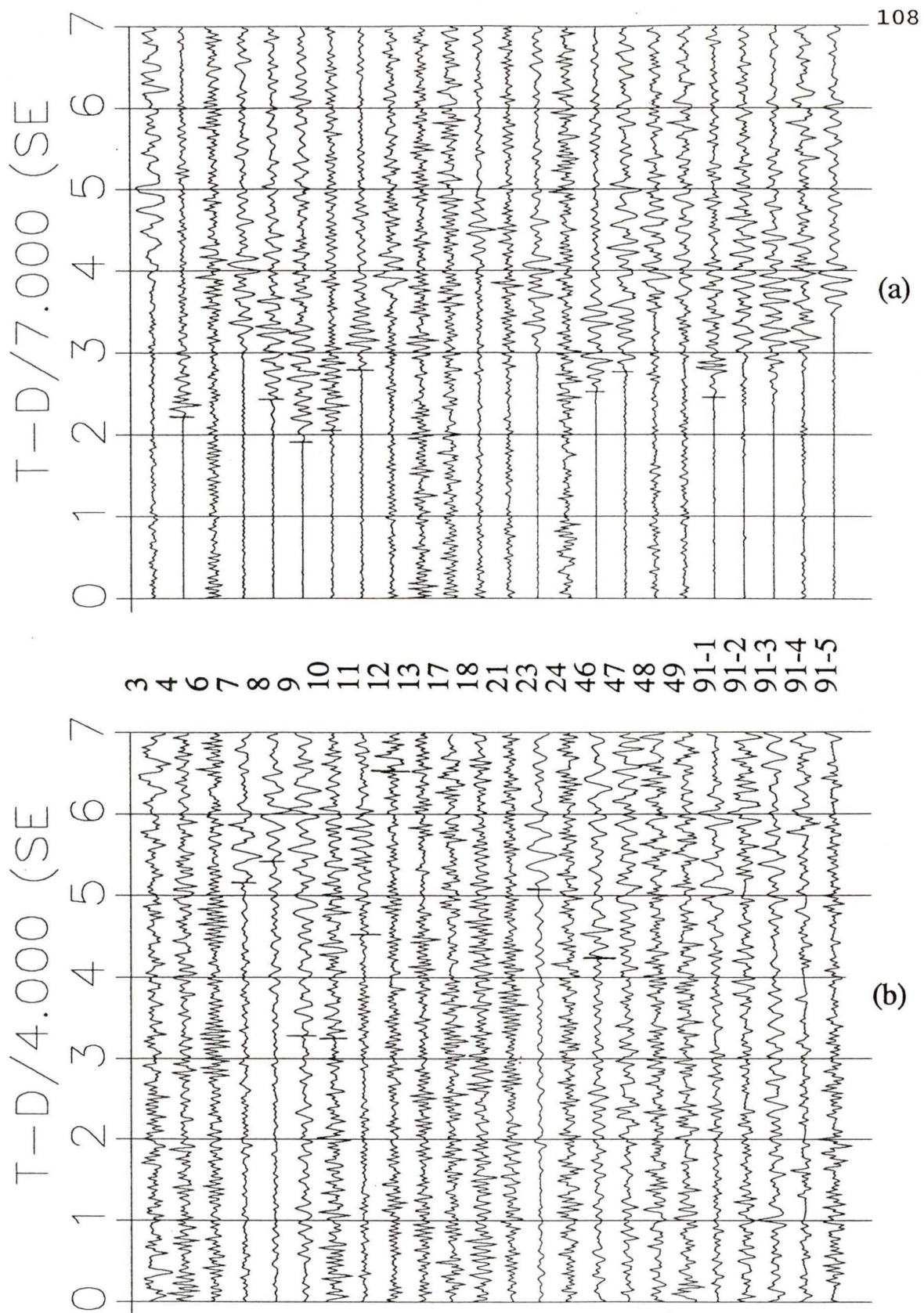


Figure 46. Seismograms at PGC Station: (a) P wave arrivals (b) S wave arrivals.

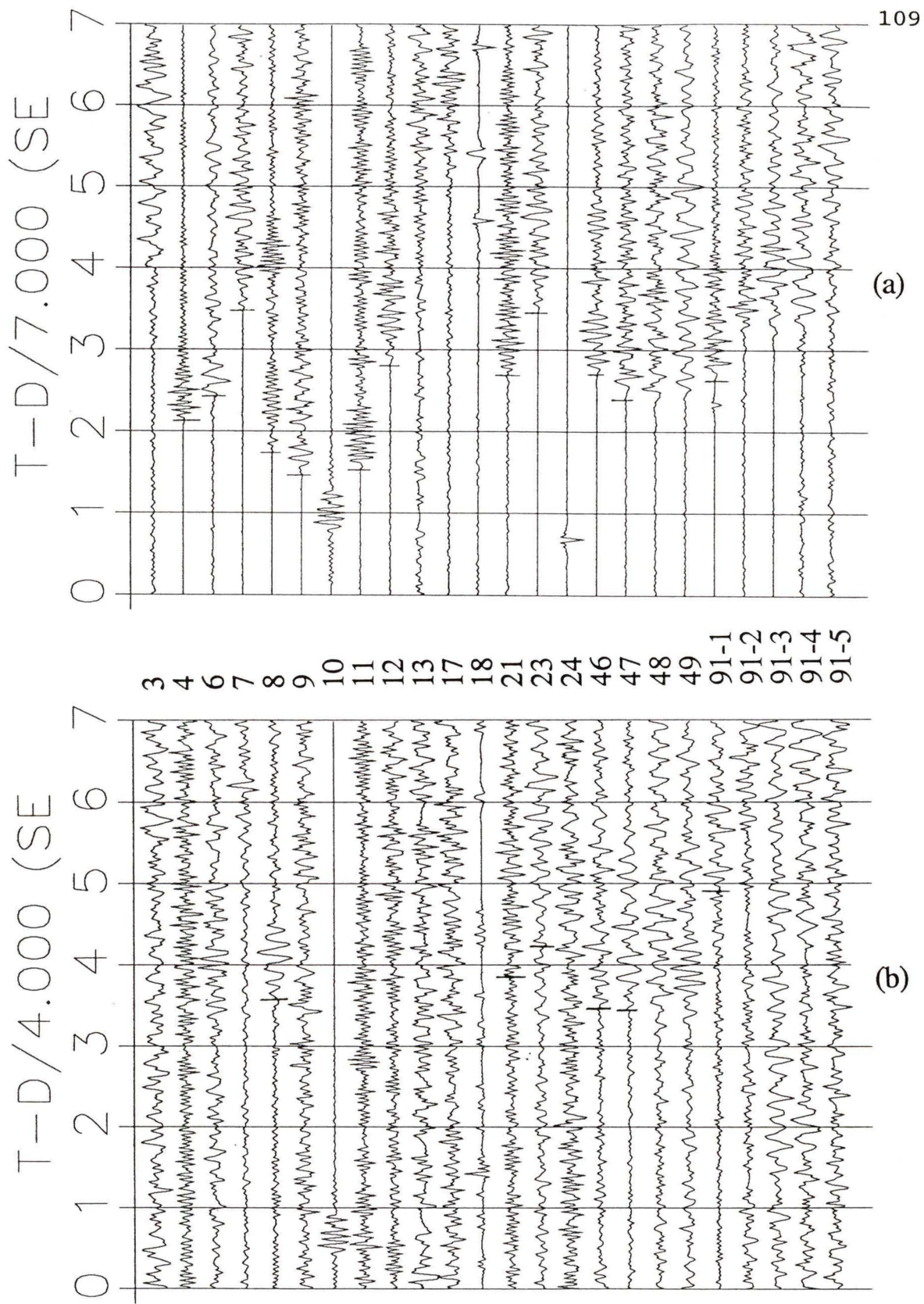


Figure 47. Seismograms at Sechelt Station: (a) P wave arrivals
(b) S wave arrivals.

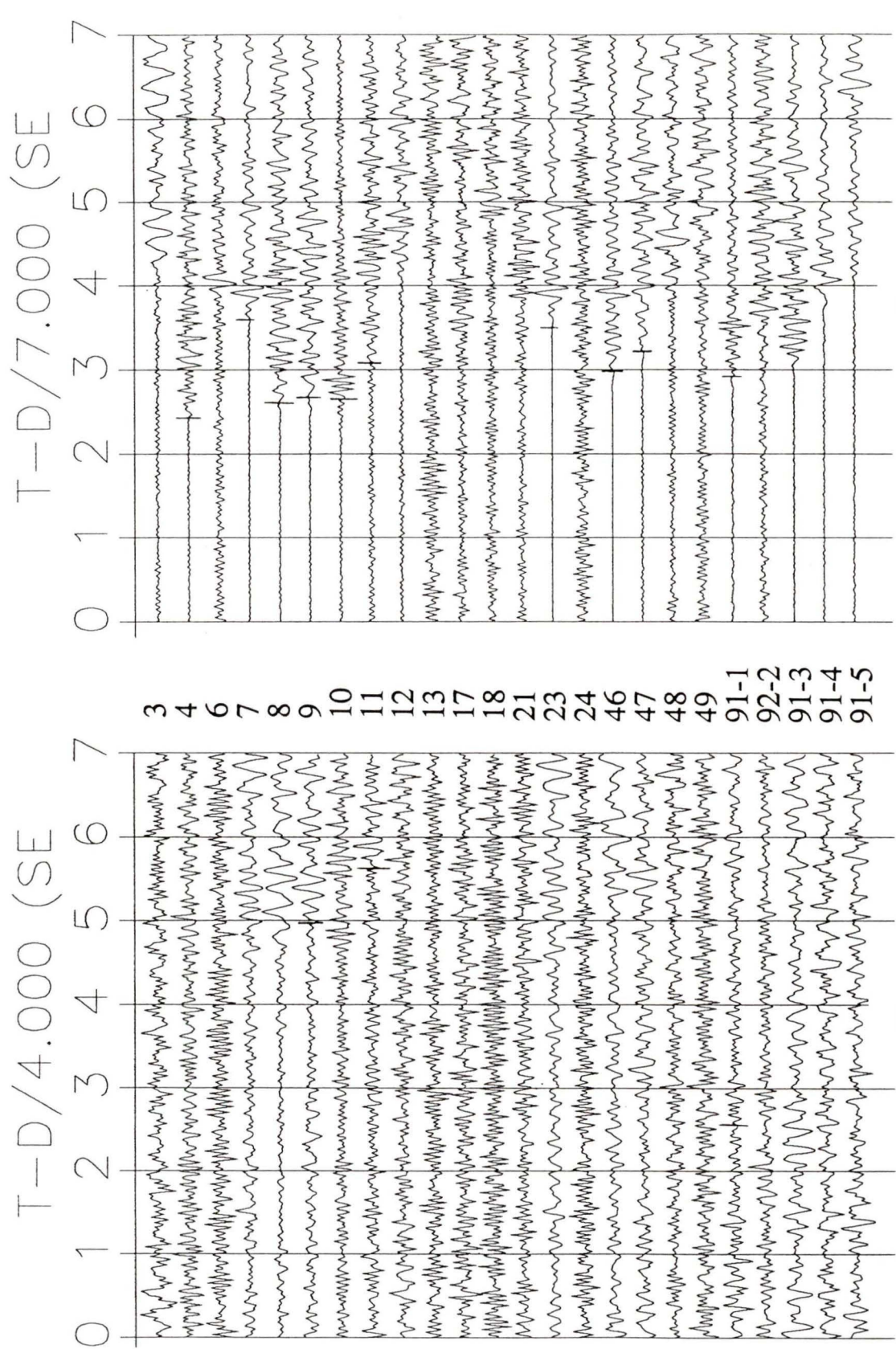


Figure 48. Seismograms at Saturna Station: (a) P wave arrivals (b) S wave arrivals.

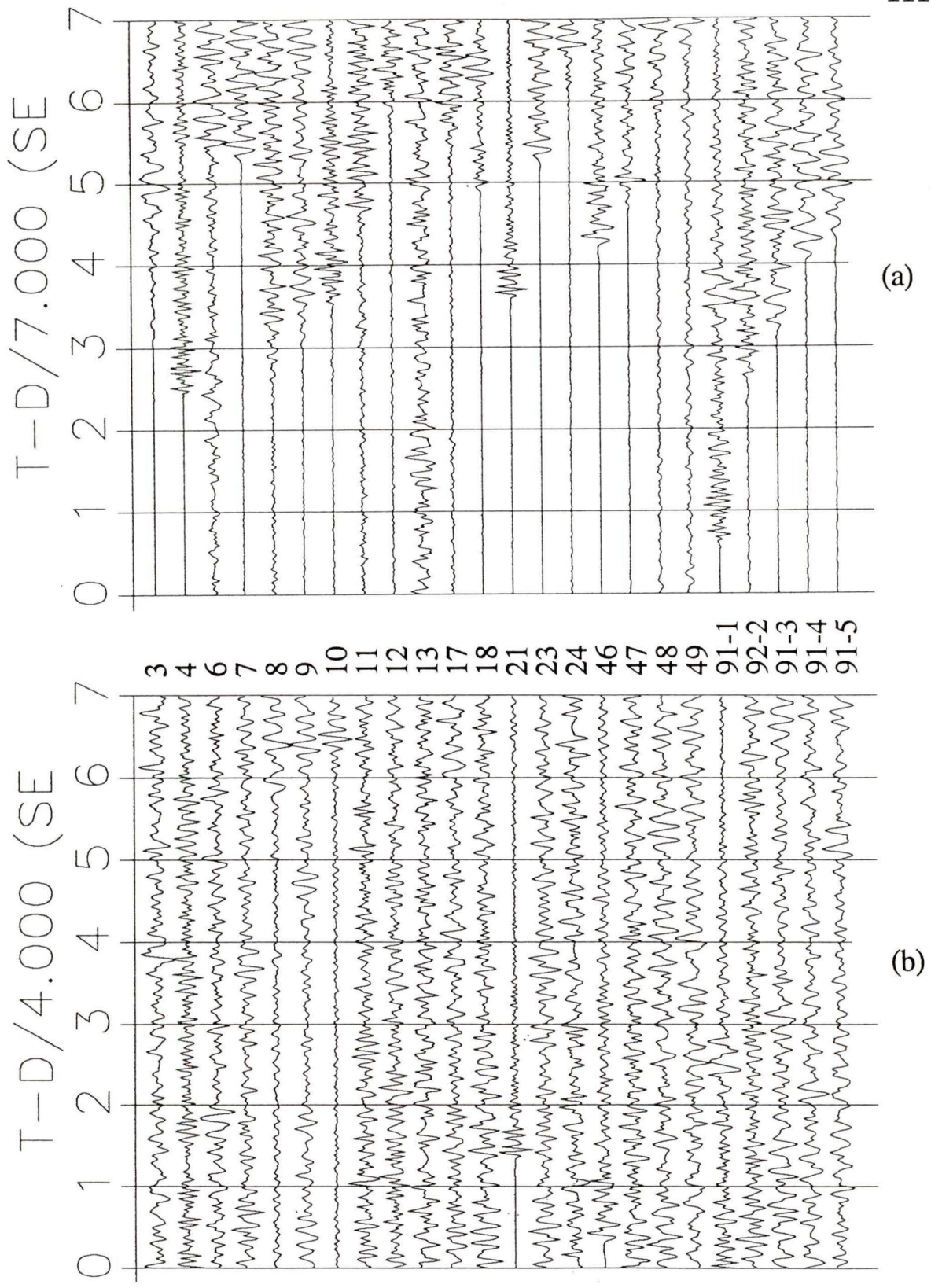
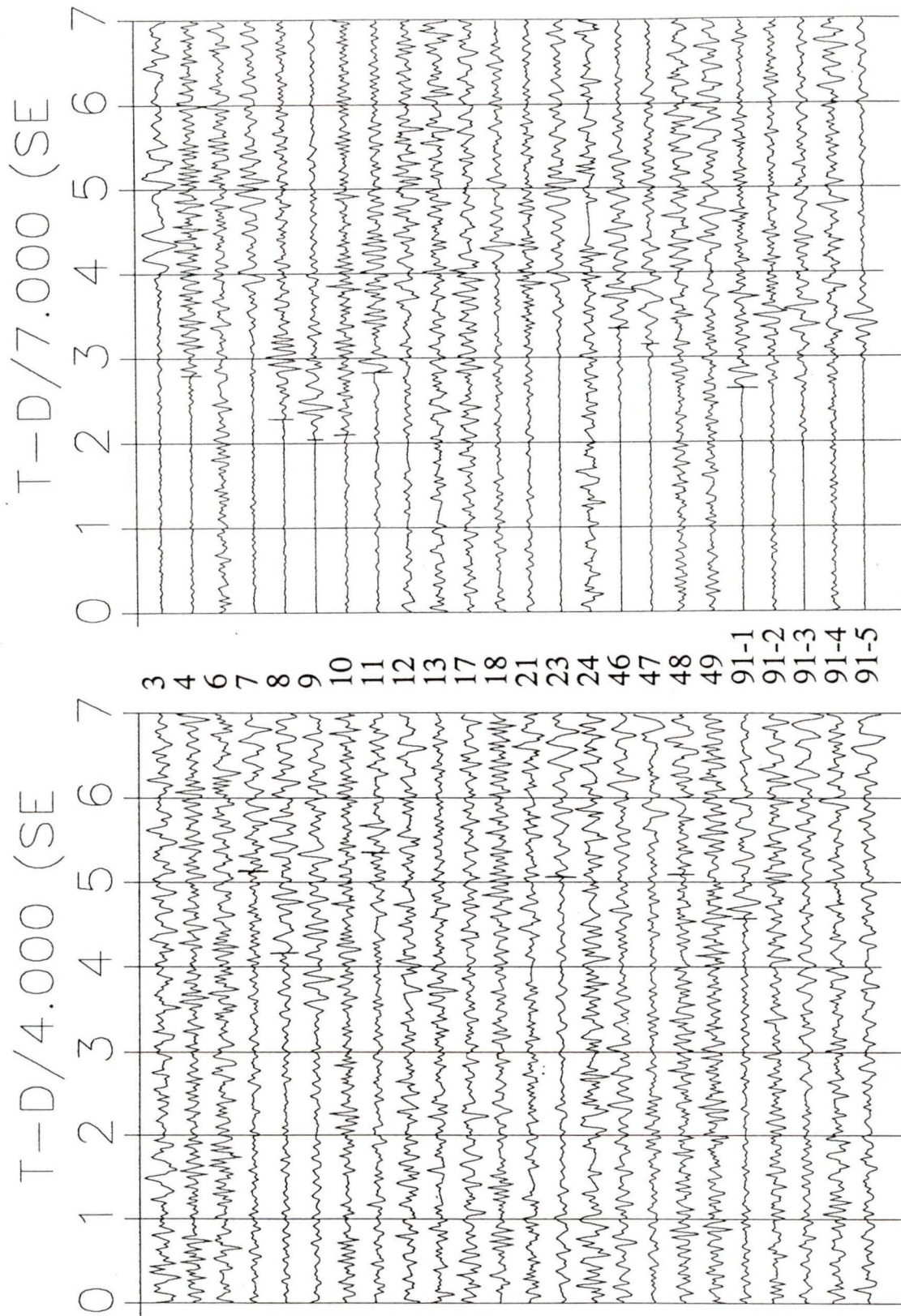


Figure 49. Seismograms at Mount Vedder Station: (a) P wave arrivals (b) S wave arrivals.



(a)

(b)

Figure 50. Seismograms at Gonzales Station: (a) P wave arrivals (b) S wave arrivals.

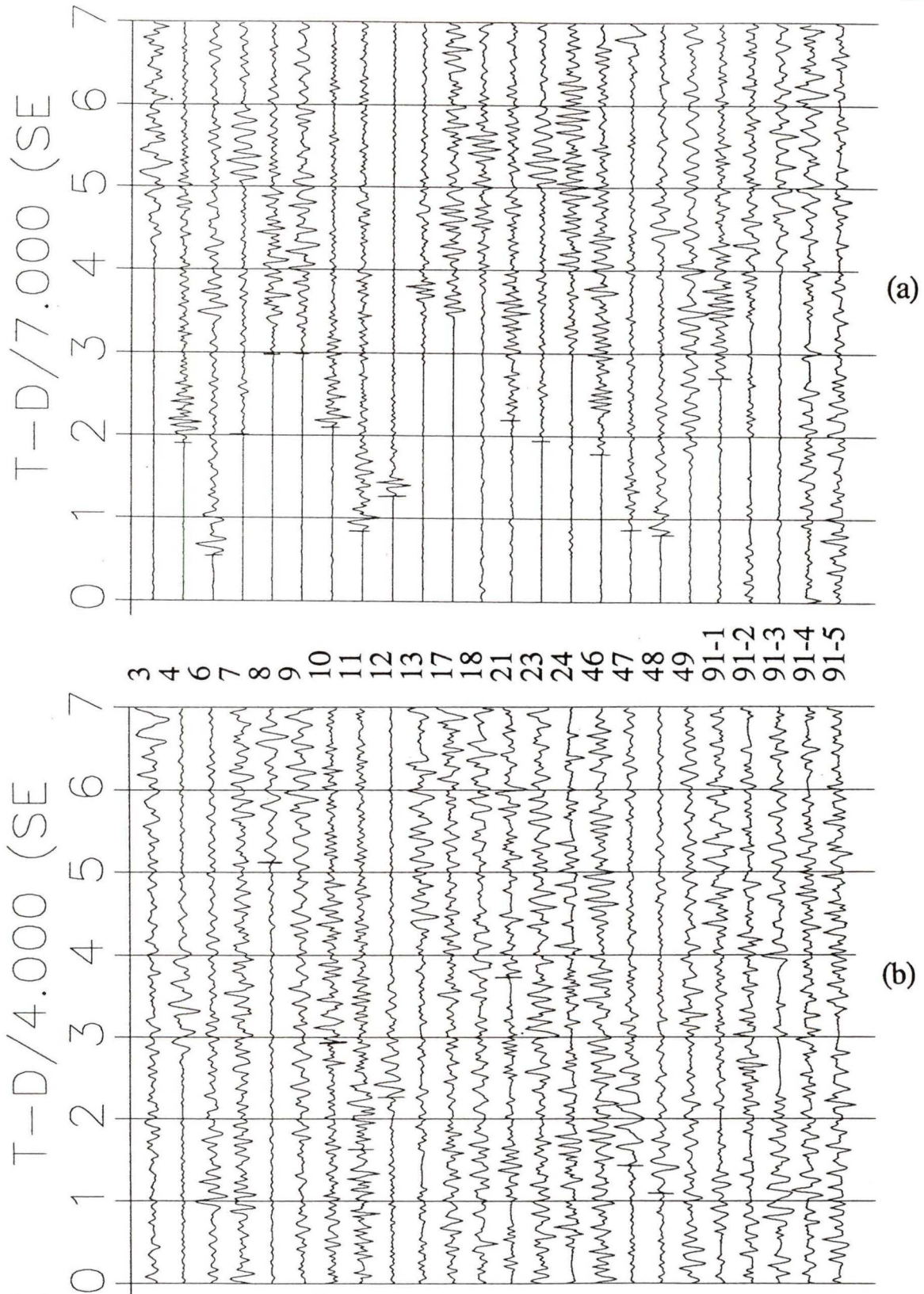


Figure 51. Seismograms at Whistler Station: (a) P wave arrivals (b) S wave arrivals.

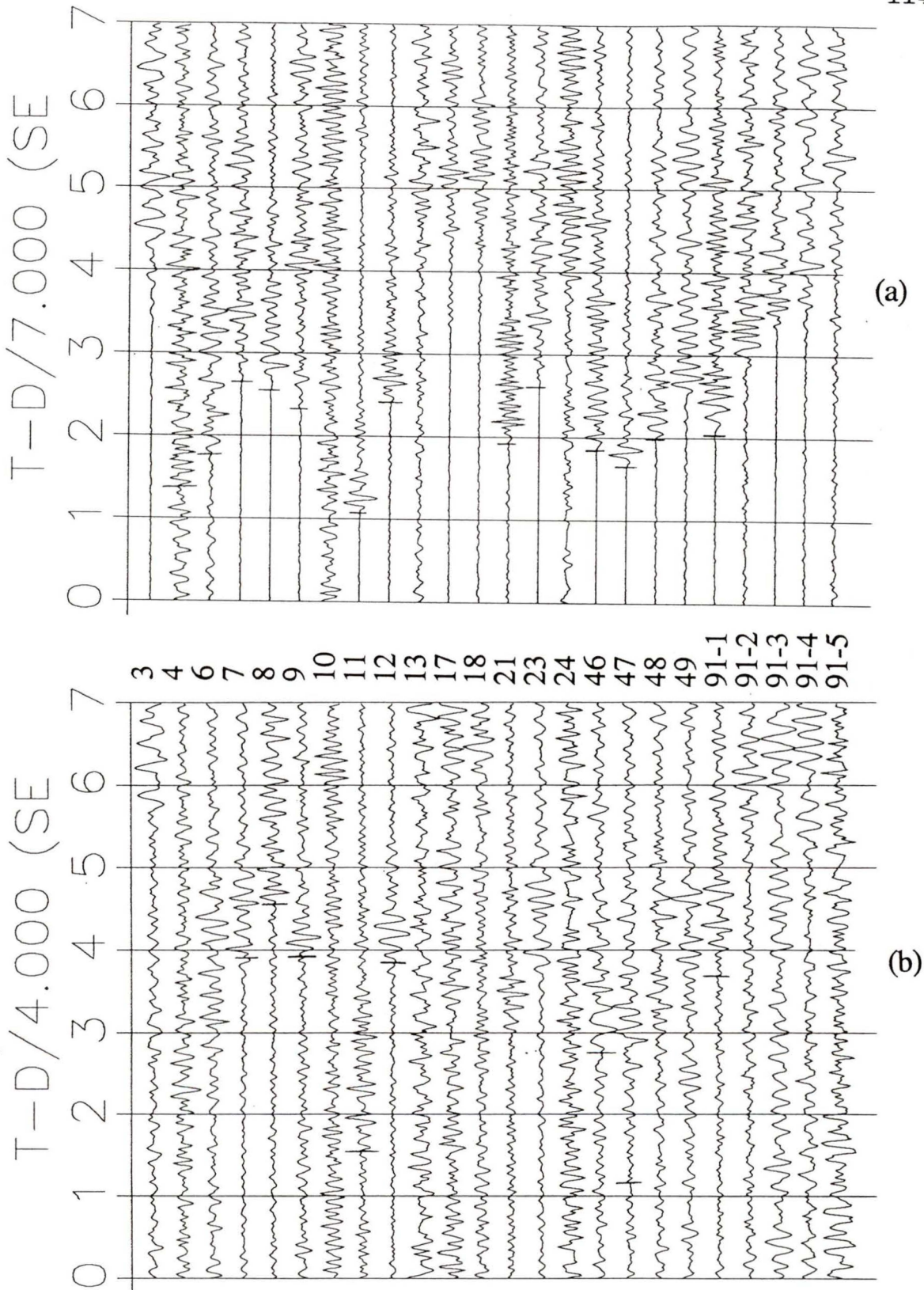


Figure 52. Seismograms at Watts Point Station: (a) P wave arrivals (b) S wave arrivals.

APPENDIX 2

SHOT	STATION	OFFSET (km)	ARRIVAL TIME (s)
4	ALB	162.487	26.155
4	BIB	52.997	8.939
4	MGB	156.703	25.024
4	NAB	102.714	16.719
4	PFB	157.137	24.667
4	PGC	95.087	15.803
4	SHB	98.615	16.226
4	SNB	71.385	12.629
4	VGZ	111.512	18.367
4	WHB	96.264	15.643
4	WPB	59.986	10.104
6	BIB	106.852	17.403
6	HNB	115.170	18.476
6	NAB	149.354	24.083
6	SHB	111.465	18.315
6	WHB	23.416	3.902
6	WPB	78.357	13.062
7	BIB	139.906	23.142
7	HNB	107.713	17.410
7	SHB	169.908	27.743
7	WHB	97.956	15.994
7	WPB	122.064	20.295
8	ALB	32.983	5.442
8	BIB	134.114	21.705
8	BTB	26.832	4.517
8	CBB	63.238	10.224
8	MGB	62.926	10.058
8	NAB	88.239	14.106
8	PFB	113.765	17.712
8	PGC	154.906	24.532
8	SHB	93.304	15.105
8	SNB	164.534	26.120
8	WPB	141.842	23.263
9	ALB	19.509	3.552
9	BIB	100.243	16.315
9	BTB	60.728	10.244
9	CBB	83.829	13.286
9	HNB	154.031	24.723
9	MGB	46.778	7.752
9	NAB	54.356	9.064
9	PFB	96.118	15.122
9	PGC	124.566	19.698
9	SHB	62.019	10.263
9	SNB	131.977	21.400
9	VGZ	150.029	23.548
9	WHB	147.491	24.093

SHOT	STATION	OFFSET (km)	ARRIVAL TIME (s)
9	WPB	110.144	18.046
10	ALB	77.473	12.993
10	BIB	44.278	7.216
10	BTB	120.541	19.565
10	CBB	119.793	19.314
10	HNB	98.780	16.122
10	MGB	87.619	14.902
10	NAB	39.804	6.594
10	PFB	118.586	19.102
10	PGC	106.512	17.262
10	SNB	101.698	17.155
10	VGZ	134.340	21.318
10	WHB	90.231	14.994
11	ALB	141.746	23.623
11	BIB	63.405	10.472
11	HNB	89.161	14.524
11	MGB	153.618	24.698
11	NAB	101.951	16.646
11	SHB	64.534	10.748
11	SNB	133.029	22.096
11	VGZ	173.454	27.607
11	WHB	24.221	4.328
11	WPB	34.960	6.097
12	BIB	138.139	22.395
12	HNB	132.415	21.795
12	SHB	149.647	24.102
12	WHB	61.184	10.006
12	WPB	111.263	18.315
21	BIB	104.709	17.033
21	HNB	51.748	8.726
21	PGC	137.436	22.421
21	SHB	148.581	23.950
21	WHB	119.305	19.251
21	WPB	104.068	16.792
23	BIB	140.006	23.145
23	HNB	107.786	17.427
23	SHB	170.016	27.788
23	WHB	98.068	15.981
23	WPB	122.170	20.126
46	BIB	100.668	16.146
46	HNB	54.328	8.945
46	NAB	154.257	24.279
46	PGC	147.056	23.577
46	SHB	141.217	22.881
46	SNB	122.441	20.452
46	VGZ	159.505	25.136
46	WHB	100.641	16.245
46	WPB	94.055	15.321
47	BIB	88.994	14.500

SHOT	STATION	OFFSET (km)	ARRIVAL TIME(s)
47	HNB	73.765	11.987
47	NAB	141.829	22.818
47	PGC	162.106	25.991
47	SHB	114.672	18.796
47	SNB	140.445	23.408
47	WHB	48.065	7.792
47	WPB	67.621	11.413
48	HNB	124.058	19.999
48	NAB	152.927	24.726
48	WHB	28.643	4.903
48	WPB	84.081	14.023
91-1	BIB	96.725	16.255
91-1	HNB	46.702	8.017
91-1	NAB	136.727	22.181
91-1	PFB	171.323	27.475
91-1	PGC	99.026	16.607
91-1	SHB	143.029	23.094
91-1	SNB	75.175	13.630
91-1	VGZ	103.011	17.348
91-1	WHB	142.903	23.145
91-1	WPB	108.877	17.657

APPENDIX 3

SHOT	STATION	OFFSET (km)	ARRIVAL TIME (s)
6	HNB	115.170	31.473
6	NAB	149.354	41.743
7	ALB	247.093	68.520
7	BIB	139.906	38.837
7	BTB	288.851	79.826
7	CBB	269.809	73.497
7	HNB	107.713	29.973
7	MGB	250.612	69.822
7	NAB	194.257	53.879
7	PFB	260.903	71.237
7	PGC	201.988	55.666
7	VGZ	217.001	59.385
7	WPB	122.064	34.353
8	ALB	32.983	9.836
8	BIB	134.114	37.664
8	BTB	26.832	8.001
8	HNB	188.217	51.959
8	NAB	88.239	24.841
8	PFB	113.765	31.211
8	PGC	154.907	43.851
8	SHB	93.303	26.765
8	VGZ	178.899	48.838
8	WHB	173.698	48.492
8	WPB	141.842	39.899
9	ALB	19.509	6.192
9	BIB	100.242	28.230
9	CBB	83.830	23.727
9	HNB	154.032	43.188
9	MGB	46.778	12.840
9	PFB	96.119	27.300
9	PGC	124.566	35.732
9	SNB	131.976	38.084
9	WPB	110.143	31.373
10	BIB	44.278	12.452
10	HNB	98.780	27.695
10	MGB	87.619	25.130
10	NAB	39.804	10.974
10	PGC	106.512	29.965
10	WHB	90.231	25.531
11	BIB	63.405	17.711
11	BTB	177.192	49.978
11	NAB	101.952	28.499
11	PFB	180.270	50.905
11	PGC	148.144	41.817
11	SNB	133.029	38.802
11	VGZ	173.455	48.679
11	WHB	24.221	7.915

SHOT	STATION	OFFSET (km)	ARRIVAL TIME (s)
11	WPB	34.960	10.111
12	HNB	132.415	37.171
12	NAB	185.336	51.559
12	PGC	217.712	60.732
12	WHB	61.184	17.555
12	WPB	111.263	31.496
21	HNB	51.748	14.651
21	NAB	155.577	42.777
21	SHB	148.581	40.971
21	WHB	119.306	33.371
23	ALB	247.199	68.424
23	BIB	140.005	38.816
23	BTB	288.962	79.600
23	HNB	107.786	29.970
23	MGB	250.713	69.768
23	NAB	194.358	53.904
23	PFB	260.992	71.518
23	PGC	202.063	55.629
23	SHB	170.016	46.819
23	VGZ	217.066	59.290
46	HNB	54.327	15.386
46	PGC	147.056	41.000
46	SHB	141.217	39.349
46	WPB	94.056	26.239
47	BTB	233.260	64.349
47	SHB	114.672	32.005
47	WHB	48.066	13.376
47	WPB	67.621	18.495
48	BTB	216.907	59.677
48	CBB	183.726	51.555
48	HNB	124.057	34.514
48	NAB	152.927	42.754
48	PFB	231.481	62.685
48	VGZ	220.957	60.262
48	WHB	28.643	8.228
91-1	PGC	99.026	29.094
91-1	SNB	75.175	21.474
91-1	VGZ	103.011	29.888
91-1	WPB	108.877	31.079

APPENDIX 4

For a two layer model the theoretical travel time t_{ij} of a wave propagating as a head wave along the velocity boundary between sites i and j on the surface of the model is given by (Berry and West, 1966)

$$t_{ij} = \frac{dis_{ij}}{v_2} + a_i + a_j \quad \text{Eq.A1}$$

in which

$$a_i = \frac{Z \left(1 - \frac{v_1^2}{v_2^2} \right)^{\frac{1}{2}}}{v_2} \quad \text{Eq.A2}$$

where

dis_{ij} is the offset distance between the sites i and j
 a_i and a_j are the time terms for the sites i and j , respectively, v_1 is the upper layer velocity, and v_2 the refracting layer velocity, Z is the depth of the refracting layer.

In using equations A1 and A2 the following assumptions about the real earth are made: (i) velocity varies only with depth beneath shot and station sites and not laterally, (ii) the velocity v_2 is constant, and (iii) the slope of the refracting surface is small (Berry and West 1966).

If the observed travel time is T_{ij} , then R_{ij} expresses the residual of that particular observation

$$T_{ij} - t_{ij} = R_{ij} \quad \text{Eq.A3}$$

and therefore

$$R_{ij} = X_{ij} - a_i - a_j \quad \text{Eq.A4}$$

where the observed quantities have been combined in X_{ij}

$$X_{ij} = T_{ij} - \frac{dis^{ij}}{v_2} \quad \text{Eq.A5}$$

For a data set in which there are N sites, it is likely that there will be more observational travel times than the N unknown site time terms. The over determined problem can be solved by stipulating that the time terms minimize the sum of the squares of the Residuals R_{ij} . For future reference a quantity γ_{ij} will be defined as follows

$$\gamma_{ij} = 1 \text{ when } T_{ij} \text{ exists in the data set}$$

$$\gamma_{ij} = 0 \text{ when } T_{ij} \text{ is not present}$$

Taking the sum of the squares of the residuals and then minimizing with respect to each time term

$$\sum_{j=1}^{i-1} a_j \gamma_{ij} + a_i \sum_{j=1}^N \gamma_{ij} + \sum_{j=i+1}^N a_j \gamma_{ij} = \sum_{j=1}^N X_{ij} \gamma_{ij} \quad \text{Eq.A6}$$

For the complete set of N simultaneous equations the matrix form is

$$C \times A = \bar{X}$$

Eq. A7

where

$$C_{ij} = \gamma_{ij}, \quad i \neq j$$

$$C_{ii} = \sum_{j=1}^N \gamma_{ij}$$

Eq. A8

$$\bar{X}_i = \sum_{j=1}^N X_{ij} \gamma_{ij}$$

The matrix shown in equation A7 has no unique solution. However, it can be made non-singular by arbitrarily assigning a value to one of the time terms. The results shown in Table 11 were obtained by the addition of a time term to site 91-3 which resulted in the same value at the shotpoint 10 and Sechelt station sites.

VITA

Surname: Fallows
Given Names: Stephen John
Place of Birth: Bletchley, England
Date of Birth: 26 December 1969

Educational Institutions Attended:

University of Victoria	1991 to 1994
University of York	1988 to 1991

Degrees Awarded:

B.Sc. University of York	1991
--------------------------	------


Honours and Awards:

University of Victoria Graduate Teaching Award	1991 to 1994
---	--------------

PARTIAL COPYRIGHT LICENSE

I hereby grant the right to lend my thesis to users of the University of Victoria Library, and to make single copies only for such users or in response to a request from the Library of any other university, or similar institution, on its behalf or for one of its users. I further agree that permission for extensive copying of this thesis for scholarly purposes may be granted by me or by a member of the University designated by me. It is understood that copying or publication of this dissertation for financial gain shall not be allowed without my written permission.

Title of Thesis: Upper Crustal Velocity Structure of the Southwestern Canadian Cordillera from Explosion Recordings on the WCTN Earthquake Seismic Net.

Author —  —

Stephen John Fallows

12 August 1994